On the Planar Flow Development and Structural Loading of Cylinders with Circular Fins in Cross-Flow

by

Jeffrey Ernest John McClure

A thesis
presented to the University of Waterloo
in fulfillment of the
thesis requirement for the degree of
Master of Applied Science
in
Mechanical Engineering

Waterloo, Ontario, Canada, 2015

I hereby declare that I am the sole author of this thesis. This is a true copy of the thesis, including any required final revisions, as accepted by my examiners.

I understand that my thesis may be made electronically available to the public.

Abstract

Finned cylinders are commonly encountered in the design of heat exchangers. Critical to the design and performance of a heat exchanger are the mean and fluctuating loading on the tubes, as they relate to pressure losses across the model and may lead to structural vibrations. The loading characteristics are related to the vortex shedding phenomena in the wakes of finned tubes, which motivates the need to understand their relationship in detail. The flow development and structural loading characteristics of cylinders with equispaced circular fins were studied experimentally in the University of Waterloo water flume facility. Finned cylinders of diameter ratio $D_f/D = 2.0$, fin thickness ratio $t/D = 0.028$ and range of fin pitch ratios $0.083 \leq c/D \leq 1.0$ were investigated using Particle Image Velocimetry (PIV), Laser Doppler Velocimetry (LDV), and force balance measurements. The Reynolds number ranged from $Re_{D_eff} = 1020 - 2040$ based on the effective diameter of the models, corresponding to the shear layer transition turbulent shedding regime. For $c/D \geq 1.0$, the vortex development resembles that of a uniform base cylinder, besides a region of affected flow near each fin. Further reduction of c/D results in similar scales of vortex formation, but with increased unsteady flapping of the separated shear layers. Following that, for $c/D \leq 0.083$, boundary layer coalescence between the fins leads to the flow redirection and separation at the fin diameter. The generation of lateral vorticity between the fins leads to the progressive weakening of the spanwise shear layers with decreasing c/D. However, the bleeding of low-energy fluid into the near wake from the viscous regions between the fins has a stabilizing effect on the mixing of vorticity during vortex formation, thereby augmenting the structure of turbulence in the wake and inducing stronger wake vortex shedding. Linear increases in the mean drag with increasing fin density are attributed to the independent viscous shear contributions introduced by each finned surface, and the fall off of the linear trend with high fin density is due to the loss of this independence with lateral boundary layer coalescence. The RMS of the fluctuating lift is shown to increase initially for decreasing $c/D \rightarrow 0.33$, as the wake vortices increase in strength and flow unsteadiness increases near the cylinder surface. However, the fluctuating lift is severely diminished for low $c/D = 0.083$, with vortex formation displaced much further downstream, despite exhibiting stronger wake vortices. The vortex shedding frequency is shown to decrease with decreasing c/D. A modification of the definition of the Strouhal number based on the cylinders effective diameter is proposed which incorporates Reynolds numbers effects associated with the differences in the added flow blockage created by the boundary layers developing on the fin surfaces. This definition is found to universally collapse the shedding frequency data in the study and literature onto a constant $St_{Deff*} \approx 0.2$ with little scatter.

Acknowledgments

I would like to thank my advisor, Dr. Serhiy Yarusevych, for constantly being involved and committed to producing quality work in collaboration with his students and whose knowledge and work ethic I hope have osmosed to me somewhat during our time working together. I would also like to thank Dr. Chris Morton for his mentorship during my studies and my fellow graduate students, Andrew Lambert, Sahil Mahey, Eugene Zivkov, John Kurelek, Ajith Airody, and JiaCheung Hu for the good times and tight knit working environment. In addition, I extend my thanks to my advisory committee members, Dr. Sean Peterson and Dr. Steven Waslander, for their fruitful comments and suggestions towards refining the document.

Finally, I would like to thank Natural Sciences and Engineering Research Council and the University of Waterloo for the financial support of my research.

Dedication

I would like to dedicate this thesis to my mother, Angie. Without her lifelong example of strength and dedication, this thesis would surely be half as long.

Table of Contents

List of Figures

List of Tables

Nomenclature

a_i	i^{th} POD temporal mode coefficient
c	Fin pitch
C_{bp}	Base pressure coefficient
C_D	Mean drag coefficient
$C_{D,p}$	Mean pressure drag coefficient
$C_{D,v}$	Mean viscous drag coefficient
$C_{L'}$	Sectional lift RMS coefficient
$C_{L',T}$	Total lift RMS coefficient
C_{ps}	Pressure coefficient at separation point
C_{pf}	Frontal pressure coefficient
D	Base cylinder diameter
D_b	Support cylinder diameter
D_{eff}	Finned cylinder effective diameter
D_{eff*}	Modified finned cylinder effective diameter
D_f	Fin diameter
D_H	Projected height of the cluster
D_o	Shell diameter of porous media
E_{uu}	Fluctuation energy
f	Frequency
f_{acq}	Acquisition/sampling frequency
f_c	Filter cut-off frequency
f_{flow}	Characteristic frequency in the flow
f_S	Vortex shedding frequency
$f_{S,\theta}$	Vortex shedding frequency with oblique angle correction
f_ρ	Fin Density
GF	Gauge factor
K	Vorticity advection of the wake vortices
K_M	Magnification factor

K_s	Vorticity production in a cylinder shear layer
L	Length of cylinder
L_f	Vortex formation length
L_w	Wake width
N	Quantity
M	Cell size
p	Pressure
p_b	Base pressure
p_o	Free-stream pressure
Re_D	Reynolds number based on diameter D
$R_{LL}(s)$	Zero-time-delay correlation coefficient between sectional lift forces
$R_{pp}(s)$	Zero-time-delay correlation coefficient between point pressure measurements
$R_{uu}(s)$	Zero-time-delay correlation coefficient between streamwise velocity measurements
SG	Specific gravity
S_l	Longitudinal spacing between two cylinders
St_D	Strouhal number based on diameter D
S_t	Transverse spacing between two cylinders
T	Fin thickness
T^*	Modified fin thickness
t	Time
Δt	Time step
U_o	Free-stream velocity
U_s	Edge velocity at separation point
u	Streamwise velocity component
u'	RMS of the streamwise velocity component
$\overline{u'^2}$	Variance of the streamwise velocity component
$\overline{u'v'}$	Covariance of the streamwise and transverse velocity component
v	Transverse velocity component
u_{slip}	Slip velocity
$\overline{v'^2}$	Variance of the transverse velocity component
w	Spanwise velocity component
WS	Interrogation window size
δx	Average particle displacement
x	Streamwise distance from the origin
X_{bl}	Length of overlap between camera images
X_{fov}	Camera field of view
y	Transverse distance from the origin

$y_{0.95umax}$	Transverse position of the edge of the shear layer
β	Porosity
δ	Boundary layer thickness
δ_{sl}	Shear layer thickness
δ^*	Boundary layer displacement thickness
Γ	Circulation
ϵ	Measurement error
λ	Light wavelength
λ_x	Characteristic spatial wavelength of the flow
Λ	One-sided spanwise correlation length
ρ	Density
μ	Dynamic viscosity
$\tau_{\overline{u'v'}}$	Reynolds stress
τ_v	Viscous stress
ϕ_i	i^{th} POD spatial mode
Ψ	Suction/blowing coefficient
ω_z	Spanwise vorticity component
$\omega_{z,max}(x)$	Shear layer trajectory
Ω	Dimensionless proportionality constant

Chapter 1

Introduction

Cylindrical bluff-bodies are ubiquitous in engineering designs such as civil structures, bridge lines, heat exchangers, offshore risers, pipelines and antennae (e.g., [1–6]). Due to the geometric simplicity of the circular cylinder, it is perhaps counter-intuitive that the characteristics of the fluid flow surrounding it would initiate such a considerable research effort over the past centuries. However, due to the inherent complexity and intractability of the governing fluid physics, developing insightful models of the flow and related dynamics has proven a formidable task [4].

Asymptotic solutions are known for creeping flow ($Re_D << 1$) and analytical solutions are known for inviscid flow ($Re_D \to \infty$) of uniform cross-flow over a uniform cylinder. However, the bulk of practical interest lies within the domain of intermediate Reynolds numbers, where the phenomenon of vortex shedding dominates the cylinder wake development [7,8]. Vortex shedding is initiated by a global instability in the flow for $Re_D \gtrsim 50$ [5,9], and is characterized by a limit cycle oscillation whereby opposite signed vortices originating from the recirculating fluid region in the near wake of the cylinder alternately advect

downstream [5, 9]. Figure 1.1 shows two snapshots of the prototypical vortex development in the wake of a uniform circular cylinder. The incoming flow stagnates at the front of the cylinder and is redirected around the sides. The boundary layer developing on the surface of the cylinder typically separates near 90° from the front stagnation point (Figure 1.1a) due to the presence of an adverse pressure gradient along the flow direction and the separated shear layers roll-up into vortices in the near wake (Figure 1.1b). The supply of vorticity from each shear layer is eventually cut-off by the shear layer roll-up from the opposing side of the cylinder and the discrete vortices are advected downstream alternately [5, 10, 11]. This periodic process occurs from opposing sides of the cylinder, creating a trail of vortices of opposing senses of rotation in the wake, referred to as a Kármán vortex street [8]. The process of vortex shedding is prevalent in various forms for all bluff-bodies, and the circular cylinder serves as the foundational example of vortex shedding to which the dynamics of more complex bluff bodies may be compared to.

Vortex shedding induces periodic fluctuating forces on the cylinder [12] which may excite so-called Vortex Induced Vibrations (VIV) of the structure [6, 13, 14]. In addition, the fluctuating pressures in the separated shear layers may lead to substantial acoustic noise generation [15–18]. The motivation for the utilization of modified cylindrical geometries in practise is often derived from the need to mitigate these detrimental phenomena and a detailed study of vortex shedding is therefore of both practical and theoretical interest [4, 6, 19–23]. The addition of helical strakes, perforated shrouds, surface wires and bumps, have been shown to suppress VIV [6] and the introduction of step discontinuities in diameter [24, 25] has led to reductions in the magnitude of the RMS lift force and mean drag force, simultaneously.

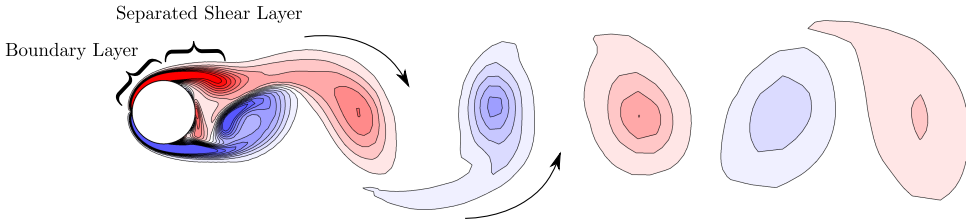

(a) $tU_o/D = 0$

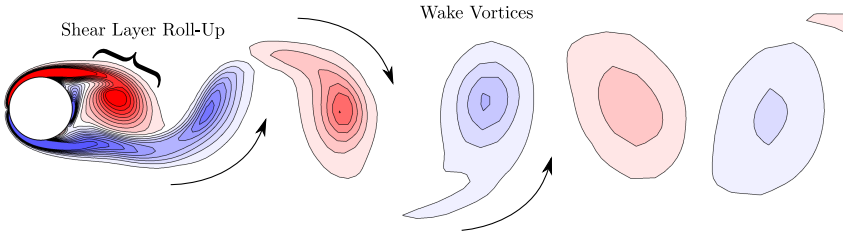

(b) $tU_o/D = 15.3$

Figure 1.1: Vortex development in the wake of a uniform circular cylinder for $Re_D = 300$. Vorticity contours from DNS results obtained by the author.

Geometric modifications from a uniform circular cylinder may also be motivated by fundamental demands of the application. Such is the case for finned cylinders, and their common arrangement into densely packed arrays in order to facilitate the heat transfer in the design of heat exchangers [16–18, 24, 26–35]. The geometry of finned tube heat exchangers may differ significantly depending on the application. A single cylinder may be placed in isolation [17, 18, 24, 26–30], two cylinders may be configured in a tandem arrangement [28], or multiple cylinders may be arranged in arrays [31–35]. The fins affixed to the base cylinder may be either circular [17, 18, 26–30] or rectangular [31–35] in shape, solid [17, 24, 26, 28, 30] or serrated [18, 27, 29], oriented parallel [24, 26–28, 30] to the flow direction or helically wound [17, 18, 27] around the base cylinder. The focus of this thesis

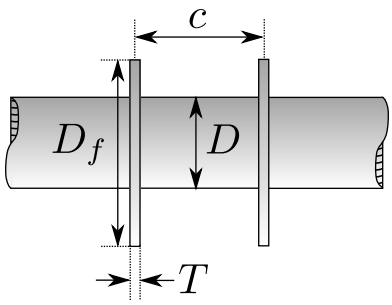

Figure 1.2: Isolated finned cylinder geometry consisting of a base cylinder of diameter D with fins affixed separated by pitch c, having thickness T and diameter D_f.

is on the planar flow development and structural loading of a single, isolated cylinder with circular, parallel fins in cross-flow. Figure 1.2 defines the geometry of the finned cylinder, which may be described using three dimensionless parameters, the pitch ratio c/D, diameter ratio D_f/D, and thickness ratio T/D. Specifically, it is worthwhile to study the salient characteristics of vortex shedding from the geometry, as it is primarily responsible for the induced fluctuating loading on finned cylindrical structures [12]. Hence, vortex shedding may lead to detrimental VIV [6, 13, 14] or resonance and catastrophic failure of the heat exchanging devices caused by the excitation of acoustic modes in its enclosure [16].

While the effect of geometrical changes (c/D, D_f/D, and T/D) to the finned tubes on heat transfer characteristics is well documented [31–35], with a number of design correlations proposed [33, 34], their effects on the fluid-side flow development are not as well understood. Previous studies on isolated finned cylinders have all detected periodic vortex shedding in the wake [17, 18, 24, 26–30]. Numerous studies have found that the coherence of vortex shedding along the span of the cylinder is typically increased by the addition of

fins [17,18,27,28]. However, despite increased shedding coherence, increased acoustic noise generation and fluctuating lift force are not observed concomitantly [17, 18], as would be the case for uniform cylinders [15]. In contrast, the study of Nakamura and Igarashi [24] on finned cylinders with high c/D and T/D shows vortex shedding occurs in discrete cells between each fin spacing and downstream of each fin, implying that the fins disrupt the coherence of vortex shedding across the span. The hot-wire wake velocity measurements of Hamakawa et al. [17,18] and the PIV measurements of Khashehchi et al. [30] for low pitch-ratio finned cylinders $c/D = 0.11 - 0.16$, and $c/D = 0.14$, respectively, indicate significant elongation of the vortex formation length occurs below a critical c/D. This displacement of the vortex formation is reasoned to be the cause of the reduction of fluctuating lift and far-field sound pressures for low c/D [18]. For higher c/D, Hamakawa et. al [18] show that the RMS of the fluctuating lift increases for $c/D = 0.27$ compared to a bare cylinder of base diameter and for $c/D = 0.8$, it is approximately the same. The vortex shedding frequency is reduced by the addition of fins. Mair et. al [26] introduced the definition of the effective diameter D_{eff} for finned cylinders, which when used to non-dimensionalize the shedding frequency data, showed a collapse of the Strouhal number near a constant value $St_{Deff} \approx 0.19$. Ryu et. al [29] advocate the use of the hydraulic diameter D_h instead and Hamakawa et. al [18] have showed better collapse of the Strouhal number data with a modification of the effective diameter definition for a specific Reynolds number and pitch ratio range.

1.1 Study Objectives

The majority of studies on isolated finned cylinders were confined to point measurements in the wake and hence a comprehensive picture of the unsteady flow development has not yet been obtained. As a result, trends reported in the vortex shedding spanwise coherence and fluctuating forces have yet to establish a strong link to the spatio-temporal evolution of the vortex dynamics. Mean drag measurements have not yet been obtained for isolated finned cylinders, and fluctuating lift RMS measurements have not been reported for cylinders with circular, parallel fins. In addition, with various length scales proposed for individual studies, there is need of some clarity regarding vortex shedding frequency scaling laws in the literature.

The specific research objectives are formulated as follows:

1. Determine the effect of fin pitch on salient characteristics of the vortex development in the wake of finned cylinders for fin pitch ratios ($c/D = 1.0, 0.33, 0.083$) at a diameter ratio of 2.0 and fin thickness ratio of 0.028.

2. Characterize the fluctuating lift and mean drag forces acting on the structure, and determine their relation to the flow characteristics.

1.2 Thesis Overview

The thesis is organized as follows: Chapter 2 provides an overview of the relevant literature on the finned cylinders and related geometries. The experimental methodology employed and experimental configuration is described in Chapter 3. An analysis of the results is

given in Chapters 4, followed by concluding remarks and recommendations in Chapters 5 and 6, respectively.

Chapter 2

Literature Review

In this chapter, the state-of-the-art is examined through a review of the published literature pertaining to the isolated finned cylinder and its related geometries. This serves as an instructive, but not exhaustive, discussion of content which will be built upon in this thesis. The review begins by introducing the uniform circular cylinder in Section 2.1, thereby establishing a fundamental basis on vortex shedding and the associated aerodynamic forces. Following that, Sections 2.2-2.3 present research on the related geometries of the porous cylinder and dual step cylinder, respectively. Section 2.4 then reviews previous studies on finned cylinder geometries. Section 2.5 presents relevant literature on planar pressure determination from particle image velocimetry measurements used for the data analysis in the thesis.

2.1 Flow around a uniform circular cylinder

The flow development around a uniform, circular cylinder in uniform cross-flow consists principally of the boundary layer, separated shear layer, and wake regions (Figure 1.1) [2–5]. The boundary layer develops on the surface of the cylinder due to the no-slip condition imposed by the solid boundary, growing along the cylinder surface and eventually separating as a consequence of an adverse pressure gradient. A global instability in the flow leads to the roll-up of the shear layers in the near wake and the development of wake vortices for $Re_D \gtrsim 50$ [5, 9, 36]. The vortices are carried downstream periodically at the dimensionless shedding frequency ($St_D = f_s D/U$) [7], forming a street of alternate signed vortices [8].

2.1.1 Flow topology and vortex dynamics

The reviews of Roshko [4], Williamson [5], and Zdravkovich [6] include in-depth discussions of vortex shedding regimes encountered with changes in Re_D and the reader is referred to these works for a comprehensive review of uniform, circular cylinder vortex development. For $Re_D \lesssim 49$, flow over the cylinder is laminar and steady. The wake is symmetric, comprised of two eddies at the aft of the cylinder. These eddies grow with increasing Reynolds number up to the onset of the primary shedding instability [3]. Following the onset of the shedding instability, for $49 \lesssim Re_D \lesssim 194$, the flow remains laminar and spanwise vortices are shed into the wake (Figure 2.1a). The wake vortex shedding is nominally two-dimensional in this regime; however, three-dimensionalities arise unless laboratory conditions are controlled [9, 38–41]. In particular, oblique shedding typically occurs at angles

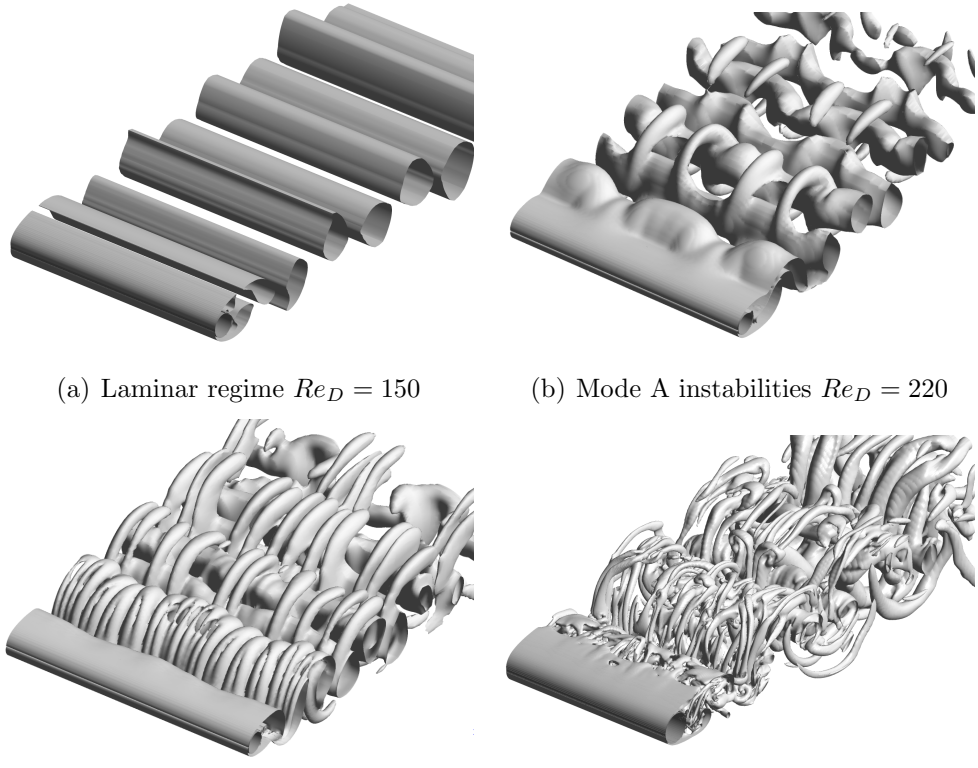

(a) Laminar regime $Re_D = 150$

(b) Mode A instabilities $Re_D = 220$

(c) Mode B instabilities $Re_D = 300$

(d) Shear layer transition regime $Re_D = 1575$

Figure 2.1: Vortex shedding topological regimes. Vortices are visualized using the Q-criterion ($Q = 0.02$) [37]. The data are obtained from direct numerical simulations (a-c) and grid-filtered LES (d) performed by the author.

between $15-20°$, leading to a scatter of up to 10% in measured Strouhal numbers [9]. However, the over-prediction of the shedding frequency caused by measuring velocity traces of the angled vortices may be corrected by multiplying the shedding frequency by the cosine of the shedding angle ($f_S = f_{s,\theta} cos\theta$) [9]. For $190 \lesssim Re_D \lesssim 260$, secondary streamwise vortex structures form along with the primary spanwise rollers due to the onset of three-dimensional flow instabilities and transition to turbulence may occur in the far wake [42].

The onset of the mode A instability occurs between $180 \lesssim Re_D \lesssim 194$, and is characterized by the formation of vortex loops at a spanwise wavelength of approximately $4D$, caused by the growth of spanwise deformations in the vortex cores (Figure 2.1b) [42]. The deformed vortex cores form streamwise vortex connections to subsequently shed spanwise vortices. The mode B instability begins to appear intermittently between $230 \lesssim Re_D \lesssim 250$ and is characterized by smaller scale streamwise vortex pairs manifesting at a wavelength of approximately 1D in the region between the primary vortex cores (Figure 2.1c) [42]. Following the onset of the mode B instabilities, further increases in Re_D lead to increased three-dimensionality and fine scale streamwise vortices forming in the wake region, accompanied by earlier wake transition for $260 \lesssim Re_D \lesssim 1000$. The previously identified secondary coherent structures become more disorganized and deformed in the wake region, forming complex connections with each other and the spanwise vortices. The shear layer transition regime occurs for $1.0 \times 10^3 \lesssim Re_D \lesssim 2.0 \times 10^5$, where turbulent transition develops in the separated shear layers before they roll up into the wake vortices (Figure 2.1d). Transition is identified by the eminent Kelvin-Helmholtz vortices produced by the growth of the convective Kelvin-Helmholtz instability in the shear layers [43, 44]. Beyond $Re_D \approx 2.0 \times 10^5$, the separated shear layer may reattach on one or both sides of the cylinder after undergoing transition, leading to separation bubble regions on the sides of the cylinder and a drastically narrowing of the wake. This regime is the so-called critical regime, or drag crisis [6], where flow reattachement leads to a large reduction in the form drag ($C_{D,p}$) on the cylinder. Above $Re_D \approx 1.0 \times 10^6$, in the post-critical regime, transition occurs in the boundary layer before separation and eliminates the presence of separation bubble reg/ons [5].

In addition to the general topological changes in the vortex development with Re_D, features arise in the spanwise development of the vortices in most regimes. For example, end affected regions develop due to the slowing of the flow near the boundaries of the cylindrical model. The vortex shedding is subdivided into spanwise cells of lower shedding frequency near the ends, leading to a complex development of vortex connections at the cell boundaries as vortices progress in and out of phase [45, 46]. Following wake transition ($Re_D \gtrsim 190$) [5, 42], the appearance of spot-like vortex dislocations [47] partitions the spanwise vortices, whereby similar complex vortex connections between the spanwise vortices are sustained up to $150D$ in streamwise extent in localized areas of the wake. Such dislocations may develop due to slight differences in free-stream conditions or cylinder geometry along the span, but also appear to be a fundamental attribute of turbulent wake transition [47]. Complex vortex interactions and dislocations may also be induced by geometric modifications to the uniform cylinder, as discussed in later sections [25, 47–49].

Concerning the mechanism and dynamics of the spanwise vortex formation that dominates the flow development across most Re_D; the vorticity contained in the wake vortices is generated entirely by the viscous boundary layers (i.e., wall generated vorticity) [50]. Following boundary layer separation, the quasi-steady separated shear layers feed a nearly constant rate of circulation into the near wake and the shear layers eventually roll-up during the vortex formation process. However, following formation, the wake vortices contain significantly less circulation than that generated by their respective shear layer of the same sense [50]. This is known to be attributed to the entrainment of opposite signed vorticity across the wake from opposing shear layers, leading to some equalization of circulation between the wake vortices [51, 52]. To develop the analysis, the boundary layer approxi-

mation yields the rate of circulation production (K_s) in a two-dimensional boundary layer at the point of separation $K_s \approx 0.5U_s^2$ [50], where U_s is the edge velocity at separation. Using Bernoulli's equation with the pressure coefficient at the separation point (C_{ps}), the following estimate can be made for the rate of circulation production in a cylinder shear layer [50]:

$$K_s = \frac{(1 - C_{ps})U_\infty^2}{2} \tag{2.1}$$

As the shear layers roll-up into vortices in the wake, entrainment of vorticity across the wake leads to a lower rate of circulation being convected downstream within the wake vortices. This rate of circulation convection can then be written as:

$$K = \Gamma f_S = \Omega U_\infty^2 \tag{2.2}$$

where Γ is the circulation contained in each individual vortex, and f_S is the vortex shedding frequency. The ratio of the circulation convected in the wake vortices to that generated in the same signed cylinder shear layer (K/K_s) is termed the vorticity deficit ratio and Ω is a dimensionless parameter which can be related to this ratio as follows:

$$K/K_s = \frac{2\Omega}{1 - C_{ps}} \tag{2.3}$$

Experimental investigations have found that the vorticity deficit ratio can vary between 0.4 and 0.7 [1, 50], depending on the Reynolds number. The deficit ratio also varies cycle to cycle, with the strength of the wake vortices not being consistent each shedding cycle

[53, 54]. Of particular importance is the relationship implied by Equation 2.2, that for a constant $\Omega = 0.35 - 0.4$ [50] and a constant free-stream velocity, a higher shedding frequency implies weaker wake vortices.

Beyond initial vortex formation, the vortex dynamics in the wake of the circular cylinder may become complex, particularly in transitional and turbulent flow regimes. As discussed earlier, fine scale streamwise vortex structures, cellular shedding and vortex dislocations can lead to deformed vortex connections in the wake. To facilitate analysis of these vortex flows, it is necessary to realize that the vortices obey some physical constraints. The most fundamental laws governing the dynamics of vortices are Helmholtz' theorems for irrotational flow. The theorems are stated as [55]:

> Helmholtz's 1st Theorem: Vortex lines move at the velocity of the fluid.
>
> Helmholtz's 2nd Theorem: The strength of a vortex tube (Γ), that is the circulation, is constant along its length.
>
> Helmholtz's 3rd Theorem: A vortex tube cannot end in a fluid. It must either end at a solid boundary or form a closed loop.
>
> Helmholtz's 4th Theorem: The strength of a vortex tube remains constant in time ($D\Gamma/Dt = 0$).

While these laws do not hold strictly in real flows due to the action of viscosity, they nevertheless still retain some general utility when perceiving the behaviour of vortices and are still often cited when developing models of vortex dynamics in the wakes of complex geometries [25, 47–49, 56–58]. In particular, viscous dissipation acts to reduce the strength

of the vortices in time, leading to a constant violation of theorem 4 and the dissipation rate depends on the gradients of the surrounding flow field, leading to a violation of theorem 2.

2.1.2 Aerodynamic forces

The flow development around a uniform, circular cylinder induces both steady and unsteady aerodynamic forces on the structure due to viscous and pressure stresses acting at the surface [12, 59, 60]. These forces are known to vary considerably with Reynolds number [12, 59]. Skin drag ($C_{D,v}$) is dominant for low Reynolds numbers [61], while the form drag ($C_{D,p}$) essentially determines the total mean drag (C_D) for higher Re_D [59]. Wieselsberger [59] tabulates drag measurements of high aspect ratio circular cylinders, and his data, covering a considerable Reynolds number range ($5 < Re_D < 5 \times 10^5$), has proved a reliable reference by subsequent studies [61–64]. In the laminar flow regimes, the drag coefficient shows a nearly linear relationship with Reynolds number, C_D decreasing monotonically with increasing Re_D [59, 61]. As the viscous stresses lose their dominance, the drag coefficient levels off at $C_D \approx 1$ over a wide range of Reynolds numbers in the sub-critical flow regimes ($200 < Re_D < 2.0 \times 10^5$). Once critical Reynolds numbers ($Re_D > 2.0 \times 10^5$ [59]) are reached, the so-called drag crisis occurs, whereby boundary layer reattachment may occur, leading to substantial decreases in the mean drag ($C_D < 0.4$ [59]).

Although the mean flow field is symmetric about the wake centre-plane, periodic vortex shedding leads to out of phase fluctuating surface pressures, and a resultant fluctuating lift force coefficient ($C_{L'}$) [12]. Norberg [12] reviews measurements of the fluctuating lift force on uniform, circular cylinders from the onset of vortex shedding up to critical Reynolds

numbers ($47 < Re_D < 2.0 \times 10^5$). Out of phase fluctuating surface pressures on the sides of the cylinder lead to fluctuations in the lift force concentrating at the vortex shedding frequency (f_S). The fluctuating drag force has significantly smaller amplitude compared to the fluctuating lift, with dominant fluctuations in drag occurring at twice the vortex shedding frequency ($2f_S$) as well as low frequency pulsations [54]. From the onset of three-dimensionalities in the wake vortices and into the shear layer transition regime ($190 < Re_D < 6.0 \times 10^3$), the RMS lift is substantially smaller ($C_{L'} < 0.2$) compared to that at other Re_D. Fluctuating lift data for this Reynolds number range are difficult to obtain due to their small magnitude and limitations on the design of the experimental facilities and sensing hardware, leading to a high degree of scatter between studies [12,65,66]. The total RMS lift acting on a finite cylinder length ($C_{L',T}$) is inherently related to the three-dimensionality of the vortex shedding across the cylinder span. Any phase difference between vortex shedding at different spanwise locations leads to reductions in the total RMS lift compared to a sectional lift coefficient ($C_{L'}$). A measure of this three-dimensionality is often expressed by the one-sided spanwise correlation length Λ/D. The relationship between the sectional lift RMS and the lift on a finite segment of length L may be expressed exactly as follows:

$$C_{L',T}/C_{L'} = \frac{1}{L}\left[2\int_0^L (L-s)R_{LL}(s)ds\right]^{1/2} \tag{2.4}$$

$$R_{LL}(s) = \frac{1}{N}\frac{\sum(C_L(0)-\overline{C_L(0)})(C_L(s)-\overline{C_L(s)})}{\sum(C_L(0)-\overline{C_L(0)})^2\sum(C_L(s)-\overline{C_L(s)})^2} \tag{2.5}$$

where $R_{LL}(s)$ is the zero-time-delay correlation coefficient between the fluctuating sectional

lift forces along the span for $0 < s < L$. Due to the difficulty in measuring simultaneous sectional lift forces at multiple spanwise locations, $R_{LL}(s)$ is often approximated by the correlation between pressure measurements at $\theta = 90^\circ$ ($R_{pp}(s)$) or by velocity measurements just outside the wake, near the separated shear layer ($R_{uu}(s)$) [67]. The one-sided correlation length can then be expressed as in Equation 2.6 [68], the integration limits being truncated practically to the length of the cylinder (L):

$$\Lambda = \int_0^\infty R_{LL}(s)ds \approx \int_0^L R_{uu}(s)ds \tag{2.6}$$

The link between characteristics of vortex shedding and changes in the aerodynamic loading is as follows. Measurements near the onset of the shedding instability ($Re_D \approx 49$) [5] where flow can either be steady or unstable [4] show that the onset of the shedding instability acts to decrease base pressure and hence increase mean drag. Moreover, across the entire Reynolds number range, increases in the base pressure (C_{bp}) correlate with increases in vortex formation length (L_f) [4], a measure of the extent of vortex formation in the near wake. A simple model often employed to relate the base pressure to the shear stresses and pressures in the wake [4, 69] involves considering the Reynolds decomposition of the flow field. A picture of the mean flow surrounding a cylinder is then constructed in Figure 2.2. Taking the mean zero velocity streamline as the bounds of a control volume yields the approximate momentum balance shown in Equation 2.7. The base pressure (C_{bp}) at the aft of the cylinder across its width acts in the positive streamwise direction along with both viscous (τ_v) and Reynolds ($\tau_{u'v'}$) stresses acting across the formation length region. These are balanced by the free-stream pressure (p_o) acting across the wake width

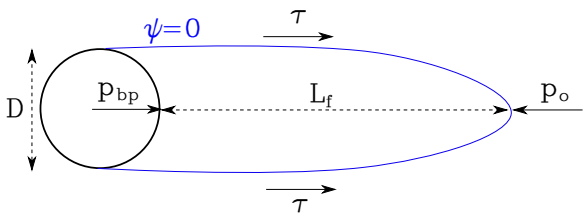

Figure 2.2: Mean recirculation region in the wake of a circular cylinder, adapted from Roshko [4], Williamson [5] and Arie and Rouse [69]

.

in the opposing direction.

$$\oint_{\psi=0} p dy + \oint_{\psi=0} \tau dx = 0 \tag{2.7}$$

When vortex shedding occurs, the Reynolds stresses dominate the viscous stresses [5] and the momentum balance may be simplified by substituting in the base pressure coefficient to:

$$(p_b - p_\infty)d = 2\tau L \tag{2.8}$$

$$L/d = -\frac{1}{4}\frac{C_{bp}}{1 - C_{bp}}\left(\frac{U_s^2}{\overline{u'v'}}\right) \tag{2.9}$$

This relation shows that the base pressure increases as the formation length increases or the Reynolds stresses decrease. However, it has been noted that this model is inadequate for the exact determination of variables, due to the arbitrary selection of some parameters [4,5]. Given that, a good experimental fit for the drag force is directly dependent on only the base pressure (Equation 2.10) [50], it can be concluded that changes in base pressure correlate directly to the mean drag force.

$$C_D = C_{pf} - C_{bp} = 0.88(1 + 0.11C_{bp}) - C_{bp} \tag{2.10}$$

Regarding the lift RMS ($C_{L'}$), it is known to increase with decreases in vortex formation length [5, 70], as unsteadiness in the velocity field close to the cylinder caused by vortex formation leads to higher surface pressure fluctuations. It has also been observed that magnitudes of the mean drag and fluctuating lift force are dependent on each other [12], supporting the relationships implied in the discussion so far that $C_D \propto -C_{bp}$, $C_{bp} \propto L_f$, and $C_{L'} \propto -L_f$.

2.1.3 Aspect ratio and end effects

The flow development around a uniform, circular cylinder is known to be affected by surface roughness, flow-uniformity, turbulence intensity, flow blockage, cylinder aspect ratio, and cylinder end conditions [38, 41, 71, 72]. It's important in the design of experiments that these factors are considered, and their effects diminished and accounted for where possible.

In laboratory experiments, end plates affixed to the ends of the cylinder models are often used to minimize finite aspect ratio effects on the flow development. The works of Stansby [73] and Mair & Stansby [26] suggest the optimum position and size of end plates to minimize the extent of the end affected region along the span. West and Fox [72] studied the effects of changing the aspect ratio (L/D) of the cylinder contained between end plates. They found that end cells of lower shedding frequency develop due to the lowering of the convective velocities of vortices near the boundary layer growth on the end plate surface [38,72,73]. The spanwise extent of the end cells is approximately $3.5D$ for $1.6\times10^4 <$

$Re_D < 1.3 \times 10^5$ [72, 73], and hence to achieve nominally two-dimensional vortex shedding at the mid-span of the cylinder, the aspect ratio must be greater than 7. The work of Norberg [41] gives more conservative estimates for the minimum aspect ratio for unaffected flow, recommending $L/D > 50$ in the shear layer transition regime $4.0 \times 10^3 \leq Re_D \leq 1.0 \times 10^4$ based on both Strouhal number and base pressure measurements converging with respect to aspect ratio at the midspan. However they utilized an suboptimal end plate configuration, with the model mounted at the exact centre [41] instead of offset in the upstream direction [26, 73]. For $L/D < 7$, bistable, irregular flow develops and vortex shedding is intermittent [41].

Compared to a cylinder with end plates, a wall junction end condition leads to larger end affected regions of the vortex shedding, as the wall boundary layer is much thicker. Indeed, studies have found for $L/D < 20$, the end cells merge, with shedding frequency decreasing with further decreases in aspect ratio [38, 74] and the alternate shedding of vortices transitioning to symmetric shedding below $L/D \approx 6$ [74]. For cylinders with two free-ends, a similar single cell vortex shedding is observed below $L/D \approx 10 - 30$ [41,45,75]. In order to obtain nominally two-dimensional flow at the mid-span, the aspect ratio must exceed these values.

Numerous studies [41,59,75] finds that decreasing the aspect ratio below $L/D = 50$ leads to a steady increase in base pressure, lowering of the shedding frequency, and enlargement of the vortex formation region for $Re_D \lesssim 8.0 \times 10^3$. This agrees with observations of the end effected regions slowing the flow and enlarging the vortex formation region [38, 41]. However, for higher Re_D, Norberg [41] finds this trend reverses, with mean loading on the cylinder increasing with decreasing L/D. Since the mean drag and fluctuating lift forces

are dependent on each other [76], the trend in the fluctuating loads with L/D is similar, confirmed by measurements at higher $Re_D = 1.0 \times 10^4 - 1.0 \times 10^5$, with increases in $C_{L'}$ observed [70, 76, 77].

2.2 Porous cylinders

The addition of porous media to the outside of cylinders has been utilized to enhance heat transfer characteristics [30] and as a passive flow control method for reducing acoustic noise generation [78, 79]. The geometry comprises of a solid base cylinder of diameter D with an outer shell of porous media extending to a diameter of D_o, (Figure 2.3). The porous media is typically a metallic foam or porous urethane [30, 78–80]. The flow development about porous cylinders is expected to share similarities to that of finned cylinders, considering a finned cylinder may be thought of as a type of structured porous media. Sueki et al. [78] investigated the porous cylinder in cross-flow for $4.6 \times 10^4 < Re_D < 8.3 \times 10^4$. For the investigated porosity $\beta \approx 0.97$ and diameter ratio $D_o/D = 1.8$, they found wake vortex shedding is completely suppressed. A low velocity recirculation region in the wake extended significantly further downstream than that observed for an equivalent uniform cylinder (D_o) and the shear layers emanating from the sides of the cylinder were stabilized, besides the formation of Kelvin-Helmholtz vortices, leading to substantially reduced noise generation. For $1.0 \times 10^3 \leq Re_D \leq 1.0 \times 10^4$, $D_o/D = 1.38$, and $\beta = 0.85 - 0.97$, Khaleschi et al. [30] also found a large low velocity region in the wake, and their Proper Orthogonal Decomposition (POD) analysis of the planar PIV measurements indicated that less energy is contained in the first two POD modes describing the vortex shedding phenomenon, compared to

that of a uniform cylinder and finned cylinder [30]. Naito and Fukagata [79] investigated a larger range of Reynolds numbers ($100 \leq Re_D \leq 1.0 \times 10^5$) for $D_o/D = 1.2$ and 1.5, and $\beta = 0.8 - 0.95$, finding the same suppression of vortex shedding for $Re_D = 1.0 \times 10^5$. However, for lower Reynolds numbers ($100 \leq Re_D \leq 3900$), vortex shedding is sustained in the wake. The wake stabilization is attributed to the low energy fluid passing through the porous media, which is subject to high dissipation, being injected into the near wake. In combination with the slip-velocity at the porous outer surface decreasing the vorticity in the shear layers, these mechanisms lead to the observed wake stabilization [79]. The lift RMS on the porous cylinder is reduced compared to a uniform cylinder, with RMS lift decreasing with increasing Reynolds number [79]. Mean drag on the porous cylinders is increased in all cases, and is more pronounced for lower Reynolds numbers [79].

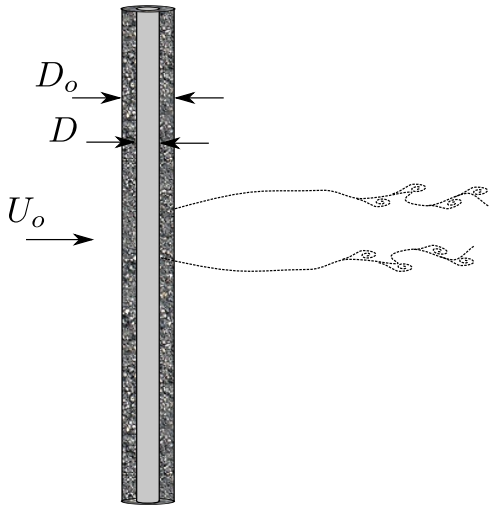

Figure 2.3: Porous cylinder in cross-flow consisting of a solid base cylinder of diameter D and a layer of porous media extending to diameter D_o.

2.2.1 Base blowing and suction

Fransson et al. [80] studied the porous cylinder with applied suction and blowing for $Re_D = 8.3 \times 10^3$. They find a linear relationship between the rate of blowing or suction applied (Ψ) and the vortex formation length (L_f), with the latter increasing for higher blowing coefficients and decreasing for higher suction coefficients. Blowing ($\Psi > 0$) causes earlier boundary layer separation, while suction ($\Psi < 0$) delays separation. Beyond a critical level of suction, up to 70% drag reduction can be achieved, with the wake development resembling that at critical Re_D. Blowing acts to increase the mean drag, despite acting to increase the base pressure. Instead, the pressure on the cylinder surface between $\theta = 60 - 90^\circ$ is higher and contributes to the increase in mean drag. Fransson et al. [80] find the shedding frequency decreases for blowing and increases for suction, which is opposite to the trend reported for suction applied to a blunt trailing-edge body by Hammond & Redekopp [81].

2.3 Dual step cylinders

When considering the finned cylinder, which consists of discrete changes in diameter across its span, it is useful to consider the dual-step geometry, which focuses on the flow development of a single 'fin' of thickness (L) and diameter (D) affixed at the mid-span of a uniform base cylinder (d), as shown in Figure 2.4. Williamson [47] investigated low aspect ratio ($L/d = 0.5$) dual step cylinders for $1.1 \leq D/d \leq 2$ in order to study vortex dislocations in the wake of circular cylinders. He found that dislocations occur at the boundaries between the vortices shed in the large cylinder wake and the small cylinder

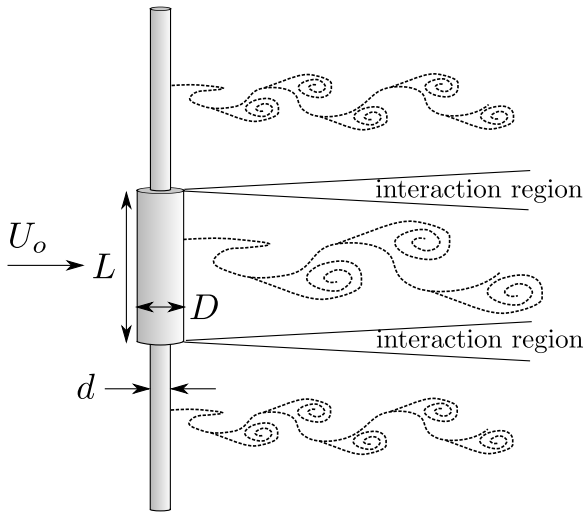

Figure 2.4: Dual-step cylinder in cross-flow consisting of a large cylinder of diameter D and length L, and small cylinder of diameter d.

wake (Figure 2.4) [47, 48, 82]. The dislocation frequency is equal to the beat frequency, $f_S - f_L$ [47], where f_S is the shedding frequency in the wake of the small cylinder and f_L is the dominant frequency in the wake of the large cylinder. Generally, the large cylinder wake topology depends on the aspect ratio of the large cylinder (L/D), the diameter ratio (D/d), and Re_D [47, 48, 82]. Morton & Yarusevych [48, 82] investigated the flow past dual step cylinders for $Re_D = 1050$ and 2100, $0.2 \leq L/D \leq 17$, and $D/d = 2$. At low aspect ratios, $L/D < 1$, vortex shedding does not occur from the large cylinder, instead vortex filaments simply connect the small cylinder vortices across the large cylinder wake. The convective velocity of the filaments is reduced due to the disturbance in the flow induced by the large cylinder, which results in periodic vortex dislocations terminating with small cylinder half-loop vortex connections [48,82]. At higher aspect ratios, $2 \leq L/D \leq 6$, vortex shedding in the large cylinder wake is less coherent, with large cylinder vortices forming

vortex loops while vortices in the small cylinder wake form continuous half-loop connections. For $L/D > 8$, vortex shedding occurs in the large cylinder wake in a single cell at a constant frequency, which increases with increasing aspect ratio. Beyond $L/D = 15$, shedding in the large cylinder wake at the mid-span approaches that of a uniform cylinder, while end cells form near the discontinuities in diameter. McClure at al. [25] report that simultaneous reductions in the mean drag ($\approx 5\%$) and lift RMS ($\approx 80\%$) for the laminar flow regime ($Re_D = 150$) can be achieved for a cylinder by affixing a larger diameter cylinder of approximate dimensions $L/D \approx 1$ and $D/d \approx 1.5$ at the mid span. The reduction in C_D is produced due to the base pressure increasing on the aft of the large cylinder which is linked to strong secondary spanwise flows induced by vorticity generated at the step discontinuities impinging near the mid-span of the large cylinder. Reductions of lift RMS are attributed primarily to the elongation of the vortex formation length as well as the decrease in spanwise coherence due to the complex vortex interactions and cellular shedding in the wakes of the large and small diameter cylinders.

2.4 Finned cylinders

The geometry of a finned cylinder may be described by the following dimensionless parameters: fin pitch ratio c/D, fin thickness ratio T/D, and fin diameter ratio D_f/D (Figure 2.5). Finned-tube cylinders with small pitch ratios (c/D) are typically used in air conditioning and radiator units due to their enhanced heat transfer characteristics [83], while refrigerators and freezers often utilize flat plate finned-tube heat exchangers with large pitch ratios due to their improved performance during frosting and defrosting conditions. Practical

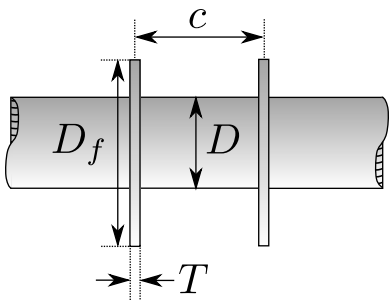

Figure 2.5: Isolated finned cylinder geometry consisting of a base cylinder of diameter D with fins affixed separated by pitch c, having thickness T and diameter D_f

ranges of geometrical parameters fall within: $0.011 \lesssim T/D \lesssim 0.15$, $0.06 \lesssim c/D \lesssim 0.8$, and $1.2 \lesssim D_f/D \lesssim 2.4$ [83, 84]. In addition to improving heat transfer characteristics, the addition of fins or helical strakes has been found to suppress VIV [6, 14]; however, acoustic characteristics may vary in tube banks, where fins have been shown to increase resonance in some cases [16, 28].

2.4.1 Isolated finned cylinders

Isolated finned cylinders in uniform cross-flow with either solid or serrated fins affixed in parallel (Figure 2.6a) or wound helically (Figure 2.6b) along the span have been shown to exhibit similarities in flow development over a wide range of fin thickness ratios (T/D), pitch ratios (c/D), diameter ratios (D_f/D), and Reynolds numbers (Re_D) (Figure 2.5) [17, 18, 24, 26–30]. Specifically, von Kármán vortex shedding has been observed in all investigations to date [17, 18, 24, 26–30] within the following range of parameters for finned cylinders: $0.0125 \leq T/D \leq 0.064$, $0.06 \leq c/D \leq 1.0$, $1.2 \leq D_f/D \leq 2.0$, and $1.0 \times 10^3 \leq Re_D \leq 1.85 \times 10^5$. Table 2.1 lists previous studies on isolated fin cylinders along with the

parameter range investigated and experimental methods employed.

The studies of Mair et al. [26] and Ziada et al. [27] report that the velocity fluctuations at the vortex shedding frequency are enhanced in the wakes of finned cylinders, compared to that of a base diameter uniform cylinder (D). They compare the streamwise velocity spectra, which exhibit a sharper, higher magnitude spectral peak at f_S [26, 27], and the velocity traces, which exhibit lower random frequency variation in time. Mair et al., conjecture that this is due to an increase in the two-dimensionality of the vortex shedding with the addition of fins [26]. Along this line, Hamakawa et al. [18] and Ziada et al. [27] find that the addition of fins leads to more correlated vortex shedding along span in comparison to uniform cylinders. In contrast, for a multi-step cylinder with comparatively large pitch ratio ($2 < c/D < 9$) and thickness ratio ($0.33 < T/D < 4$), Nakamura & Igarashi [24] present flow visualization that shows discrete vortex shedding cells between each fin pitch, implying less correlated vortex shedding along the span. Moreover, studies measuring profiles of turbulence intensity in the wake [18, 28] find that the addition of fins leads to a decrease in the maximum turbulence intensities in the wake, and the POD analysis of Khashehchi et al. [30] found the strength of the coherent structures to be slightly less for the finned cylinder compared to a uniform cylinder of diameter D_f.

Typically, the addition of fins acts to progressively decrease the shedding frequency from that of a bare tube [17, 26, 27], however Ryu et al. observe that the shedding frequency may be marginally increased by the addition of fins at large c/D, as they confine the flow to accelerate over the cylinder [29]. In order to scale the shedding frequency data, Mair et al. [26] introduced the definition of the effective diameter (D_{eff}) based on equating the volume of the finned cylinder to that of a uniform cylinder of diameter D_{eff} (Equation

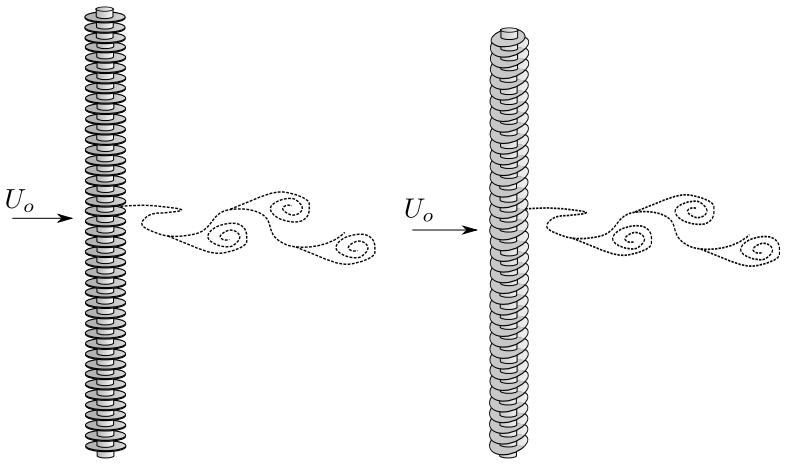

Figure 2.6: Isolated finned cylinders in cross-flow: (a) circular, solid, straight fins and (b) circular, solid, helically wound fins

2.11). A number of subsequent studies find that the Strouhal number based on the effective diameter (St_{Deff}) leads to a reasonable collapse of the shedding frequency data over a wide range of Re_D and geometrical parameters (e.g., [17, 26, 27]).

$$D_{eff} = \frac{(c-T)D + TD_f}{c} \tag{2.11}$$

In studies on cylinders with serrated helically wound fins [18], once a minimum c/D was reached, the shedding frequency from the cylinder decreases to approximately that of a uniform cylinder with diameter D_f instead of scaling with the effective diameter D_{eff}. When this is the case, flow separation is observed at the fin diameter. Hamakawa et al,. [18] modified the definition of the effective diameter to $D_{eff} = D_f$ for a specific pitch ratio and Reynolds number range ($c/D \leq 0.16$ and $7.6 \times 10^4 \leq Re_D \leq 1.9 \times 10^5$) to fit the

experimental data. Alternatively, Ryu et al. [29] find that scaling by the hydraulic diameter D_H (Equation 2.12) provides a better collapse of the frequency and wake profile data for flow over cylinders with serrated fins with relatively small pitch ($0.08 \leq c/D \leq 0.17$) and diameter ratios ($1.0 \leq D_f/D \leq 1.82$).

$$D_H = D_f - 4\frac{(c-T)(D_f-D)}{c-T+D_f-D} \tag{2.12}$$

The spanwise coherence of vortex shedding is of interest for the finned cylinder due to its effect on the fluctuating loading ($C_{L'}$) and far-field oscillating sound pressure levels (SPL) manifested from the vortex shedding process. The coherence along the span of a bluff body is often estimated experimentally by the cross correlation of simultaneously obtained velocity signals in the wake. Ziada et al. [27] found that the addition of fins was generally accompanied by an increase spanwise coherence. However, variations in the spanwise coherence were detected at different orientation angles, due to a non-uniform spanwise waviness in the manufactured finned cylinder models. In addition, for the lowest pitch ratio model studied ($c/D = 0.095$), a reduction in coherence length was detected compared to a uniform cylinder of diameter D. Hamakawa et al. [17, 18] found similar results, with the addition of fins increasing the coherence of shedding compared to uniform cylinders of diameter D and D_f. The coherence was largest for $c/D = 0.27$, and decreased for lower pitch ratios of $c/D = 0.16$ and 0.11.

Typically, increased shedding coherence leads to increased fluctuating forces ($C_{L'}$) [12] and acoustic noise generation [15], however Hamakawa et al. [18] find substantial reductions in fluctuating loads and far-field sound pressures for finned cylinders of low pitch ratios

Table 2.1: Compilation of experimental studies on isolated finned cylinders

Authors	Re_D	D_f/D	T/D	c/D	Fin Geometry	Experimental Techniques
Mair et al. [26]	16,000-46,000	1.2,1.4	0.0224-0.064	0.06-0.8	solid, straight	Hot-wire
Ryu et al. [29]	17,000-185,000	1.0-1.82	0.02-0.025	0.08-0.17	serrated, helical	Hot-wire, flow viz
Ziada et al. [27]	26,100-49,800	2.0	0.033	0.095-0.19	serrated, helical	Dual hot-wire
Hamakawa et al. [17]	11,000-63,000	1.8	0.038	0.16-1.0	serrated, helical	Hot-wire, flow viz
Nakamura & Igarashi [24]	3,000-38,000	1.2-2.0	0.33-4.0	2.0-9.0	solid, straight	Force balance, flow viz, surface pressures
Hamakawa et al. [18]	5,300-110,000	1.8	0.038	0.11-0.8	serrated, helical	Hot-wire (x-y plane), force balance, microphones
Eid & Ziada [28]	16,000-110,000	1.6	0.0254	0.067-0.29	solid, straight	Hot-wire, microphones
Khashehchi et al. [30]	1,000-10,000	2.0	0.0125	0.14	solid, straight	PIV, flow viz

($0.11 \leq c/D \leq 0.16$) despite higher spanwise correlations between velocity signals in the wake. This is attributed to the vortex formation region being displaced downstream for low c/D, and the associated larger stagnant flow region in the near wake where fluctuating pressures near the cylinder and in the shear layers are low [5]. For low c/D models ($c/D \leq 0.16$), lift RMS is reduced compared to a uniform cylinder of diameter D_f, and for high c/D models ($c/D \geq 0.27$), lift RMS increases in comparison to a uniform cylinder of diameter D, and is nearly matching for $c/D = 0.8$. Eid & Ziada [28] also observe an

attenuation of acoustic noise generated from finned cylinders compared to uniform cylinders ($0.067 \leq c/D \leq 0.29$). The sound pressures are attenuated more substantially for lower fin pitch ratios, despite the strength of shedding being comparable between models. Nakamura and Igarashi [24] study finned cylinders of relatively large thickness ($0.33 \leq T/D \leq 4.0$) and pitch ($2.0 \leq c/D \leq 9.0$) ratios and find substantial drag reductions ($\approx 20\%$) compared to a uniform cylinder, which they attribute to a Reynolds number specific effect of flow reattachment on the sides of the fins.

2.4.2 Multiple finned cylinder arrangements

In many heat exchanger designs, finned cylinders may also be arranged in tandem [28, 85], in-line [85], staggered [85], or in a compact, parallel array referred to as a tube bundle or tube bank [31–34]. In such cases, the geometry is not only defined by the fin parameters; thickness ratio (T/D), pitch ratio (c/D) and diameter ratio (D_f/D) (Figure 2.5), but also the number of tube rows (N), longitudinal spacing (S_l), and transverse spacing (S_t), in addition to. Several correlations for the pressure drop coefficient and heat transfer coefficient have been proposed based on the available experimental data for plate fin and tube arrays [31–34]. For large spacing ratios, independent wake shedding occurs for each cylinder [28,84], whereas for smaller spacing ratios the wakes may form single vortex street, synchronized or coupled streets [84]. As well, for closely spaced tube bundles, the geometry may considered like a porous medium, in which vortex shedding is suppressed within the bundle geometry [84]. However, Nemoto et al. [16] studied the acoustic characteristics of finned tube bundles and found that resonance can be excited, indicating some periodic

flow activity within the bundle. Moreover, Hamakawa et al. [86, 87] find high frequency activity within the tube bank ($St_{Deff} \approx 0.4$) and lower frequency activity excited in the wake ($St_{Deff} \approx 0.2$), which is presumably related to von Kármán vortex shedding. Despite the connection between acoustic resonance and flow characteristics to vortex shedding in the wake not being well-established [86,87], it seems apparent that vortex shedding activity persists throughout the studies multiple cylinder arrangements [16,28,84–87]. Presumably, relationships identified for the isolated finned cylinder studied herein may be extended to multiple cylinder arrangements.

2.5 Pressure PIV

With the measurement of the instantaneous planar velocity field $\vec{u}(x, y, t)$ from PIV and the extraction of its spatial and temporal derivatives, the pressure gradient field may be calculated from the two-dimensional Navier-Stokes equation:

$$\nabla p(x, y, t) = \mu \nabla^2 \vec{u} - \rho(\frac{\partial \vec{u}}{\partial t} + \vec{u} \cdot \nabla \vec{u}) \tag{2.13}$$

The problem of integrating this field to obtain the planar pressure field $p(x, y, t)$ is subject to a variety of practical, numerical, and theoretical complications and limitations [88]. However, resolving the pressure field both spatially and temporally represents tremendous analysis potential in experimental work.

Baur and Kongeter [89] utilized an iterative spatial marching scheme in order to integrate the pressure gradient over the domain. At each time step, the pressure field is

initialized as $p(x, y) = 0$. The pressure gradient calculated from the two-dimensional Navier Stokes equations (Equation 2.13) is then spatially integrated along sequential rows, starting at an arbitrary corner of the domain. The pressure values at each node are updated based on the known pressure gradients and pressures at the surrounding nodes. Successive iterations alternate the direction and starting corner of the spatial integration scheme in order to avoid the inhomogeneous propagation of errors.

Dabiri et al. [90] propose a simple line integration technique developed for relatively quick calculation of pressure fields. The pressure gradient is first integrated along the outer boundary of the domain and the resulting pressure values along the boundary are stored. The pressure at any point in the domain $p(x, y)$ is then calculated based on the average of eight symmetric line integrations through the domain from that point to the outer boundaries. The integrations are initially performed iteratively only on the boundary points, until the boundary pressures reach acceptable convergence, and then the internal pressures are calculated in a single loop through the domain. Liu and Katz [91] developed the omni-directional line integration technique, in which internal domain pressures are calculated based on the average of many line integrations which pass through the point. The pressure is first integrated along the outer boundary. A loop is then performed around the outer boundary, during which a line integration is performed from every point on the outer boundary to every other point on the outer boundary. Every time a line integration passes an internal point, the pressure is stored at that point. Once all the line integrations are performed, the pressure median of the saved pressures at each point determines the new pressure value. The pressures at the boundaries are then updated and the method is iterated until converged. The inhomogeneous propagation of pressure error near the

boundaries of the domain was reduced by performing the line integrations from a virtual boundary outside of the domain instead of originating directly from the domain boundary [91].

Rather than integrating the pressure gradient directly, Gurka et al. [92] solved the pressure Poisson equation in the fluid domain. The pressure Poisson equation is derived from the divergence of the Navier-Stokes equations (Equation 2.14). Using a standard 5-point second order central difference scheme for the Laplacian of the pressure field, a sparse system of equations is obtained for the nodal pressures and are solved simultaneously over the domain.

$$\nabla^2 p = 2\rho\left(\frac{\partial u}{\partial x}\frac{\partial v}{\partial y} + \frac{\partial v}{\partial x}\frac{\partial u}{\partial y}\right) \tag{2.14}$$

Charonko et al. [93] compared the Poisson solver, omni-directional and iterative spatial integration schemes, utilizing analytical solutions for a pulsatile flow and decaying vortex subjected to uncorrelated velocity field noise to test the random error sensitivity of the methods. Experimental data from internal flow in a diffuser was used to validate the methods and compare time-filtering methods. The effect of conservative formulations of the Navier-Stokes equations, which retain terms containing out-of-plane gradient ($\partial w/\partial z$) calculated form the continuity equation, was investigated on the accuracy of the pressure calculation. The findings indicate that the virtual-boundary, omni-directional integration method [91] performed overall the best with the standard two-dimensional Navier-Stokes equations, with errors in the pressure field between 1-100%. However, an optimum method was not established and was dependent on the type of flow. Analysis of different filter-

ing approaches (low-pass filtering, Lagrangian minimization with respect to the continuity equation, and POD smoothing) indicates that POD based filters perform the best, reducing errors in the pressure field evaluation by up to an order of magnitude. Violato et al. [94] compared the errors associated with Eulerian and Lagrangian techniques for evaluating the material acceleration and find Eulerian methods were suitable for higher time steps compared to Lagrangian methods ($\Delta t_{Lag}/\Delta t_{Eul} > 3$). De Kat and van Oudheusden [95] present theoretical considerations on error propagation and frequency response of derived pressure fields for both Eulerian and Lagrangian approaches and conclude that interrogation window size should be 5 times smaller than the smallest spatial wavelengths of the flow structures ($WS/\lambda_x < 0.2$) and the acquisition frequency should be 10 times higher than the corresponding flow frequency ($f_{acq} > 10 f_{flow}$) in order to resolve the flow features with less than 10% peak modulation in the pressure field.

Chapter 3

Experimental methodology

In this study, cylinders with straight, circular fins were studied experimentally in the water flume facility at the University of Waterloo. Experiments in the same facility have previously formed the basis of the works of Bansal [96], Morton [97, 98], and Kheirkhah [99] on cylindrical bluff-body aerodynamics and VIV. Experiments were conducted on three finned cylinder models and two uniform cylinder models. The diameters of the uniform cylinders match the base (D) and fin (D_f) diameters to allow comparison with finned cylinders. The three finned cylinders investigated have pitch ratios $c/D = 0.083, 0.33, 1.0$, selected to cover the entire range of pitch ratios used in practical applications [18, 26, 27, 83]. The Reynolds number was $Re_{Df} = 2040$. A combination of experimental techniques were employed in order to obtain a comprehensive description of the planar flow development and structural loading characteristics on the experimental models. Specifically, planar, time-resolved particle image velocimetry measurements, laser doppler velocimetry measurements, and force balance measurements.

3.1 Experimental facility

A diagram of the water flume facility at the University of Waterloo is shown in Figure 3.1. Water is recirculated through the test section from a large reservoir beneath the laboratory floor. A pump elevates the fluid from the reservoir into a head tank maintained at a constant water level. From the head tank, a pipeline carries the water into the settling chamber, with the flow rate controlled by a gate valve. Flow recirculation in the settling chamber caused by the injection of fluid from the pipeline is mitigated by a vertical array of tubes at the bottom of the chamber and a smaller secondary injection pipeline. The water exiting the settling chamber passes through a series of flow conditioning elements. First, the flow passes though a plastic grid and two fine wire turbulence screens meant to improve uniformity and reduce turbulence intensity in the flow. The flow then passes through a 2.42° diffuser section and enters a honeycomb flow straightener, aluminium grid and an additional five turbulence screens before entering the test section. The test section dimensions are $1.2m$ wide (C_w) and $2.4m$ long (C_l) with one vertical wall of the test section made from $19mm$ thick glass for optical access. The flow then exits though a perforated plate before recirculating into the water reservoir. The plate design and gate valve settings maintain a constant water level of $0.8m$ (C_h) in the test section, and a mean free-stream velocity of $86.5mm/s$ (U_o). The specifications of the turbulence screens and free-stream characterization are presented in Appendix A. Measurements in the free-stream demonstrated a test section turbulence intensity of $|u'| < 1\%$ and flow non-uniformity $\alpha_u < 4\%$.

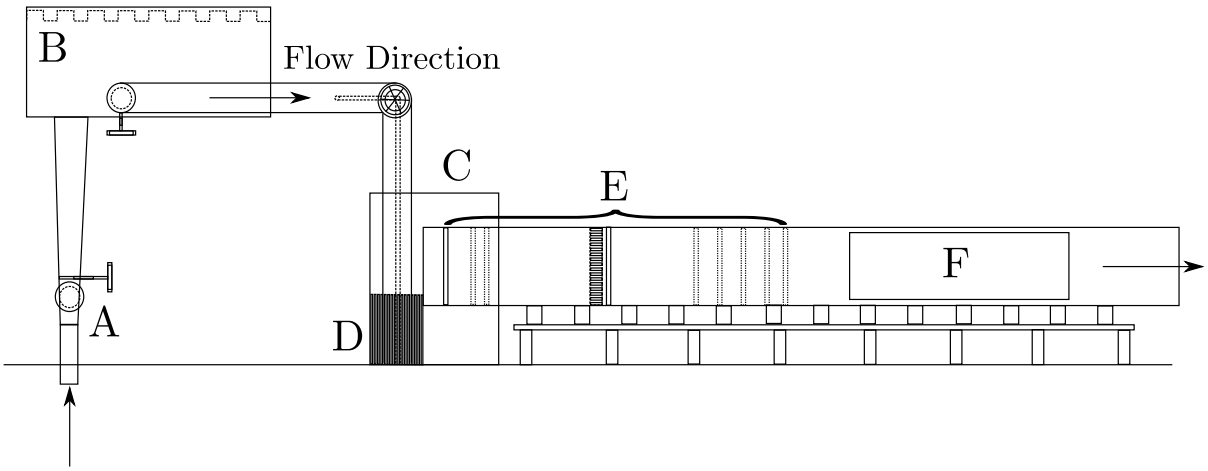

Figure 3.1: University of Waterloo water flume facility: (A) head tank pump, (B) head tank, (C) settling chamber, (D) array of vertical flow conditioning tubes, (E) flow conditioning grids, honeycomb and screens, (F) test section.

3.1.1 Model specifications

Three finned cylinder models of varying pitch ratio (c/D) were manufactured along with two uniform cylinder models of base and fin diameter, corresponding to $Re_D = 1020$ and $Re_{Df} = 2040$, respectively (Figure 3.2). The upper limit on the Reynolds number of models in the water flume facility wass set by maximum acceptable model blockage ratios, with $< 3\%$ solid blockage corresponding to $Re_{Deff} < 2250$. The lower limit was set by resolution considerations associated with the laser based flow diagnostics, imaging hardware and force balance, typically requiring $Re_D \gtrsim 500$ [97,98]. The finned cylinder models were constructed using a stainless steel support cylinder of diameter (D_b) $0.375in$, with aluminium fins of thickness (T) $0.021in$ and diameter (D_f) $1.5in$ slid between aluminium spacers of base diameter (D) $0.75in$. The length of the spacers (c) varied between $0.0625in$ and $0.75in$ depending on the model. The resulting dimensionless geometric and flow parameters for

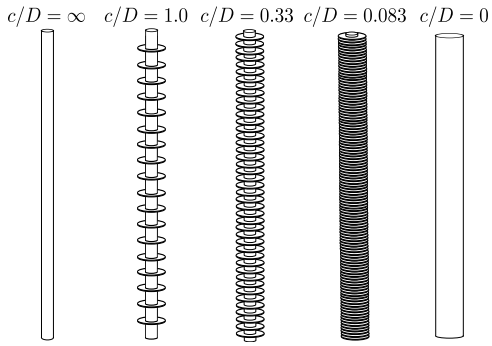

Figure 3.2: Illustration of all experimental models investigated.

each experimental model are included in Table 3.1. The pitch ratios $c/D = 0.083 - 1.0$, fin thickness ratio $T/D = 0.028$ and diameter ratio $D_f/D = 2$ were selected from the practical range of parameters for finned-tube heat exchangers [18, 26, 27, 83]. The fins were punched from aluminium sheet, deburred, and compressed together on a jig such that the outer diameter could be turned down to $1.5in$ with sharp, parallel edges. The aluminium spacers were bored and reamed out from aluminium rod and the outer surfaces of the fins and spacers were sanded with 600 grit sand paper and finished with aluminium paste polish. The inner diameters of the fins and spacers were sized to ensure a tight sliding fit on the support cylinder (Figure 3.3). Once assembled, a section near the midspan of the model was spray painted matte-black in order to mitigate reflections in PIV measurements.

The finned cylinder assembly mounted in the water flume free-stream is shown in Figure 3.3. The models were offset $y = -0.1m$ from the midspan of the test section to accommodate wake velocity measurements with the fixed focal length LDV system used in this study. The cylinders were oriented vertically and perpendicular to the incoming free-stream. All models were mounted between two circular end plates of $10.5in$ $(7D_f)$

Table 3.1: Parameters pertaining to the uniform and finned cylinders manufactured for experimentation.

Model	c/D	T/D	D_f/D	D_{eff}/D	Re_{Deff}	L/D_{eff}
Uniform Cylinder	∞	-	-	1.0	1020	21.3
Uniform Cylinder	0	-	-	2.0	2040	10.6
Finned Cylinder	0.083	0.028	2.0	1.25	1277	17.0
Finned Cylinder	0.33	0.028	2.0	1.08	1100	19.8
Finned Cylinder	1.0	0.028	2.0	1.03	1048	20.7

diameter, with the model positioned $1D_f$ upstream of the end plate center, following the recommendations of Stansby [73] and West and Fox [72]. The end plates were $1/8in$ thick and chamfered 60° on the outer edges in order to cut the incoming flow such that thin boundary layers form on the inward faces. However, the back edges of the end plates were ground parallel in order to minimize image distortions when optically accessing the wake area from above. The models were mounted $0.2m$ from the bottom of the flume and $0.2m$ from the free surface, and when mounted between the end plates, the compressive force transferring axially ensured the fins and spacers remained stationary and perpendicular to the cylinder axis. The vertical alignment of the models and the horizontal alignment of the end plates was performed in air and verified with a laser level to be within ± 0.1 deg. The aspect ratio based on the effective diameter of each model (L/D_{eff}) was large enough such that nominal two-dimensional flow would develop in a region surrounding the mid-span of the models, as per the recommendations of Stansby [73] and West and Fox [72].

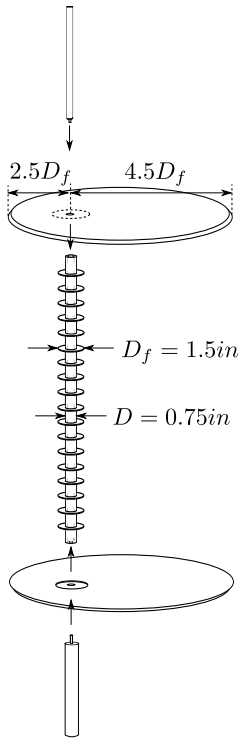

Figure 3.3: Experimental assembly of a finned cylinder for $c/D = 1.0$.

3.2 Particle Image Velocimetry (PIV) Measurements

Two-component, Time-Resolved Particle Image Velocimetry (TR-PIV) measurements were employed to estimate the planar velocity fields in the wake. The general operating principle of the PIV measurments is covered in detail by the works of Willert and Gharib [100], Westerweel [101], and Raffel et al. [102]. In this work, PIV measurments were obtained in horizontal and vertical planes using a LaVision PIV system comprising of two high speed, $1024 \times 1024px$ Photron cameras and a high repetition rate Nd:YLF pulsed laser. The horizontal $x - y$ plane PIV experimental set-up is shown in Figure 3.4. The two

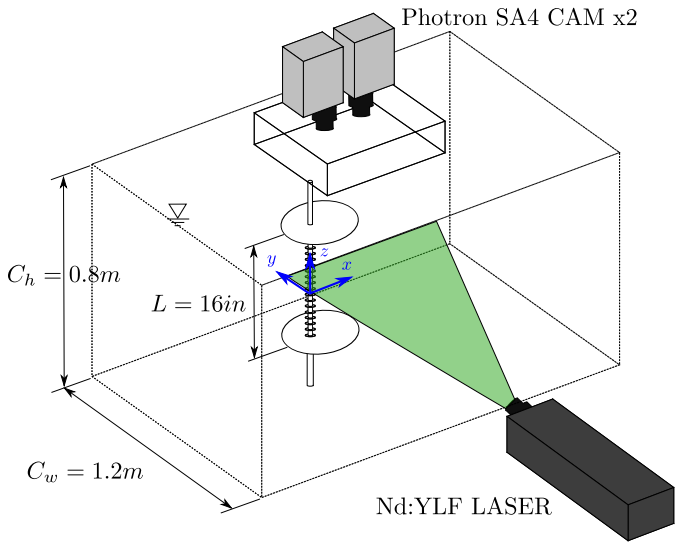

Figure 3.4: Experimental configuration for horizontal plane $(x - y)$ PIV measurements. Illustration for $z/D = 0$.

Photron cameras were mounted above the free surface of the flume in streamwise alignment, extending the field of view to cover the wake region of interest. A plexiglass box cut the free surface of the water in order to eliminate optical distortions created by surface waves. The Photron cameras were set to an acquisition rate of $f_{acq} = 100Hz$, which was over 50 times the highest detected vortex shedding frequency from the experimental models. The laser was pulsed in sync with the camera acquisition, and the beam was conditioned with lens optics to produce a two-dimensional plane sheet approximately $2mm$ thick. The flow is seeded with $10\mu m$ diameter, nearly mutually buoyant hollow glass spheres with specific gravities (SG) of approximately 1.05. For each finned cylinder model, horizontal planar measurements $(x-y$ planes) were obtained at the mid-span $(z = 0)$, intersecting the center of a fin on the finned cylinder models, and at the mid-pitch plane $(z = c/2D)$. For the

uniform cylinders, a single plane is measured at the mid-span ($z = 0$) of the model. The laser and optics are placed on a vertical traverse which is operated by a stepper motor in order to precisely control the vertical location of the measurement plane.

In order to obtain vertical plane measurements ($x-z$ planes), the two Photron cameras are placed on the vertical traverse to the side of the flume in streamwise succession (Figure 3.5a). The Nd:YLF laser is placed outside of the flume, and a vertically aligned laser sheet is generated through a series of mirrors and optics mounted above the free surface of the water flume, as shown in Figure 3.5b. The laser sheet is aligned and positioned by the traversing of the mirrors and optics. Measurements are obtained in vertical planes at the wake centre ($y = 0$) and a plane offset transversely by half the effective diameter for each model ($y = 0.5D_{eff}$). The cameras were positioned the same distance from the measurement plane as in the horizontal plane measurements, such that the spatial resolution and field of view of the wake measurements was matched.

In both horizontal and vertical configurations, the high speed cameras were offset from each other in the streamwise direction such that their image planes overlapped by approximately 10%. Figure 3.6 shows a representative sketch of the imaged region in the wake for the horizontal plane measurements. The transverse extent of the Field of View (FOV) was approximately $X_{fov} = 0.2m$ and each camera had a streamwise FOV of approximately $X_{fov} = 0.2m$. Once the respective vector fields were calculated from the PIV cross-correlations, ten simultaneous vector fields from the two cameras were correlated, and the maximal peak in the correlation matrix determined the precise offset position ($X_{fov} - X_{bl}$, Figure 3.6) of the second camera. In the overlap region, the vector fields are stitched together using a linear weighting function, creating a single vector field covering

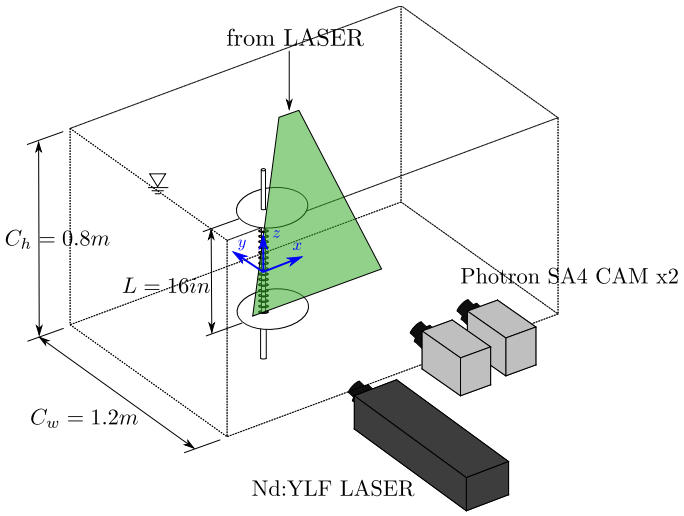

(a) Vertical plane $(x - z)$ PIV measurement general configuration.

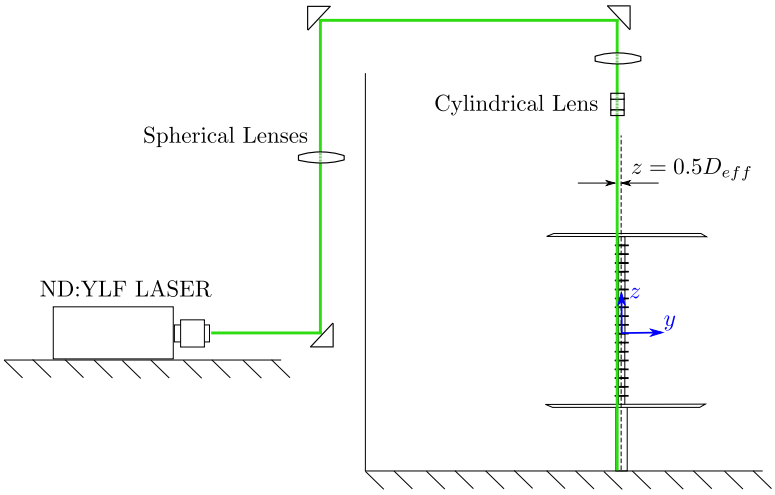

(b) Vertical laser sheet optics illustrated for $y/D_{eff} = 0.5$.

Figure 3.5: Experimental configuration for vertical plane $(x - z)$ PIV measurements.

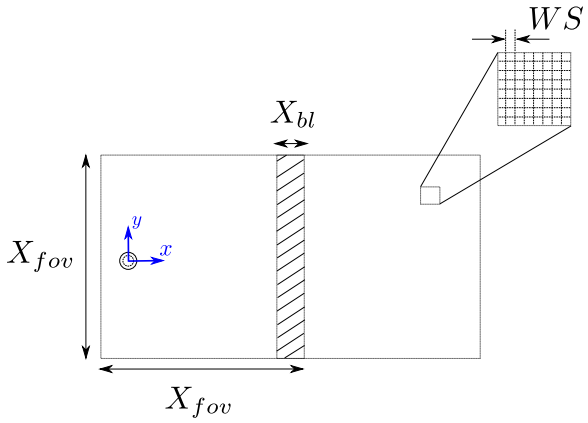

Figure 3.6: Imaged region of the wake for horizontal plane PIV measurements, with dimensions of each square imaged region X_{fov} and hatched overlapped region X_{bl}, subdivided into interrogation windows of WS for PIV correlation.

a field of view of approximately $0.2 \times 0.38m$ $(5.25D_f \times 10D_f)$.

Cross-correlations were performed on sequential image pairs, with a sliding sum of correlation [103] applied over a kernal of four images, in order to reduce random error in the velocity field measurements. The cross-correlations use an iterative, multi-grid algorithm, with the final interrogation window size (WS) of 16×16 pixels. The aperture of the camera was set to an $F_{stop} = 5.6$, resulting in $2 - 3px$ diameter seeding particles in the captured images. The seeding density is such that the amount of particles within each interrogation window is maximized, without particles overlapping ($6 - 8$ particles per window). The interrogation windows are overlapped by 75%, yielding a minimum of $0.02D_f$ vector pitch in the vector field measurements. The velocity error in the PIV measurements is calculated in Appendix B, and is determined to be approximately $1.03 - 2.36\%$ of the free-stream velocity.

3.3 Laser Doppler Velocimetry (LDV) Measurements

In order to measure vortex shedding frequencies (f_S), as well as resolve the spectral content of the velocity fluctuations in the wake, wake velocity data were collected using Laser Doppler Velocimetry (LDV) measurements. The operating principles of LDV are covered in detail by Tavoularis [104]. The miniLDV system employed in the current study comprises of a $140mW$ Argon-Ion laser which produces a dual beam of $628nm$ wavelength intersecting at a focal length of $400mm$ in air ($\approx 530mm$ in water). The intersection of the beams forms a laser volume of $0.15mm \times 1.24mm \times 0.15mm$ in the x, y, and z directions, respectively (Figure 3.7). One beam is frequency shifted using a Bragg cell, and the doppler burst is detected by the system in order to measure one-component of velocity. The beams were aligned such that the streamwise velocity component (u) is measured in the wake region. The flow was seeded with the same neutrally buoyant glass spheres with mean diameter $10\mu m$ and $SG \approx 1.05$ used in the PIV measurements.

The laser volume was aligned using the Photron SA4 high-speed cameras calibrated for PIV measurements. The traces of the two laser beams and their intersection were captured by digital images and the location of the measurement volume was determined using a square grid superposed onto the captured images. The measurement volume position in the wake was set to $x/D_{eff} = 0.5$ and $y/D_{eff} = 5.0$ for each model (Figure 3.7). The velocity data were sampled over 60 minutes, with mean data rates over $40Hz$ resulting in over 2^{17} samples. The data were resampled at a fixed frequency ($f_{acq} = 20Hz$) using the sample-and-hold technique proposed by Adrian and Yao [105]. The resampled velocity signal was partitioned into segments of 2048 samples with 50% overlap between

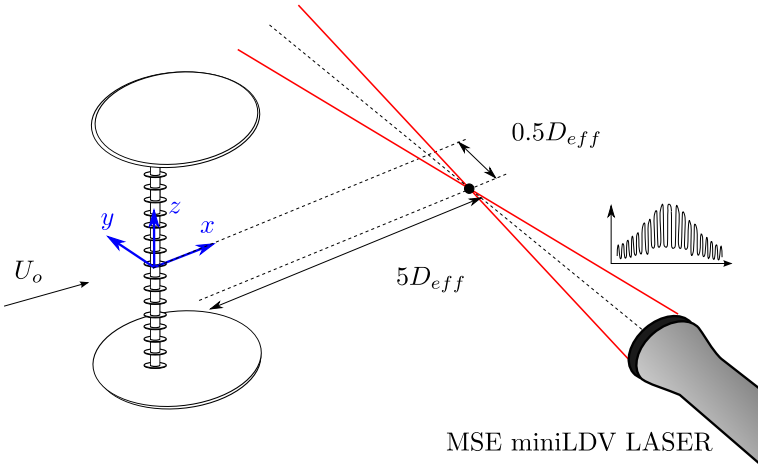

Figure 3.7: LDV measurement experimental configuration. Probe location at $y/D_{eff} = 0$ and $x/D_{eff} = 5$.

each segment. The fast fourier transform (FFT) algorithm was applied to each segment and the resulting spectra were then averaged a minimum of 50 times, yielding a spectral resolution of $\pm 0.002 St_D$. Solid blockage of the models in the test section was between 1.5% and 3%, hence, no corrections were applied to the shedding frequency based on blockage effects unless otherwise specified in the text. Appendix B calculates the bias error in the LDV velocity measurements to be between $0 - 8.4\%$ the free-stream velocity. However, this error does not affect the frequency content of the velocity signal. The errors in the frequency determination are set by the resolution of the obtained velocity spectra, which is $\pm 0.001 fD/U_o$.

3.4 Force Balance Measurements

The aerodynamic forces acting on the models in both the drag and lift directions were measured simultaneously using a strain gauge force balance designed and manufactured at the University of Waterloo (Figure 3.8). The operating principle involves the measurement of strain on milled sections of a cantilevered cylinder using 8 high-resistance (350Ω) precision strain gauges from Vishay Measurement Group with a strain gauge factor (GF) of 2.05. Figure 3.8 shows the strain gauge configuration. Two cross-sections of the cantilevered cylinder were milled out to a flat thickness of $0.08in$, with one section normal to the lift direction and the other normal to the drag direction. Two strain gauges are then adhered to each side of the flat surface with a polymer compound supplied by the manufacturer, and covered with heat shrink in order to allow the gauges to be submersible. The four strain gauges corresponding to each direction are wired in a wheatstone bridge configuration (Figure 3.8) in order mitigate temperature drift and lead resistance effects, as well as to maximize the output signal. The strain gauges were supplied with a $10VDC$ excitation voltage, and the signal output from the wheatstone bridges was amplified using two Futek CSG110 amplifiers at a gain of $0.5mV/V$. The sensitivity of the force balance was approximately $0.125V/g$, though it varied between experimental models and was calibrated independently for each model. The signal was sampled using a National Instruments (NI) model 6320 Data Acquisition System (DAQ) with the voltage input range of $\pm 10V$. The absolute accuracy of the DAQ was $1.14mV$ at this voltage input range with a sensitivity of $0.67mV$. The force balance was calibrated using a set of $1-10g$ calibration weights, applied to the mid-span of the experimental models using a string and pulley system. Added

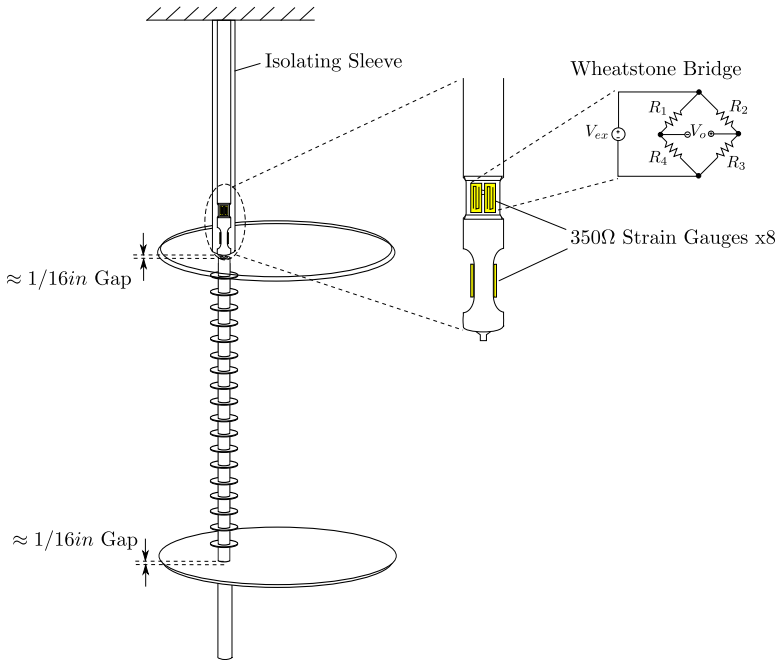

Figure 3.8: Strain gauge force balance for measurement of simultaneous lift and drag.

details on the calibration method are included in Appendix C.

Chapter 4

Results

This chapter presents the results of the experiments described in Chapter 3; namely, time-resolved planar PIV velocity measurements in horizontal and vertical planes in the wake, LDV streamwise wake velocity measurements, and mean drag and fluctuating lift force measurements. The data set obtained from these measurements is used to form a comprehensive description of the salient features of the wake flow development and structural loading. To facilitate this discussion, the chapter is divided into five sections: (i) an overview of the flow development, (ii) the time-averaged flow fields, (iii) characteristics of vortex shedding, (iv) considerations on scaling laws for the wake vortex shedding frequency, and (v) structural loading characteristics.

4.1 Overview of the flow development

Across a large class of bluff-bodies in cross-flow, the wake flow development is dominated by the vortex shedding phenomena [4, 75, 84]. Likewise, previous investigations on finned cylinders support the occurrence of vortex shedding in the wake based on various measurement techniques [17, 18, 24, 26–30]. For the current study, instantaneous snapshots of the spanwise vorticity derived from PIV measurements in a horizontal $(x - y)$ plane, at the mid-pitch position $(z = c/2)$, are presented in Figure 4.1 and clearly exhibit the von Kármán vortex shedding occurring in the wakes of both the finned and uniform cylinders, for $Re_{Deff} = 1020 - 2040$. There are variations in the cycle to cycle characteristics of the wake vortices [53, 54], however the snapshots presented are representative of typical vortex development in the wake of each model. Inspection of the instantaneous vorticity fields shows the roll-up of the separated shear layers into the near wake, and the production of alternating wake vortices. The spanwise wake vortices are the dominant coherent structures in the wake, however, within the vortex formation region and in the wake, smaller scale vortex structures are present. The smaller structures are representative of the shear layer transition regime for the Reynolds number range studied, in which many fine-scale three-dimensional vortex structures develop [5, 43].

General trends in the vortex development can be immediately identified from the instantaneous vorticity fields. Specifically, the scales of vortex formation are similar for a uniform cylinder of base diameter (D) and high pitch ratio ($c/D = 1.0$ and 0.33) finned cylinders (Figures 4.1a-4.1c). In comparison, the vortex formation region is significantly enlarged for the lowest pitch ratio ($c/D = 0.083$) finned cylinder (Figure 4.1d) and a uni-

form cylinder of fin diameter (D_f) (Figure 4.1e). The changes in the wake development with c/D will be outlined in more detail in the following sections.

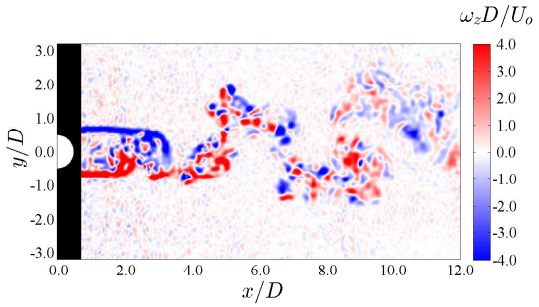

(a) Instantaneous

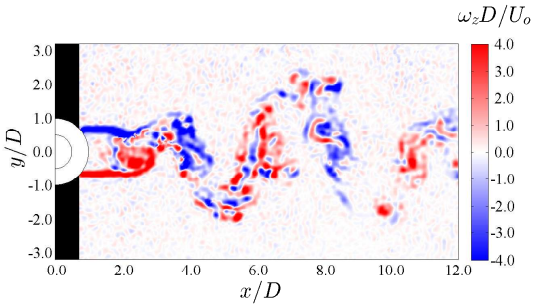

(b) Instantaneous $z/c = 0.5$

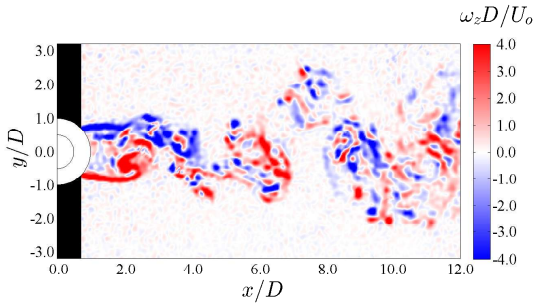

(c) Instantaneous $z/c = 0.5$

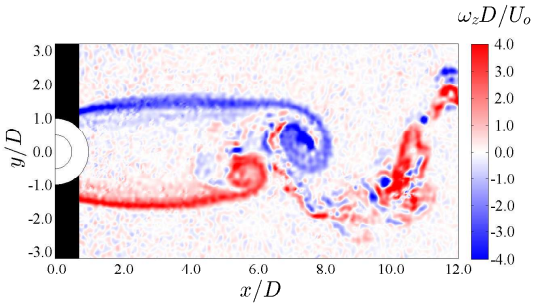

(d) Instantaneous $z/c = 0.5$

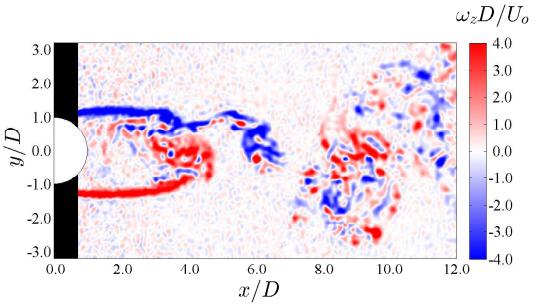

(e) Instantaneous

Figure 4.1: Instantaneous vorticity fields in the wake for (a) uniform cylinder (D), (b) finned cylinder ($c/D = 1.0$), (c) finned cylinder ($c/D = 0.33$), (d) finned cylinder ($c/D = 0.083$), and (e) uniform cylinder (D_f).

4.2 Time-averaged velocity field

From the previously presented instantaneous fields, changes in the scales of vortex shedding in the wake are identified. The discussion in this section aims to present the trends relating to these scales, as well as provide a physical explanation for the trends through an analysis of time-averaged statistics in the wake. Figure 4.2 presents the mean streamwise velocity contours overlaid with the mean streamlines from the horizontal plane PIV measurements, Figure 4.3 presents the mean streamwise velocity contours from the vertical plane PIV measurements, and Figures 4.4, 4.5, and 4.6 present the Reynolds stresses in horizontal planes in the wake ($\overline{u'^2}$, $\overline{v'^2}$, and $\overline{u'v'}$, respectively).

4.2.1 Scales of vortex formation

The mean streamline curvature and position of the saddle point in the wake (Figure 4.2) are associated with the presence and extent of the recirculation region created with the formation of the wake vortices from the models [11, 106]. The figures indicate substantial changes in this recirculation region with fin pitch ratio (c/D). Specifically, for larger pitch ratios of $c/D = 1.0$ and 0.33 (Figures 4.2c-4.2f) the effect of the fins on the mean flow development compared to a uniform cylinder of diameter D (Figure 4.2a) is minimal, with similar recirculation region scales and streamline topology observed. However, for $c/D = 0.33$, the saddle point moves upstream compared to its position for a finned cylinder of $c/D = 1.0$ and a uniform cylinder of diameter D. A large growth in the recirculation region is observed in the wake of a finned cylinder with $c/D = 0.083$ (Figures 4.2g and 4.2h), with the low velocity stagnant flow region extending to the width of the fin diameter and

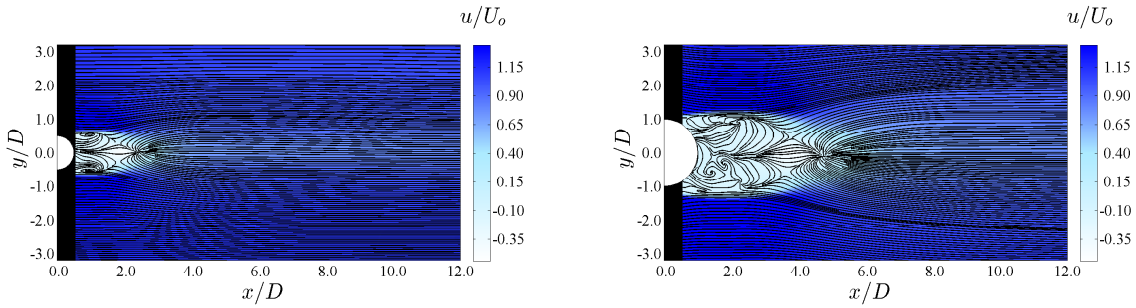

(a)

(b)

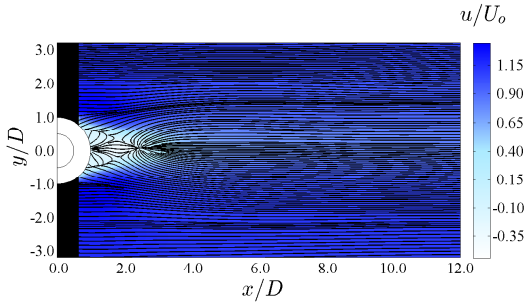

(c) $z/c = 0$

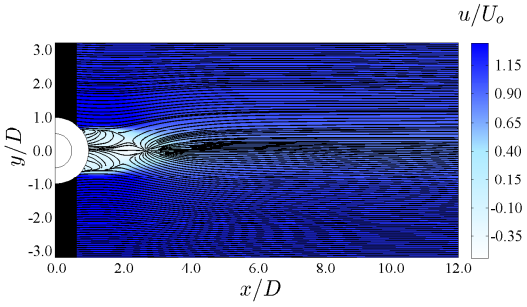

(d) $z/c = 0.5$

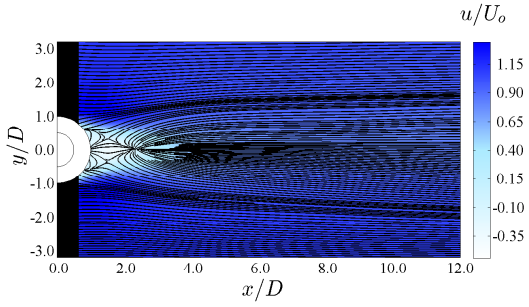

(e) $z/c = 0$

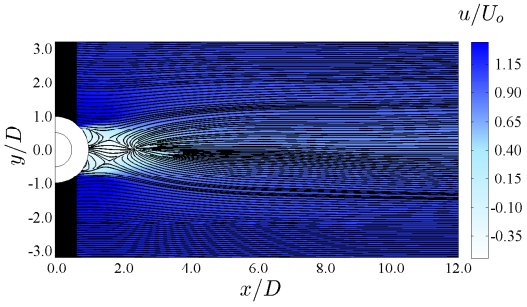

(f) $z/c = 0.5$

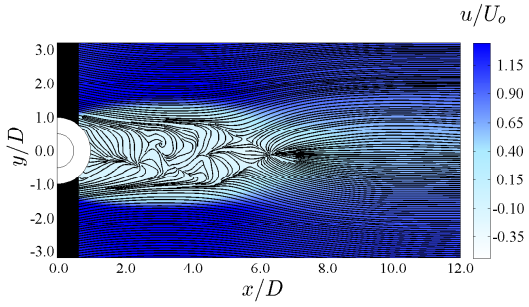

(g) $z/c = 0$

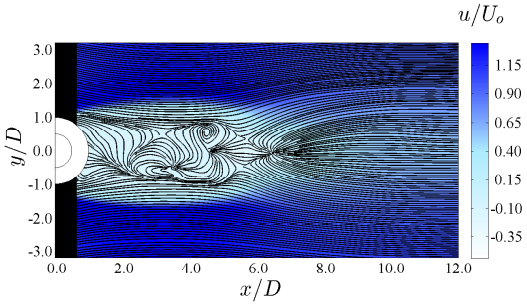

(h) $z/c = 0.5$

Figure 4.2: Mean streamwise velocity contours, overlaid by the mean horizontal planar streamlines for (a) uniform cylinder (D), (b) uniform cylinder (D_f), (c-d) finned cylinder ($c/D = 1.0$), (e-f) finned cylinder ($c/D = 0.33$), and (g-h) finned cylinder ($c/D = 0.083$).

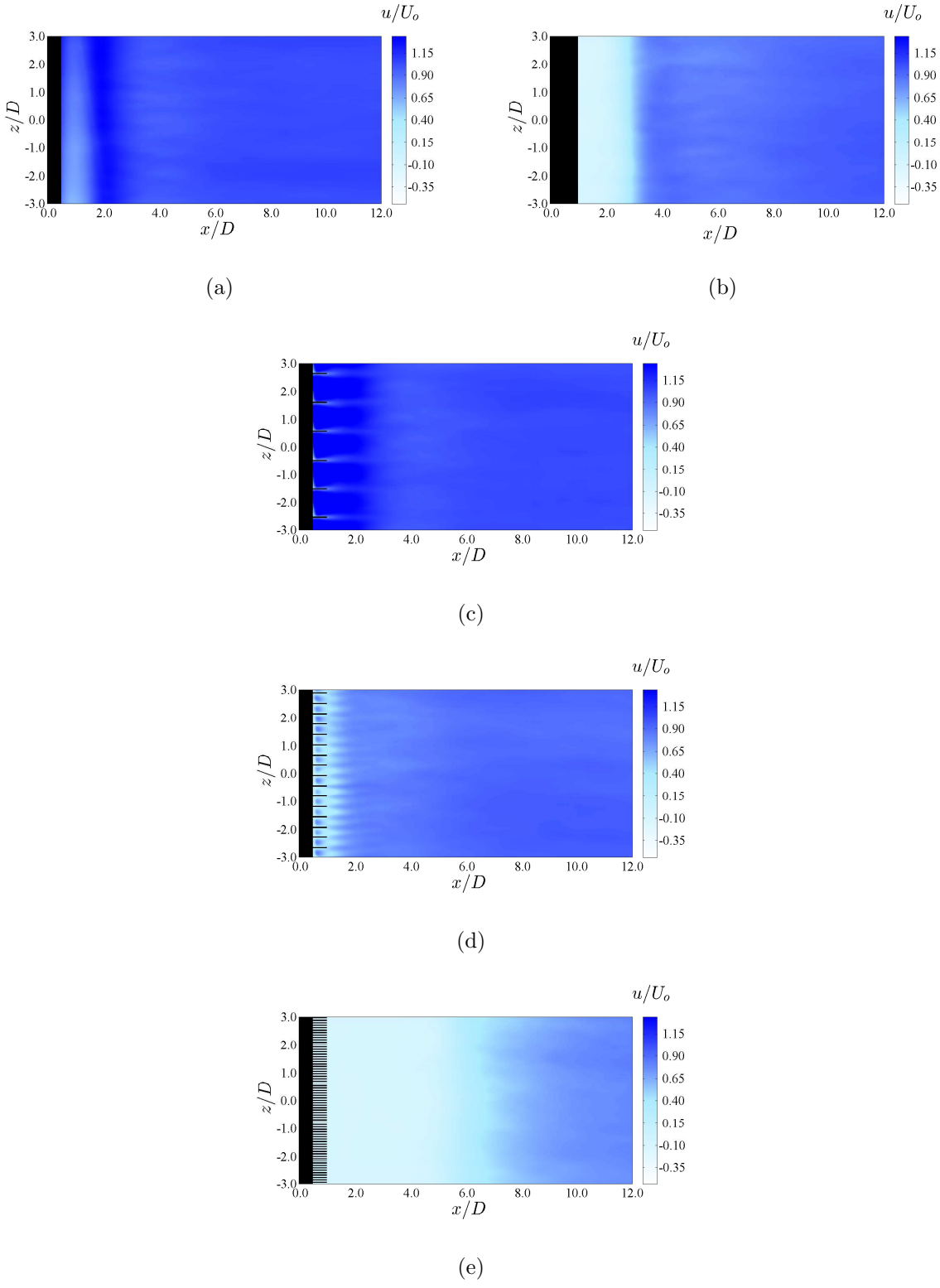

Figure 4.3: Mean streamwise velocity contours in vertical planes at $y/D_{eff} = 0.5$ for (a) uniform cylinder (D), (b) uniform cylinder (D_f), (c) finned cylinder ($c/D = 1.0$), (d) finned cylinder ($c/D = 0.33$), and (e) finned cylinder ($c/D = 0.083$).

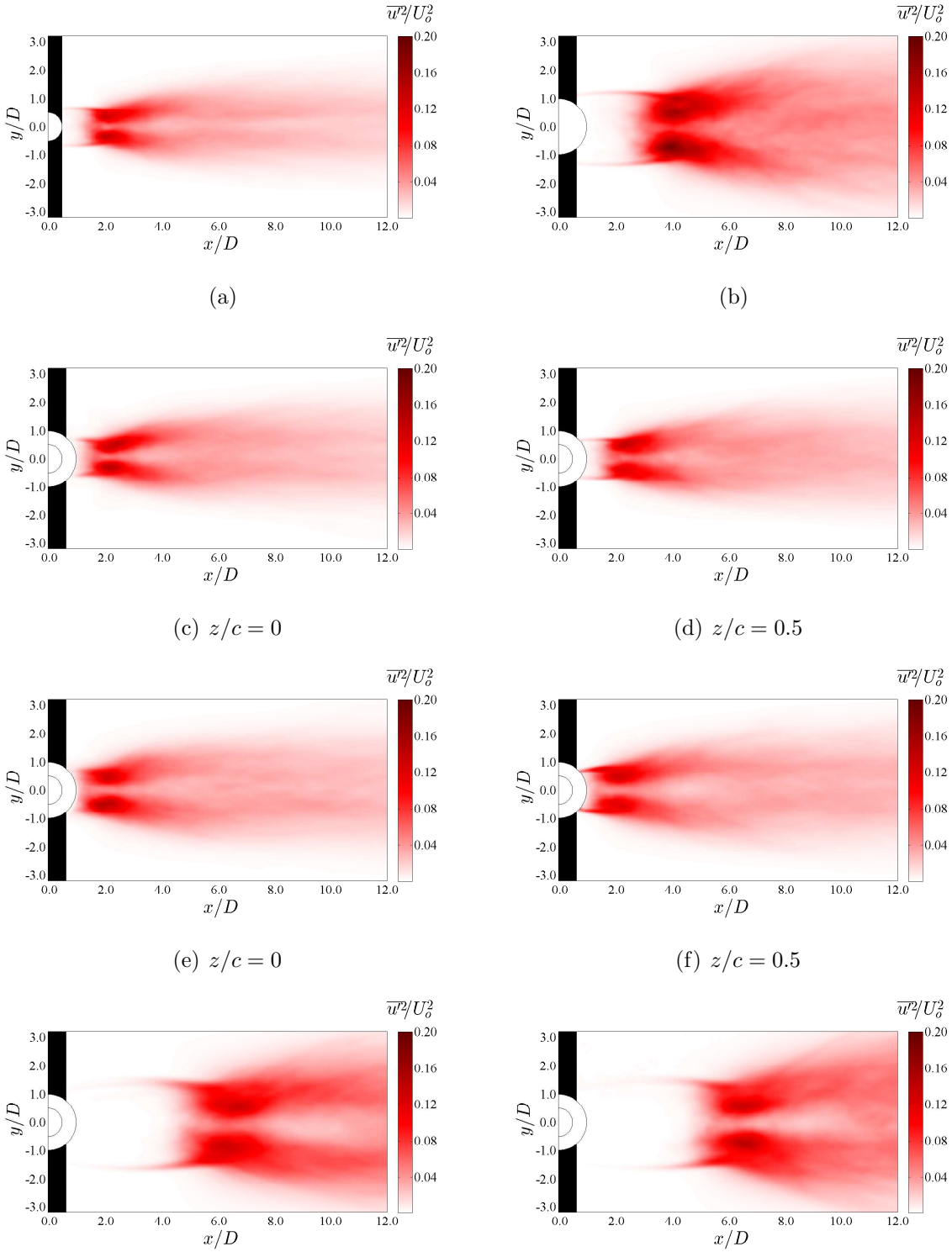

(a) (b)

(c) $z/c = 0$ (d) $z/c = 0.5$

(e) $z/c = 0$ (f) $z/c = 0.5$

(g) $z/c = 0$ (h) $z/c = 0.5$

Figure 4.4: Streamwise Reynolds stress ($\overline{u'^2}$) for (a) uniform cylinder (D), (b) uniform cylinder (D_f), (c-d) finned cylinder ($c/D = 1.0$), (e-f) finned cylinder ($c/D = 0.33$), and (g-h) finned cylinder ($c/D = 0.083$).

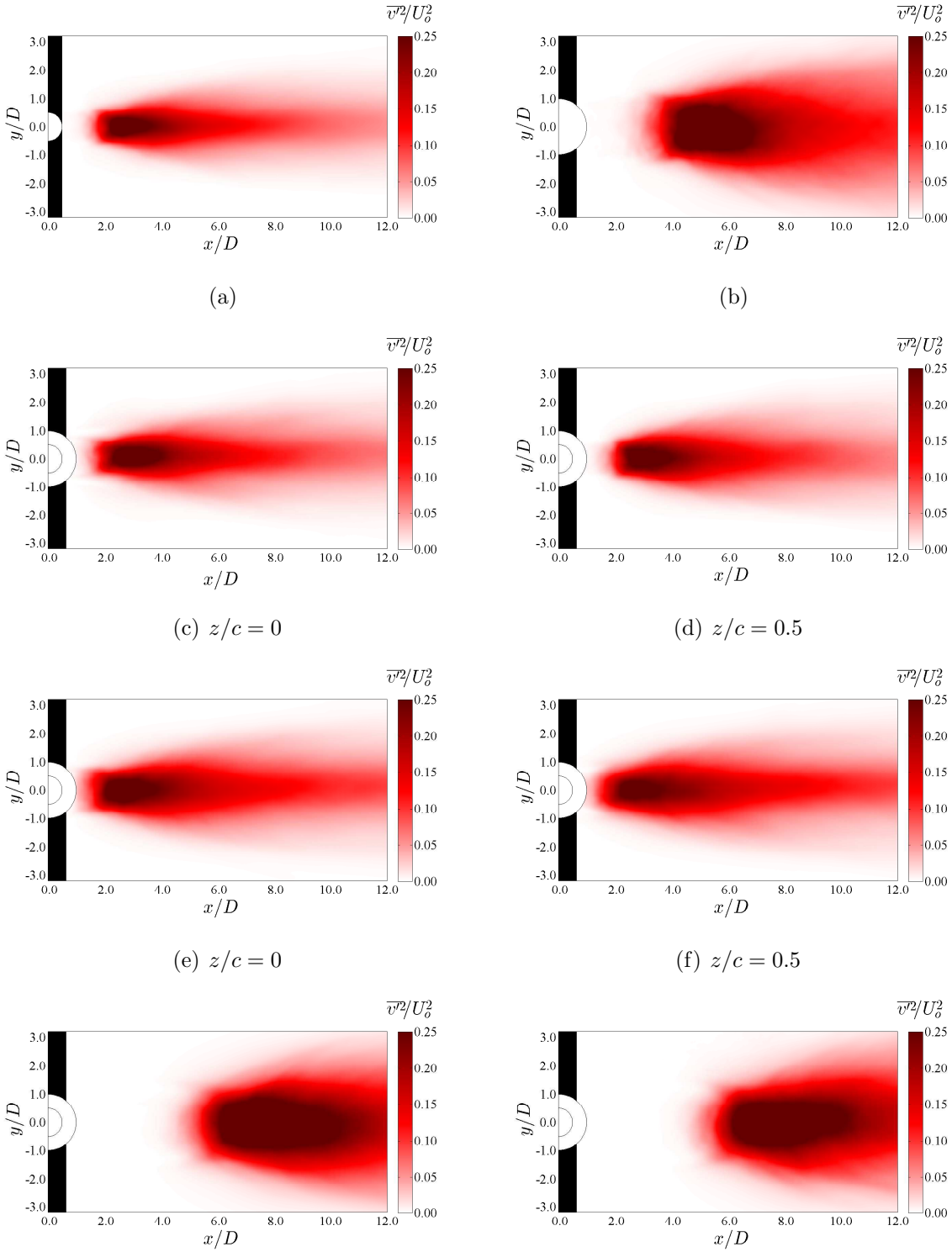

(a) (b)

(c) $z/c = 0$ (d) $z/c = 0.5$

(e) $z/c = 0$ (f) $z/c = 0.5$

(g) $z/c = 0$ (h) $z/c = 0.5$

Figure 4.5: Transverse Reynolds stress ($\overline{v'^2}$) contours in the wake for (a) uniform cylinder (D), (b) uniform cylinder (D_f), (c-d) finned cylinder ($c/D = 1.0$), (e-f) finned cylinder ($c/D = 0.33$), and (g-h) finned cylinder ($c/D = 0.083$).

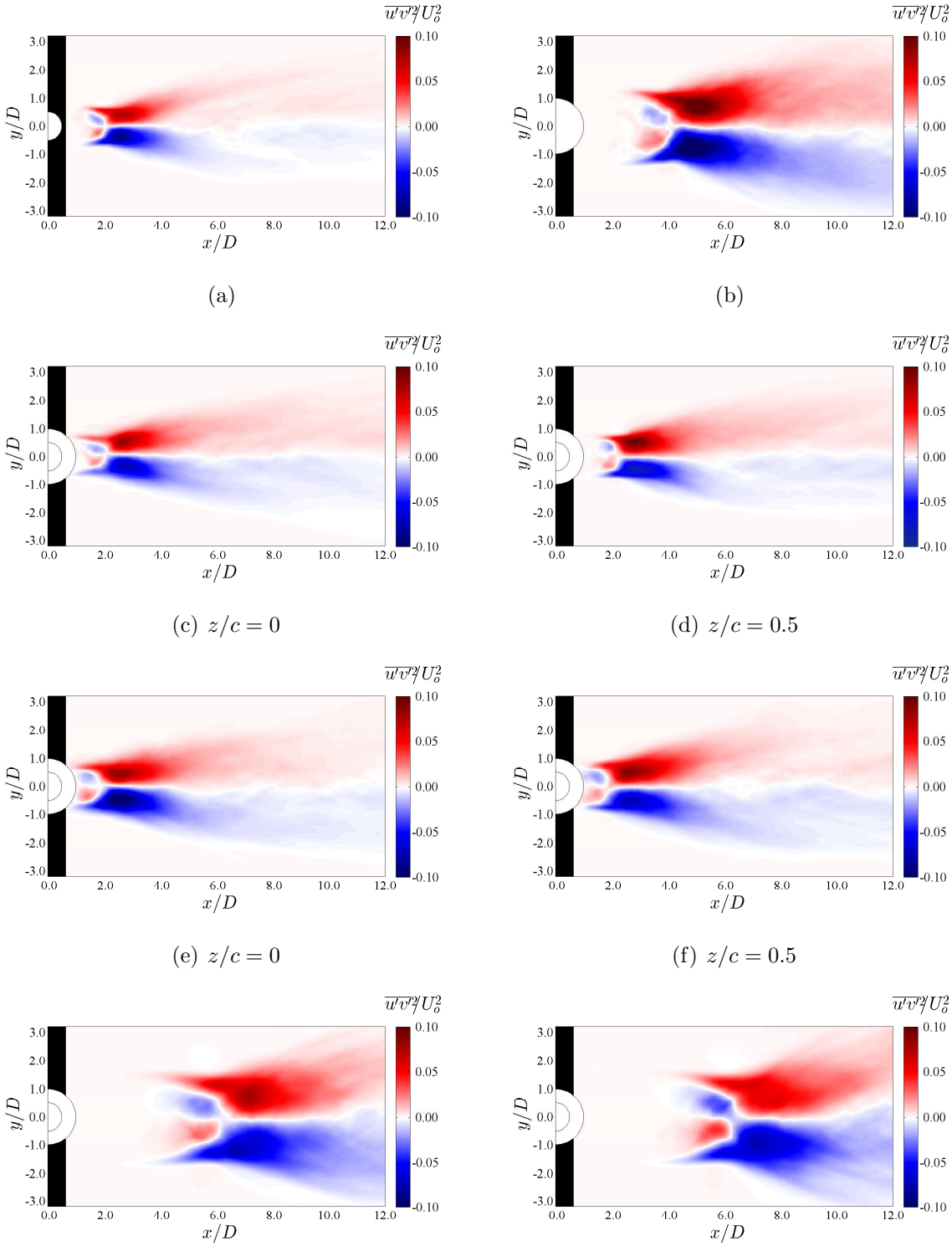

(a) (b)

(c) $z/c = 0$ (d) $z/c = 0.5$

(e) $z/c = 0$ (f) $z/c = 0.5$

(g) $z/c = 0$ (h) $z/c = 0.5$

Figure 4.6: Cross-term Reynolds stress ($\overline{u'v'}$) contours in the wake for (a) uniform cylinder (D), (b) uniform cylinder (D_f), (c-d) finned cylinder ($c/D = 1.0$), (e-f) finned cylinder ($c/D = 0.33$), and (g-h) finned cylinder ($c/D = 0.083$).

extending into the wake to $x/D \approx 6$. The recirculation region for $c/D = 0.083$ extends further into the wake than for a uniform cylinder of D_f (Figure 4.2b), while retaining similar transverse scales. This large stagnant flow region in the near wake and associated downstream displacement of vortex formation was also observed by Hamakawa et al. [18] for helically finned cylinders with low pitch ratios ($c/D \leq 0.16$) and in several investigations on flows around cylinders with porous shells [30, 78–80].

The scales of vortex formation can be quantitatively described by invoking definitions of the vortex formation length and wake width [5]. The vortex formation length (L_f) is defined as the streamwise distance along the wake centreline to the peak in the RMS of the streamwise velocity fluctuations ($u'(x, 0, 0)$). The wake width (L_w) is defined as the transverse distance between the two distinct peaks in the RMS of the streamwise velocity fluctuations ($u'(L_f, y, 0)$) at a streamwise location of $x = L_f$. Figure 4.7 presents the variation of the two vortex formation region characteristic scales with pitch ratio. Non-monotonic trends in both L_f and L_w may be identified with c/D. Figure 4.7 shows that with the addition of fins, for $c/D = 1.0$, there is slight enlargement of the formation length compared to a uniform base cylinder, with approximately equal wake width. At this pitch ratio, formation length differs by $0.2D$ between planar measurements in-line with the fin (Figure 4.2c) and at the mid-pitch plane (Figure 4.2d), indicating marginal spanwise differences in the vortex development at this pitch ratio. For a pitch ratio of $c/D = 0.33$, there is again a minor increase in the characteristic dimensions of vortex formation (Figure 4.7). Following that, for the smallest pitch ratio of $c/D = 0.083$, there is a substantial enlargement of the formation region (Figures 4.2g, 4.2h and 4.7). The formation length is approximately 50% larger than that of uniform cylinder of diameter D_f, and the wake

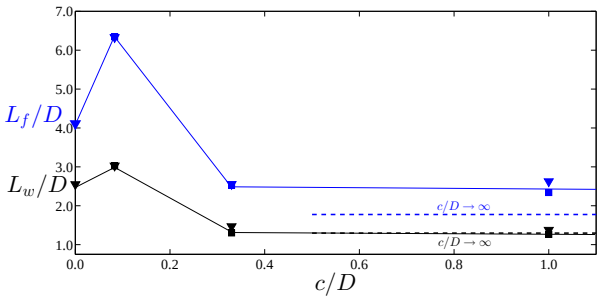

Figure 4.7: Formation length (L_f) and wake width (L_w) of the formation region versus fin pitch ratio (c/D) for (■) measurements at the mid-pitch location $z/c = 0.5$, and (▼) measurements in-line with the fins ($z/c = 0$).

width is also enlarged, but to a lesser degree. Measurements parallel to the fins and at the mid-pitch plane show similar estimates of the formation length and wake width for pitch ratios $c/D = 0.33$ and $c/D = 0.083$, indicating no spanwise variation in vortex formation characteristics for the lower pitch ratios.

It is pertinent to the analysis at this point to discuss some inferred asymptotic characteristics of the flow development. Specifically, as the limit $c/D \to 0$ is approached, the fins would become so close together that flow between the fins is impeded and the finned cylinder would act as a solid uniform cylinder of diameter D_f. As the limit $c/D \to \infty$ is approached, the fins would be so spaced apart that the flow development matches that about a uniform cylinder of diameter D, similar to the observed behaviour in studies on uniform cylinders with end plates with increasing model aspect ratio [41, 72, 73]. Hence, despite any trends between these limits, it is expected that wake characteristics of finned cylinders asymptotically approach that of the respective uniform cylinder at sufficiently high or low c/D. Given the trends discussed referring to Figure 4.7, the asymptotic behaviour of the vortex formation scales is well established for $c/D \to \infty$, with gradual

reduction of the characteristic scales observed as c/D increases for $c/D \geq 0.33$. In contrast, towards $c/D \to 0$, the asymptotic behaviour isn't fully established in the presented results due to a non-monotonic trend developing for low c/D. However, it is expected that measurements at lower $c/D = 0.083$ would show a gradual reduction in the characteristic scales approaching the values for $c/D = 0$.

The unsteady flow in the wake is dominated by the fluctuations associated with the vortex shedding phenomena. This gives rise to Reynolds stresses in the wake ($\overline{u'^2}$, $\overline{v'^2}$, and $\overline{u'v'}$), which are presented in Figures 4.4, 4.5, and 4.6. The wake Reynolds stresses exhibit a high degree of similarity between all the models investigated, scaling generally with the reported changes in the vortex formation and wake widths. The magnitude of the Reynolds stresses in the wake are comparable for $c/D = 1.0$ and a uniform base cylinder. For $c/D = 0.33$, the Reynolds stresses are similar in magnitudes in the wake, however higher Reynolds stresses are present near the the surface of the cylinder. In addition, high $\overline{u'^2}$ is observed in the separated shear layer, indicating some unsteady flapping of the separated shear layers for $c/D = 0.33$. For $c/D = 0.083$ (Figures 4.4g, 4.4g, 4.5g, 4.5g, 4.6g, and 4.6g), compared to a uniform cylinder of fin diameter (Figures 4.4b, 4.5b, and 4.6b), the peak Reynolds stresses are decreased.

From the vertical plane PIV measurements and horizontal plane PIV measurements at $z/c = 0.5$ and $z/c = 0$, aspects of the spanwise development of the vortices can be ascertained. For $c/D = 0.083$, the horizontal plane mean fields in-line with the fin and at the mid-pitch location are nearly identical (c.f. 4.2g and 4.2h) and in the vertical plane measurements (Figure 4.3e), the velocity streaks are not observed. For $c/D = 1.0$ and $c/D = 0.33$, differences in the mean flow development between planes taken in-line with a

fin at $z/c = 0$ (Figures 4.2c and 4.2e) and those taken parallel to the mid-pitch location at $z/c = 0.5$ (Figures 4.2d and 4.2f) develop due to a low velocity region surrounding the fin, a product of the boundary layers developing on the fin surfaces. These low velocity streaks can also be seen clearly in the vertical plane PIV measurements (Figures 4.3c and 4.3d) directly downstream of each fin, a consequence of the low-momentum fluid in the boundary layers forming on the fin surfaces. However, besides an affected region near the fins, there does not appear to be any substantial differences in the mean flow development between the two measured horizontal planes obtained at the mid-pitch ($z = c/2$) and in-line with a fin ($z = 0$) in respect to the topology and size of the recirculation region (Figure 4.2) for finned cylinders. This can also be seen in the vertical PIV measurments at $z/D_{eff} = 0.5$ which show that the low velocity perturbations in the wake introduced by the fins do not extend past the formation region of the vortices (Figure 4.3). This indicates that any substantial spanwise spatial modulation of the vortex shedding characteristics does not occur on the scale of the fin pitch, such as the cellular shedding observed by Nakamura and Igarashi [24] for multi-step cylinders and the vortex dislocations observed in the wake by Morton and Yarusevych [48, 49] and McClure et al. [25] for dual step cylinders. Hence, vortex shedding occurs nominally two-dimensionally in the wake in the present study, similar to that observed in the wakes of uniform circular cylinders [5].

4.2.2 Shear layer development

In order to explain the observed changes in the scales of vortex formation with changing c/D, it is of interest to investigate the mean flow separation characteristics and vorticity

development in the wake. Figure 4.8 presents the mean vorticity fields in horizontal planes at the mid-span of uniform cylinders of base (D) and fin (D_f) diameter (Figures 4.8a and 4.8b, respectively), as well as the two horizontal planes at the mid-pitch and in-line with a fin for the finned cylinders (Figures 4.8c-4.8h). The vorticity is estimated from the measured velocity fields using Richardson extrapolation derivative estimators [102], which is known to mitigate the under prediction of vorticity values due to the smoothing effect of the derivative estimators, at the cost of higher noise. At the mid-pitch plane (Figures 4.8d, 4.8f, and 4.8h), the shear layers extend much further into the wake for the $c/D = 0.083$ case, diffuse earlier for the $c/D = 0.33$ case, and are nearly identical to a uniform base cylinder for $c/D = 1.0$. Of note are the changes in the vorticity fields between horizontal planes taken parallel to a fin ($z/c = 0$) and those taken at the mid-pitch location ($z/c = 0.5$) for pitch ratios $c/D = 1.0$ and 0.33. The shear layers extending from the radial cylinder surfaces are more diffuse and weaker (Figures 4.8c and 4.8e) than those observed at the mid-pitch position (Figures 4.8d and 4.8f), due to the surrounding boundary layer flow inducing lower streamwise velocities in the region.

Figure 4.9 plots the shear layer trajectories for the uniform and finned cylinder models based on the mid-pitch ($z/c = 0.5$) planar measurements. The trajectories are determined by tracking the position of maximum vorticity in the traverse profiles in the wake with streamwise distance $\omega_{z,max}(x)$. Extrapolation of the trajectories show that flow separation occurs from the base cylinder for $c/D = 1.0$ and $c/D = 0.33$, and occurs at the fin diameter for $c/D = 0.083$. For $c/D = 0.33$, while flow separates from the base cylinder, the trajectory as it extends into the wake exhibits a higher degree of curvature and is angled more outward compared to the uniform base cylinder and $c/D = 1.0$ trajectories. This

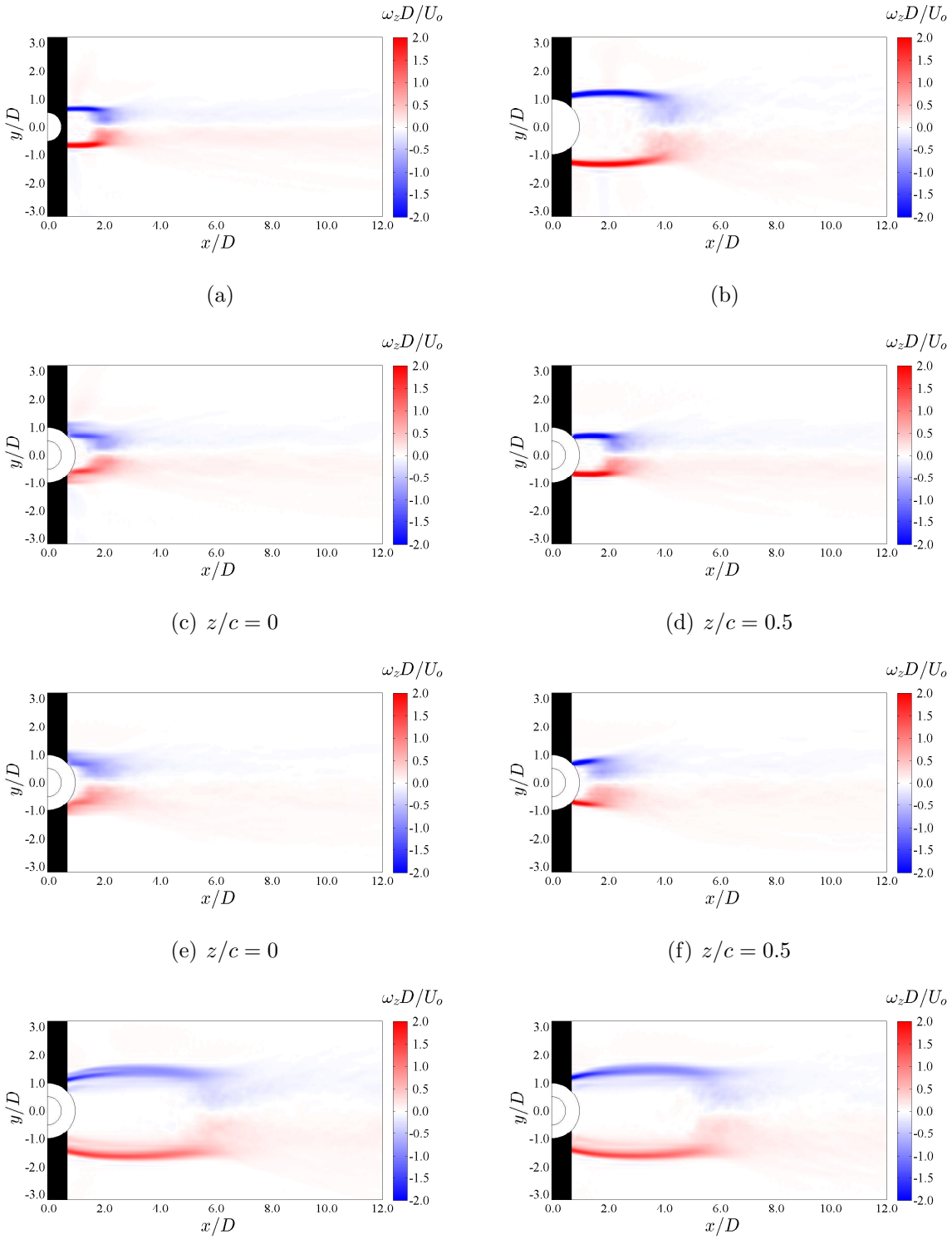

Figure 4.8: Mean spanwise vorticity (ω_z) for (a) uniform cylinder (D), (b) uniform cylinder (D_f), (c-d) finned cylinder ($c/D = 1.0$), (e-f) finned cylinder ($c/D = 0.33$), and (g-h) finned cylinder ($c/D = 0.083$).

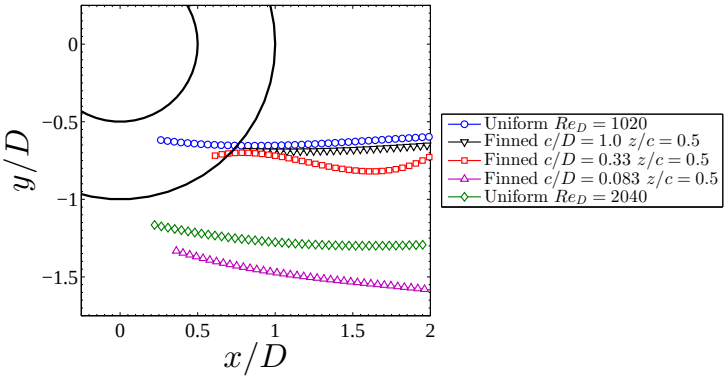

Figure 4.9: Shear layer trajectories computed by tracking the maximum vorticity with streamwise distance $\omega_{z,max}(x)$. The circular contours indicate the positions of the base cylinder and fins.

can be seen in the mean vorticity fields in Figures 4.8e and 4.8f, which show the vorticity development in the wake exhibiting some differing characteristics than for $c/D = 1.0$. Specifically, the mean vorticity fields show the shear layers diffusing earlier into the near wake. This indicates that at a pitch ratio $c/D = 0.33$, the lateral vorticity generated on the fins is beginning to affect the flow development at the mid-pitch location. However, with separation occurring at similar positions from the base cylinder for a uniform base diameter cylinder and for pitch ratios $c/D = 1.0$ and 0.33, there is little change in the size of the vortex formation regions between these models (Figure 4.7). For $c/D = 0.083$, flow separation occurs from the fin diameter and the trajectory is angled outward to a higher degree than for a uniform cylinder of diameter D_f, indicative of earlier flow separation and leading to the enlarged wake width observed for this pitch ratio (Figure 4.7).

The marked change in flow separation and vortex formation scales for low pitch ratios (e.g., $c/D = 0.083$) is speculated to be linked to the development of the lateral boundary

layers on the fin surfaces. As c/D decreases and approaches the scale of the boundary layer thickness, the boundary layers on neighbouring fin surfaces coalesce, reducing the flow velocities and changing the related dynamics in the regions between the fins. The boundary layer thickness on the fin surfaces may be estimated using a Blasius [107] flat plate solution at a streamwise distance of $0.5D_f$ from the leading edge of the fin. Based on estimates for the current experimental set-up, it is expected that the boundary layers on adjacent fin surfaces will coalesce between the fins at approximately $c/D \approx 0.15$. Indeed, for $c/D = 0.083$ in the present results, the fact that the boundary layers have coalesced is supported by the vertical plane measurements presented in Figure 4.3e. The figure shows the absence of low velocity streaks downstream of the fins and a corresponding small streamwise velocity magnitude between the fin pitch ($0 < z/c < 1$). This is in contrast to observations for $c/D = 1.0$ (Figure 4.3c) and $c/D = 0.33$ (Figure 4.3d), which show higher velocities between the fin pitch and independent boundary layer streaks extending from each fin surface. When flow through the pitch of the fins is impeded by the boundary layer coalescence, the separated shear layer develops from the fin diameter (D_f). As shown by Hamakawa et al. [18], once this flow separation behaviour changes, flow field parameters scale approximately with the fin diameter instead of the cylinder effective diameter (D_f as opposed to $D_{eff} = 1.25D$ in this case, for $c/D = 0.083$). Specifically, the bulk of the incoming flow is instead displaced around at the fin diameter (D_f), and the wake width (L_w, Figure 4.7) thus grows transversely.

In order to investigate the characteristics of the shear layers immediately following separation, Figure 4.10 plots the magnitude of the mean streamwise velocity in transverse profiles at $x/D = 0.5$ for a uniform cylinder of base diameter and $x/D_f = 0.5$ for the

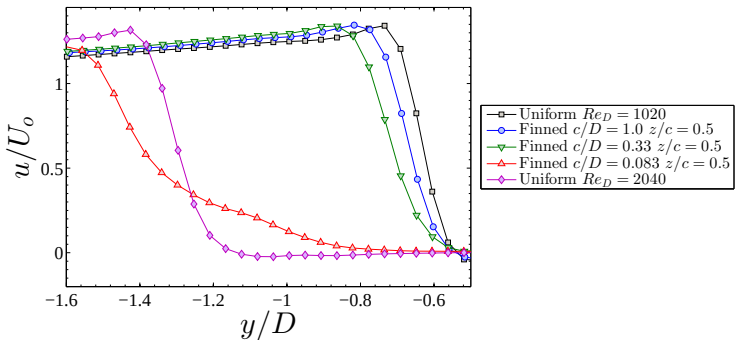

Figure 4.10: Transverse profiles of the streamwise velocity at $x/D = 0.5$ for uniform cylinder of diameter D and $x/D_f = 0.5$ otherwise.

remaining models. The shear layers are displaced transversely with increasing c/D (Figure 4.10), corresponding with the previously discussed increases in wake width (L_w, Figure 4.7) with pitch ratio. Figure 4.11 presents the variation of the shear layer thickness δ_{sl}, derived from these profiles, with pitch ratio c/D. The shear layer thickness is defined as the distance over which the streamwise velocity changes from $5\% - 95\%$ the minimum to maximum streamwise velocity in the profile. Figure 4.11 demonstrates similarities in the shear layer development for the uniform base cylinder and finned cylinder with pitch ratios $c/D = 1.0$ and $c/D = 0.33$, with these models having approximately the same shear layer thickness. For $c/D = 0.083$, the shear layer is much thicker (Figure 4.11), leading to rather weak velocity gradients in the profile. In addition, a slip velocity is present at the edge of the fin diameter (i.e., $u_{slip} > 0$ at $y = -D$) (Figure 4.10).

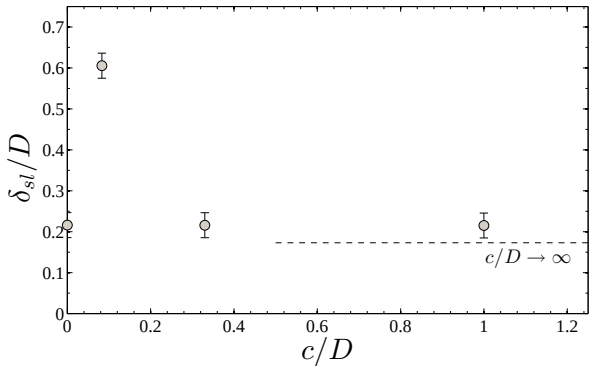

Figure 4.11: Shear layer thickness δ versus fin pitch ratio c/D. The shear layer thickness is evaluated from measuring the distance between 5%-95% the min-max streamwise velocity in the transverse profiles shown in Figure 4.10.

4.3 Vortex Shedding

The previous section outlined mean flow changes with pitch ratio. Specifically, changes in the scales of the recirculation region in the wake and separated shear layer characteristics are identified and linked to the lateral boundary layer development on the finned surfaces. This section aims to provide a description of the unsteady flow development in the wake, dominated by the vortex shedding phenomenon and characteristics of the wake vortex shedding frequency and the development of the vorticity into the wake vortices are outlined.

4.3.1 Wake vortex shedding frequency

Figure 4.12a presents the spectra of the streamwise wake velocity measured by LDV at a position of $x/D_{eff} = 5$ and $y/D_{eff} = 0.5$ in the wake for the uniform cylinders and finned cylinders investigated. The respective spectra are offset from each other by 1.5

orders of magnitude for clarity of presentation. The spectral characteristics show a high degree of similarity between both the uniform cylinders and all the finned cylinder models. A dominant peak at the vortex shedding frequency and a secondary harmonic peak are discernible for all models, indicating that the transient characteristics of von Kármán vortex shedding are not altered significantly by the presence of the fins. Figure 4.12b presents the same spectra, but normalized by the cylinder effective diameter [26]. The dominant spectral peaks at the vortex shedding frequency for the uniform cylinders are nearly coincident using this normalization, as indicated by the dashed vertical line in Figure 4.12b, however the spectral peaks remain lower at lower dimensionless frequencies for the finned cylinder models. Figure 4.13 shows the variation in the frequency energy content with time by presenting the spectrograms of the streamwise velocity signals obtained from the LDV measurements. The spectrograms are computed over 4096 samples at a constant $20Hz$, with 97% overlap to show the temporal evolution of the spectral energy content. The results indicate that the dominant shedding frequency shows some variation in time for all the models. The magnitude of the peak is shown to exhibit higher modulations and fluctuations over a wider band of frequencies for the high pitch ratio ($c/D = 1.0$ and 0.33 in Figures 4.13b and 4.13c) and uniform cylinder of diameter D (Figure 4.13a) models in comparison to the lowest pitch ratio ($c/D = 0.083$ in Figure 4.13d) and uniform cylinder of fin diameter (D_f in Figure 4.13e). This is attributed to aspect ratio effects on the flow development, with cellular and oblique shedding for the higher aspect ratio models leading to frequency variation in time compared to the single cell shedding from the lower aspect ratio models (e.g., $L/D_f = 10.6$ for the uniform fin diameter cylinder) which are nearing transitional aspect ratios reported in studies where the end cells developing near

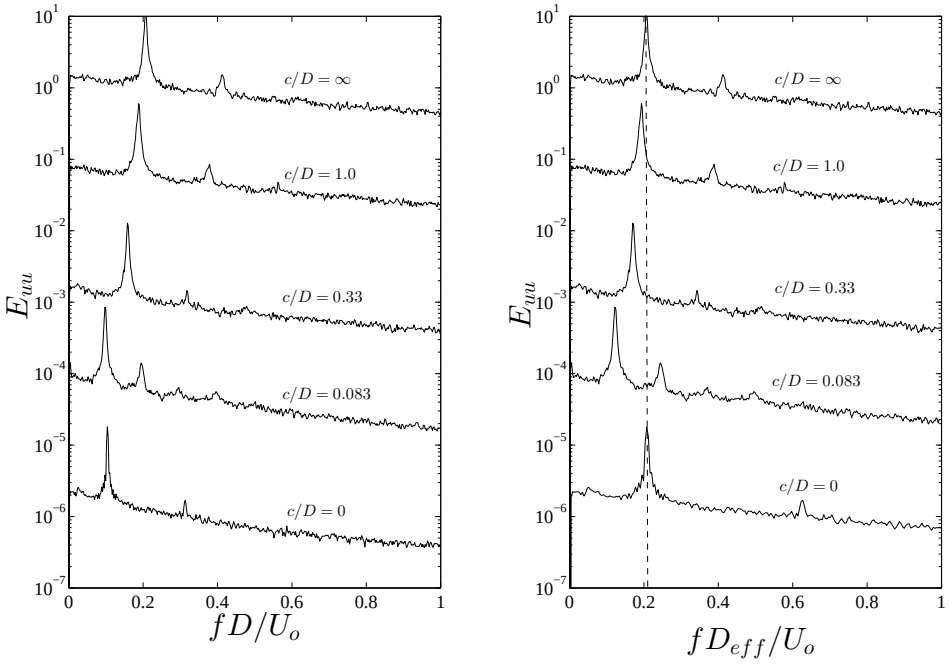

Figure 4.12: Wake velocity spectra of the streamwise velocity component measured at $x/D_{eff} = 5$ and $y/D_{eff} = 0.5$. The frequency is normalized by (a) the base cylinder diameter (D) and (b) the effective diameter (D_{eff}).

the endplate surfaces merge at the midspan [73, 108].

The shedding frequency (f_S) variation with pitch ratio (c/D) is shown in Figure 4.14. As $c/D \to \infty$ (i.e., the geometry approaches that of a uniform base cylinder), the shedding frequency asymptotically approaches that of a uniform cylinder of diameter D. As fins are added, effectively decreasing c/D, the shedding frequency monotonically decreases until the shedding frequency becomes slightly lower than that of a uniform cylinder of fin diameter for $c/D = 0.083$. Following that, the trend implies that the shedding frequency will

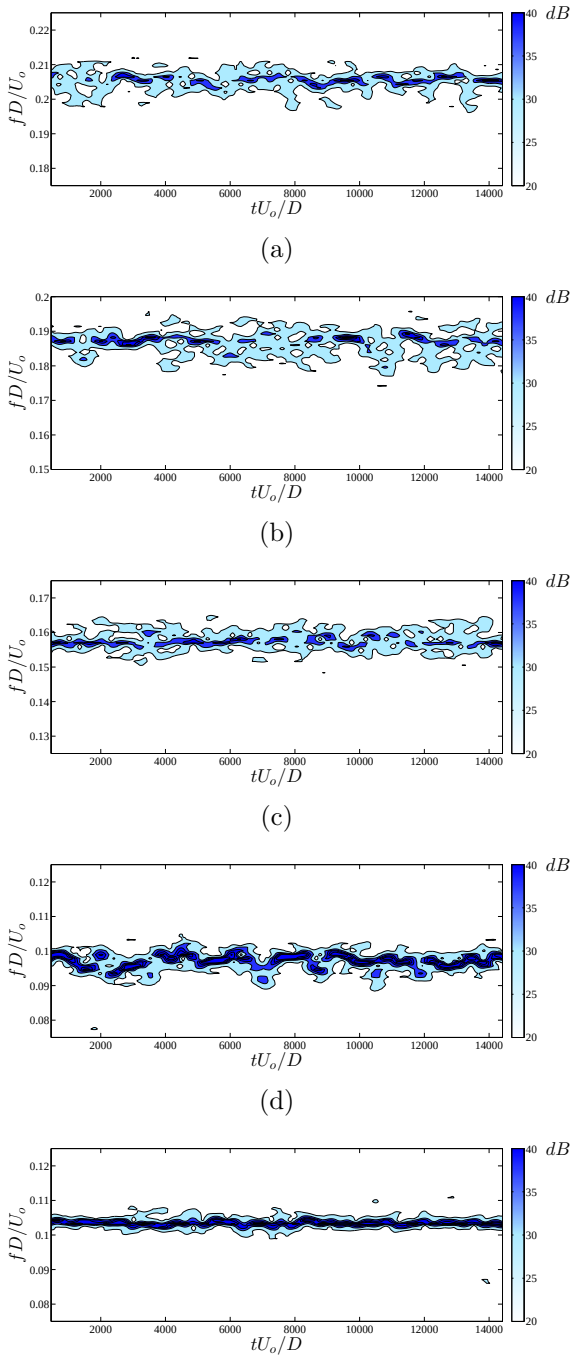

Figure 4.13: Spectrograms showing the frequency content energy variation in time for the streamwise velocity component measured at $x/D_{eff} = 5$ and $y/D_{eff} = 0.5$

increase to asymptotically approach that of the uniform fin diameter cylinder. Comparing the trends in shedding frequency in Figure 4.14 to those identified in the wake widths and formation lengths in Figure 4.7, it can be concluded that the shedding frequency has an inverse relationship with the vortex formation scales, in agreement with previous studies on vortex shedding from bluff-bodies [1, 4].

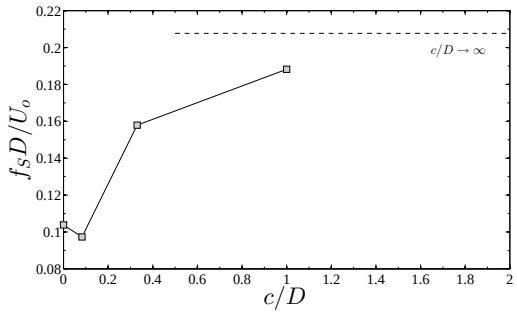

Figure 4.14: Vortex shedding frequency ($f_S D/U_o$) versus fin pitch ratio (c/D).

4.3.2 POD analysis

The horizontal planar measurements are decomposed using Proper Orthogonal Decomposition (POD), an energy-based decomposition of flow field which may be used as a method for detecting coherent structures in turbulent flows [109] and provide a description of the distribution of fluctuating energy in the wake. The decomposition of the zero-mean velocity field (Equation 4.1) results in a set of spatial modes ϕ_i with corresponding temporal coefficients a_i.

$$\vec{u^*}(x, y, t) = \sum_{i=1}^{N} a_i(t)\vec{\phi_i}(x, y) \tag{4.1}$$

Figure 4.15 presents the first two spatial modes and their temporal coefficients for a uniform cylinder of base diameter (Figure 4.15a and 4.15b) and a finned cylinder of pitch ratio $c/D = 0.33$ (Figure 4.15c and 4.15d). The first two modes, when superposed in combination with their respective temporal coefficients, yield a reduced order model of the vortex shedding in the wake [110, 111]. The temporal modes show regular, sinusoidal fluctuations at the vortex shedding frequency for both the uniform (Figure 4.15b) and finned (Figure 4.15d) models, indicative of the nominally two-dimensional vortex shedding occurring in the wakes of the structures. The first two spatial modes for both models have similar topologies, however the lower shedding frequency in the wake of the finned cylinder model and the associated stronger wake vortices [50] leads to larger coherent structures in the wake. In addition, the spatial modes show higher energy content closer to the cylinder surface for $c/D = 0.33$, in agreement with previous discussions on the observed unsteadiness in the shear layers and movement of the streamline saddle point towards the cylinder surface at this pitch ratio.

The energy distribution in the spatial modes resulting from the POD decomposition of the $x - y$ plane velocity fields is presented in Figure 4.16. Figure 4.16a plots the percentage of the total energy in the wake contained in the respective spatial eigenmodes for each model investigated, and Figure 4.16b plots the cumulative energy contained in the first N spatial eigenmodes. For each case, the majority of the energy is in the first two spatial modes ($\approx 55 - 70\%$). For the uniform cylinders, and for $c/D = 1.0$, the cumulative energy in the first two modes is approximately equal to 55%. With decreasing pitch ratio, the proportion of the wake fluctuation energy contained in the first two modes increases to approximately 60% for $c/D = 0.33$ and approximately 70% for $c/D = 0.083$. This indicates

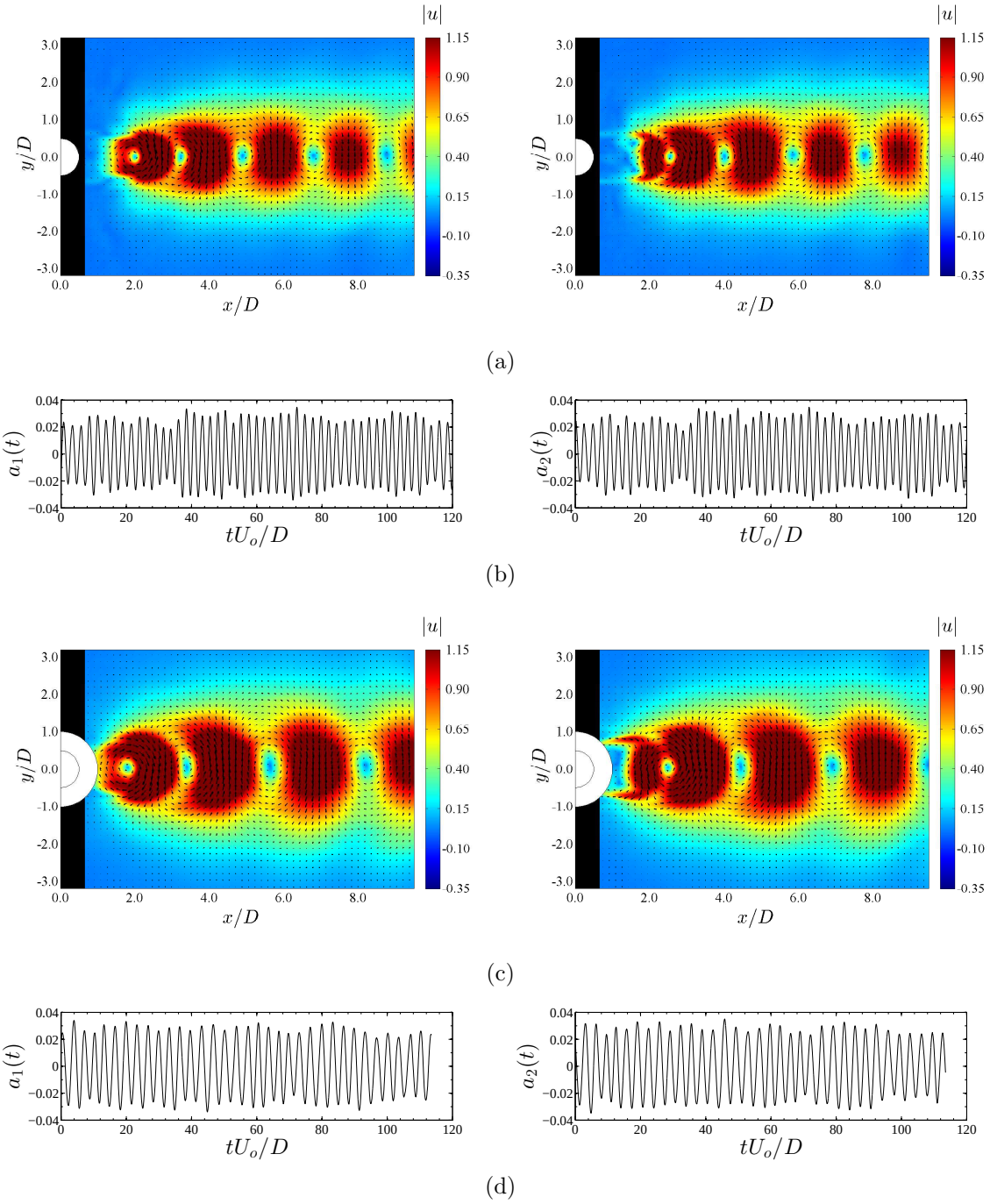

Figure 4.15: First two POD spatial modes and corresponding temporal coefficients for (a-b) a uniform cylinder of base diameter (D) and (c-d) a finned cylinder of $c/D = 0.33$.

that a decrease in pitch ratio leads to more energetic vortex shedding in the wake.

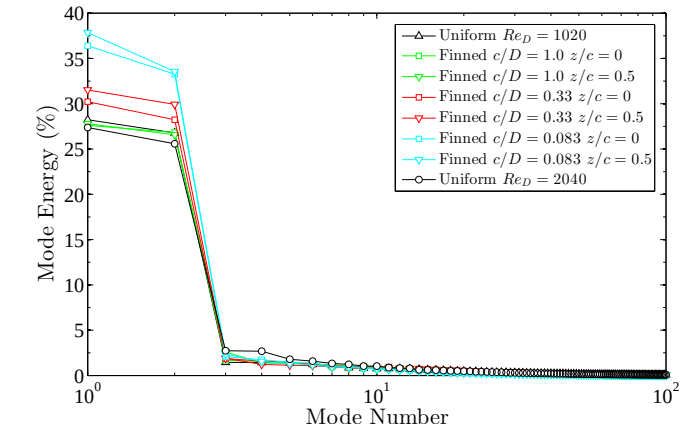

(a)

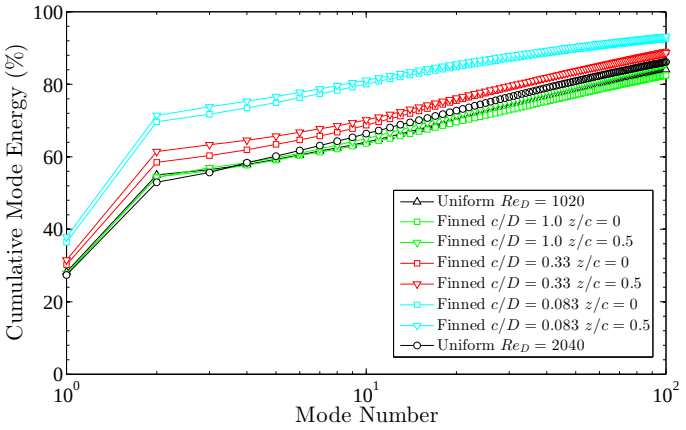

(b)

Figure 4.16: Mode energy distribution for uniform and finned cylinder, (a) distribution of energy % per mode and (b) cumulative total energy versus modes.

4.3.3 Circulation of the wake vortices

Based on the POD analysis, it may be speculated that the addition of fins to a cylinder leads to stronger wake vortex shedding. In order to form a comprehensive description of the vortex development in the wake, it is instructive to start with determining the vorticity flux (K_s) in the boundary layers developing on the models. The vorticity flux in a boundary layer is conserved in the separated shear layer and should be related to the strength of the vortices developing downstream in the wake, as it is the singular source of wall generated vorticity for cylindrical bluff bodies [50–52]. In order to estimate the vorticity flux into the wake by a single shear layer, the transverse profiles of streamwise velocity at the trailing edge of the cylinder in Figure 4.10 are integrated according to Equation 4.2. To capture the total vorticity flux on a single side of the wake, the profiles are numerically integrated from the wake centreline ($y = 0$) to the edge of the shear layer ($y = y_{0.95umax}$).

$$K_s = \int_0^{y_{0.95umax}} u \frac{\partial u}{\partial y} dy \tag{4.2}$$

The results of the vorticity flux calculation are presented in Figure 4.17. For the uniform cylinders of both base ($c/D = \infty$) and fin diameter ($c/D = 0$), the vorticity flux is approximately equal, in agreement with boundary layer theory approximations for uniform cylinders which estimate $K_s \propto U_o^2$ [50]. For $c/D = 1.0$, the wake development exhibits similarities to that of the uniform cylinder of base diameter and the vorticity flux is also approximately equal. As the pitch ratio is lowered further, the vorticity flux decreases approximately 15% for $c/D = 0.33$ and by approximately 30% for $c/D = 0.083$, compared to the reported values for the other models. The explanation for the lower

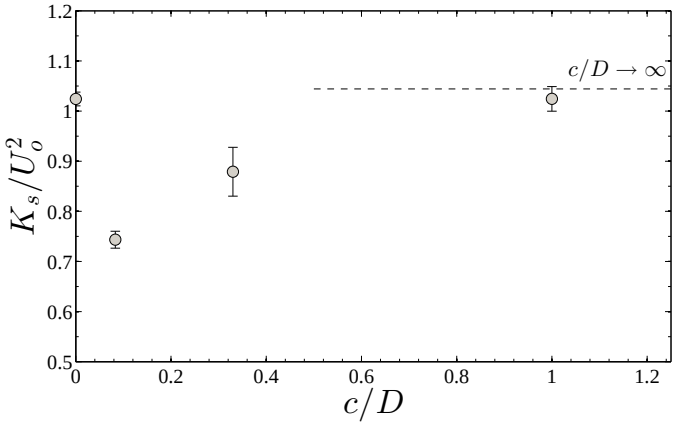

Figure 4.17: Vorticity flux (K_s) advected in the shear layer entering the wake from a given side of the cylinder versus fin pitch ratio (c/D). Calculated by integrating udu/dy from the wake centreline to the edge of the shear layer thickness.

vorticity flux in the shear layers with decreasing c/D is apparent if one considers that the lateral vorticity from the boundary layer development on the fin surfaces leads to a reduction in the streamwise momentum of the flow in the regions $-1 \leq y/D \leq -0.5$ or $0.5 \leq y/D \leq 1$. This leads to decreasing velocities and gradients in the shear layers extending into the wake which contribute to the vorticity flux. Hence, although the shear layer is much thicker for $c/D = 0.083$ (Figure 4.11), the weak gradients present in the high velocity regions lead to less vorticity flux into the wake (Figure 4.10).

Given that vorticity advected in the shear layers is significantly reduced for lower pitch ratios (Figure 4.17), it is surprising that higher fluctuation energies are present in the dominant spatial modes associated with vortex shedding in the wakes of models with low pitch ratio (Figure 4.16). However, from studies on uniform cylinders, it is known that the vorticity deficit ratio K/K_s, that is the ratio between the vorticity flux in the shear

layers and that advected in the wake vortices can vary due to differences in the amount of opposite-sign vorticity entrained into the vortices from the opposite side of the wake.

In order to compare the resulting vorticity flux of the wake vortices developing from the models, the following analysis procedure is employed to phase average the TR-PIV data. For a circular cylinder, the periodic vortex shedding phenomena may be simply represented in a reduced order model by the mean velocity field and the first pair of spatial eigenmodes of the decomposition [110,111]. Thus, the temporal coefficients $a_1(t)$ and $a_2(t)$ (Figure 4.15) magnitude as it varies in time yield signals which may be used to identify the phase progression of the vortex shedding process [98, 110, 111]. In order to extract the phase, the Hilbert transform of the temporal coefficient of the first POD spatial mode ($a_1(t)$) is used. The extracted phase signal is partitioned into bins of $\Delta\theta = \pi/36$, and the instantaneous velocity fields falling in each respective bin are then averaged to obtain the phase averaged velocity field $\vec{u}_\theta(x, y, \theta(t))$. From the phase averaged fields, the average circulation of the wake vortices is calculated by the vorticity thresholding method [25,102], in which the boundary of a vortex is defined by the contour of some percentage of the peak vorticity at the centre of the vortex ($10 - 20\%\omega_{max}$). For each model, the circulation of a wake vortex is measured immediately following detachment from the separated shear layer. Figure 4.18 shows the functional definition utilized of an attached and detached vortex. The vortex is considered attached when the theshold boundary topology is connected to the shear layer. A vortex is considered detached when the threshold boundary completely surrounds the wake vortex, and the area integral over this region (Figure 4.18b) of the phase averaged vorticity field yields the average circulation of the wake vortices. This way, the circulation calculation is applied such that viscous dissipation effects as the vortices

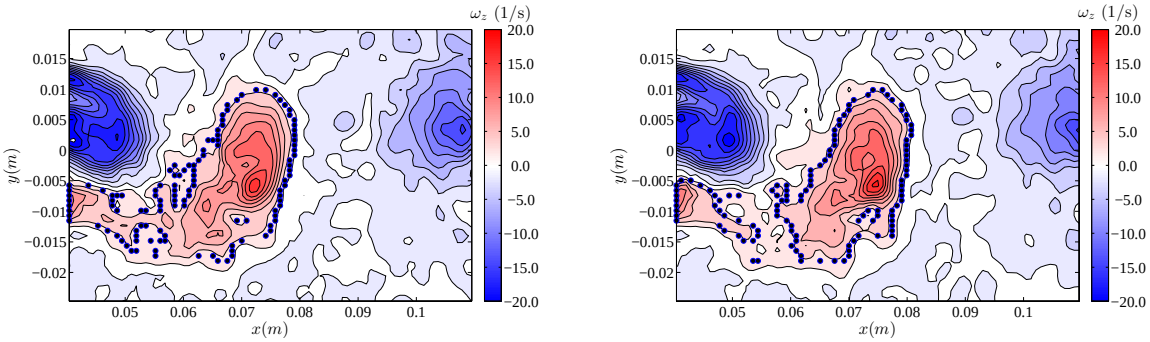

Figure 4.18: Circulation estimation of the wake vortices using vorticity thresholding on the phase averaged fields. Circulation is estimated immediately following the detachment of the vortices into the wake from the shear layer as determined by the threshold topology (a) attached vortex, (b) detached vortex.

are carried downstream are consistent across models.

Based on the circulation calculations, Figure 4.19 shows the vorticity flux of the wake vortices (K) plotted against the fin pitch ratio. The vorticity flux in the wake vortices is equal to the product of the average circulation of the wake vortices (Γ) and the vortex shedding frequency (f_S). The vortex shedding frequencies are obtained from the LDV velocity measurements presented earlier (Figure 4.14). The results indicate that there is a higher vorticity flux in the wake for lower fin pitch ratios, reaching a maximum for $c/D = 0.083$ (Figure 4.19). As remarked earlier, the opposite trend is reported for the amount of vorticity flux in the shear layers for decreasing c/D (Figure 4.17). Based on the discrepancies between the vorticity flux in the shear layers and the vorticity advected in the wake by the vortices, clearly there are changes in the vorticity deficit ratio K/K_s with fin pitch ratio. Figure 4.20 presents the trend in the vorticity deficit ratio K/K_s, that is the ratio between the vorticity flux in the cylinder shear layers, and that ultimately advected

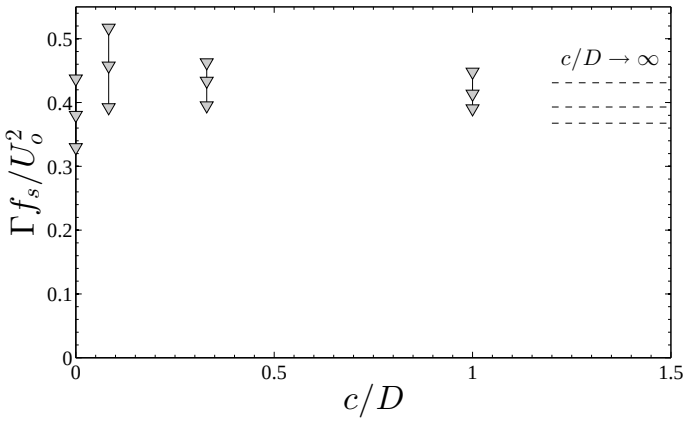

Figure 4.19: Vorticity flux ($K = f_s\Gamma$) advected into the wake by the wake vortices versus fin pitch ratio. For each model, the circulation is calculated in the wake vortices based on 10%, 15%, and 20% vorticity threshold boundaries, leading to progressively lower circulation measurements for each.

in the wake by the vortices. The results show that for the uniform cylinders of diameter D and D_f and for the finned cylinder of the highest pitch ratio $c/D = 1.0$, the vorticity deficit ratio is approximately equal to $K/K_s \approx 0.4$. With decreasing pitch ratio, for $c/D = 0.33$ and 0.083, the vorticity deficit ratio is increased up to a maximum of $K/K_s \approx 0.7$, nearing the maximum reported deficit ratios for flows over uniform circular cylinders [50].

The results show that for lower c/D, the wake vortices are stronger and more efficiently transport the vorticity generated in the cylinder boundary layers into the wake vortices. This agrees with the results of previous studies on finned cylinders, which conjecture that the vortex shedding process is enhanced by the addition of fins compared to uniform cylinders due to sharper, high magnitude peaks in the wake velocity spectra [26, 27]. The lower entrainment of opposing vorticity in the wake vortices for $c/D = 0.33$ and 0.083 can be seen in Figure 4.21, which presents both the phase averaged vorticity fields and sample

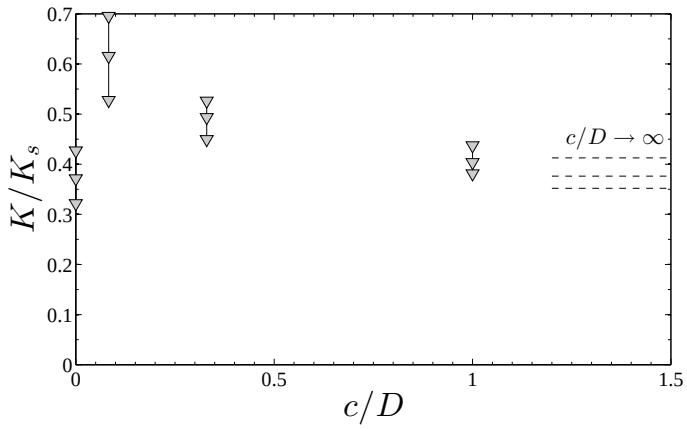

Figure 4.20: Vorticity deficit ratio (K/K_s) of the vorticity advected in the wake by the vortices and the vorticity advected in the shear layers versus fin pitch ratio c/D.

instantaneous vorticity fields at the same phase angle of vortex shedding. The figure shows that despite von Kármán vortices of opposing sign being shed into the wake for each model, as indicated by the phase averaged fields, there is a significant amount of opposing sign vorticity entrained into each wake vortex, as shown in the instantaneous fields. For example, a vortex shed from the shear layer of positive vorticity contains many small scale vortex structures of negative sign. For $c/D = 0.083$ (Figure 4.21f), the instantaneous field shows that the wake vortices contain a significantly smaller amount of entrained vorticity from the opposing shear layer. This leads to the net circulation of the wake vortices being significantly higher for this pitch ratio. For $c/D = 0.33$ (Figure 4.21d), the effect is less pronounced, however, inspection of the instantaneous fields yields an observation of a lesser degree of vorticity entrainment from opposing shear layers than observed for the uniform cylinders and $c/D = 1.0$ (Figures 4.21b and 4.21h).

An explanation for the addition of fins lowering the mixing of vorticity in the wake,

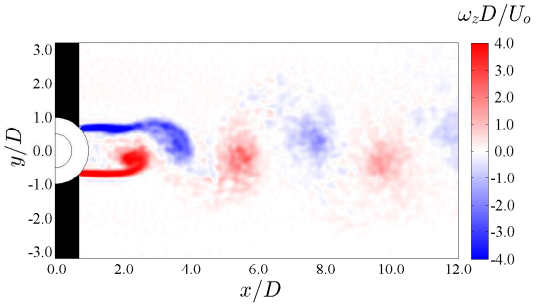

(a) Phase averaged

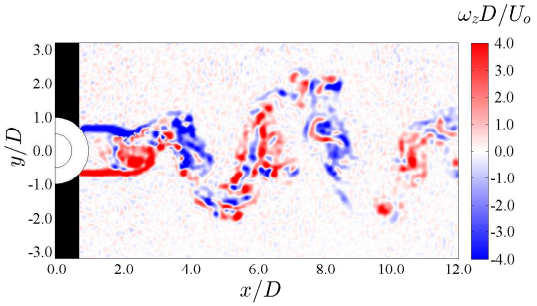

(b) Instantaneous $z/c = 0.5$

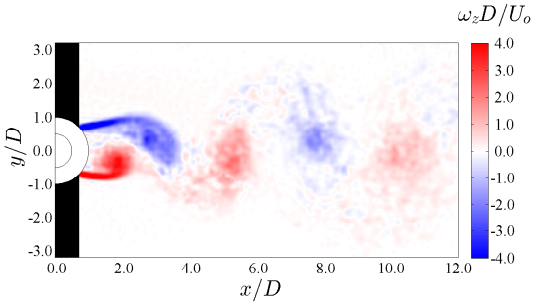

(c) Phase averaged $z/c = 0.5$

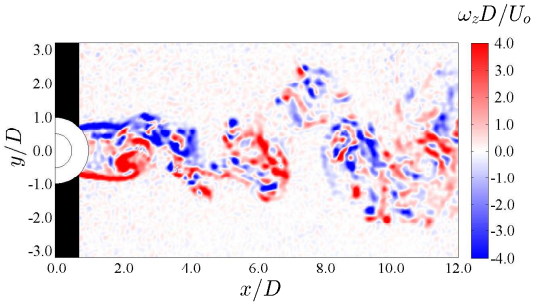

(d) Instantaneous $z/c = 0.5$

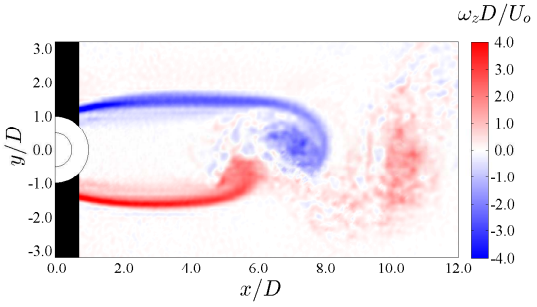

(e) Phase averaged $z/c = 0.5$

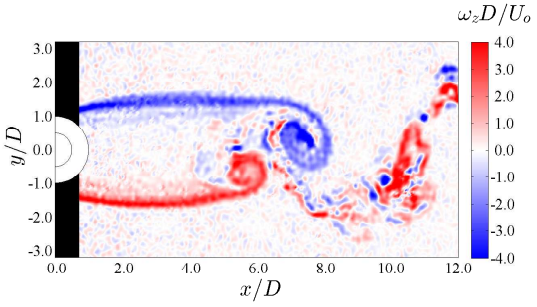

(f) Instantaneous $z/c = 0.5$

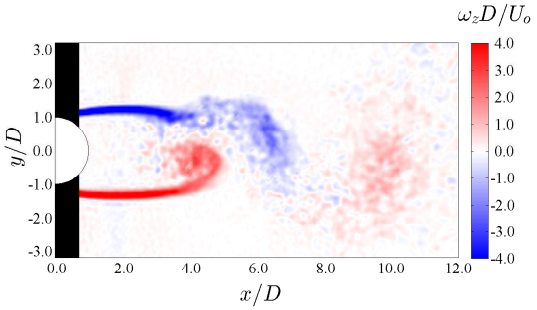

(g) Phase averaged $z/c = 0.5$

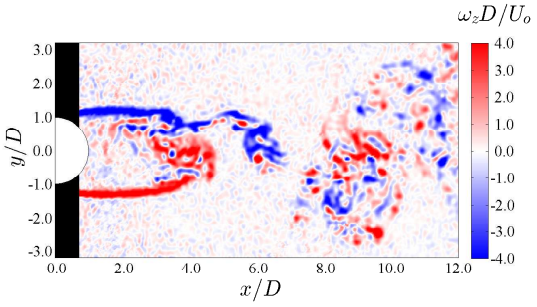

(h) Instantaneous

Figure 4.21: Phase averaged and instantaneous vorticity fields in the wake for (a-b) finned cylinder ($c/D = 1.0$), (c-d) finned cylinder ($c/D = 0.33$), (e-f) finned cylinder ($c/D = 0.083$), and (g-h) uniform cylinder (D_f).

ultimately leading to stronger wake vortices is not readily apparent. However, it is speculated that it is linked to the generation of significant lateral vorticity originating from the boundary layers on the surfaces of the fins. Naito et al. [79] attributes the complete stabilization of the shear layers and suppression of vortex shedding in the wake of uniform cylinders with an attached outer shell of porous media, to the low energy fluid injected in the near wake from through-flow between the porous media which has been subjected to a high degree of dissipation ($|\nabla u|^2$). While the addition of low energy fluid into the wake, and the associated creation of a slip velocity at the surface of the porous cylinder leading to weaker shear layers can both be reasoned to have stabilization effects on the shear layers, it is not immediately apparent that these effects would lead to the decrease in opposing vorticity entrainment observed in the present study, where vortex shedding occurs in the wake. Nevertheless, stabilization effects in the wake due to the injection of the low energy fluid, leading to reduced three-dimensional, fine-scale vortex structures, appear a likely explanation.

4.4 Shedding frequency scaling

The high degree of similarity in the vortex shedding characteristics from finned and uniform cylinders indicates that a universal scaling for the shedding frequency can be explored. For a uniform cylinder, universal Strouhal numbers ($St = fL/U_o$) have been proposed based on using various length scales associated with the vortex development, such as the transverse distance between separated shear layers, transverse distance between streamwise velocity RMS peaks in the wake, and spacing between vortices [1]. For finned cylinders,

several geometric scaling parameters have been explored. Beginning with the work of Mair et al. [26], there have been numerous successful attempts at using an a priori, practical geometric scaling parameter which collapses the shedding frequency data [18, 26, 29]. All the proposed scalings involve modifying the definition of the diameter of the cylinder, such that the characteristic length scale is increased with the addition of fins in order to account for the downward trend in shedding frequency observed for higher fin densities.

The finned cylinder effective diameter (D_{eff}, Equation 4.3) [26] is the most widely used geometric scaling in both studies of solid, parallel finned cylinders [26, 28] and helical, serrated fins [17, 18, 27]. The definition is a function of the base diameter (D), fin diameter (D_f), fin thickness (T), and fin pitch (c), and is based on equating the projected area of the finned cylinder to that of an equivalent uniform cylinder of diameter D_{eff}. Modifications to the definition have been proposed in studies on helical, serrated finned cylinders. Hamakawa et al. [18] proposed that the effective diameter be simply replaced by the fin diameter D_f once a minimum pitch ratio ($c/D \leq 0.16$) is reached for a certain Reynolds number range ($7.6 \times 10^4 \leq Re_D \leq 1.9 \times 10^5$). This approach accounted for the substantial growth of the wake for low c/D, attributed in the current study to be caused by the boundary layer coalescence between the fins.

$$D_{eff} = \frac{(c - T)D + TD_f}{c} \tag{4.3}$$

Figure 4.22 illustrates the result of scaling the shedding frequency data with the effective diameter (St_{Deff}), using the results from the present study, as well as those for previous investigations on the same fin geometry. The data show that this scaling pro-

duces relatively high scatter. In particular, the scaling performs poorly for lower Reynolds numbers (Figure 4.22b) or lower pitch ratios (Figure 4.22a), with the calculated Strouhal numbers falling outside of the Strouhal number range for uniform cylinders of comparable Reynolds numbers $St_{Deff} \approx 0.19$ [12]. Ryu et al. [29], in their study of helical, serrated cylinders with low pitch ratios ($0.08 \leq c/D \leq 0.17$), also found a poor collapse of the shedding frequency data for $1.7 \times 10^4 \leq Re_D \leq 1.85 \times 10^5$ with the cylinder effective diameter. Instead, they proposed scaling the data by the hydraulic diameter (D_h, Equation 4.4). For their paramater range, the hydraulic diameter provided a better collapse of the Strouhal number data from the helical, serrated finned cylinder models [29].

$$D_H = D_f - 4\frac{(c-T)(D_f - D)}{c - T + D_f - D} \tag{4.4}$$

The analysis so far has shown that the effective diameter definition performs poorly in scaling frequency data for finned cylinders at relatively low Reynolds numbers and relatively low fin pitch ratios (Figure 4.22). These observations point towards the failure of these methods to reflect changes in the flow development surrounding the fins. In particular, none of the proposed scalings take into account the boundary layer growth on the fin surfaces, shown to be responsible for marked changes in the flow development with c/D in this study. Since both the effective (D_{eff}) and hydraulic (D_H) diameter definitions are derived purely from geometric considerations, they do not account for the variation of the fin boundary layer thickness with Reynolds number. Hence, where the boundary layers dominate a larger fraction of the span of the cylinder for both lower Reynolds numbers and lower pitch ratios, the effects are most apparent.

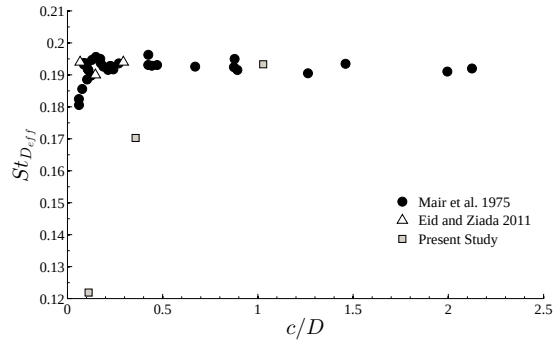

(a)

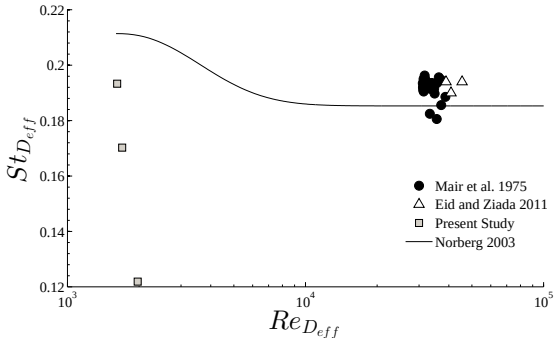

(b)

Figure 4.22: Strouhal number frequency scaling based on the cylinder effective diameter ($St_{Deff} = f_S D_{eff}/U_o$), the variation is shown with respect to (a) Reynolds number based on the effective diameter Re_{Deff} and (b) fin pitch ratio c/D.

Figure 4.23, shows a schematic diagram of the boundary layer growth on the finned surfaces. The boundary layer thickness (δ) and displacement thickness (δ^*) of the boundary layers may be approximated from Blasius' flat plate boundary layer solution [107] (Equations 4.5 and 4.6), with the leading edge of the fin taken as the origin ($x = 0$). The boundary layer thickness and displacement thickness estimated at a distance $D_f/2$ along the fin surface are denoted $\delta_{0.5\pi}$ and $\delta^*_{0.5\pi}$, respectively.

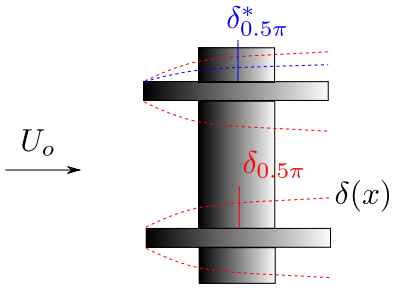

Figure 4.23: Schematic of the boundary layer development on the finned surfaces and denoted displacement thickness (δ) and momentum thickness (δ^*) estimates.

$$\delta = \frac{5.0x}{\sqrt{Re_x}} \tag{4.5}$$

$$\delta^* = \frac{1.72x}{\sqrt{Re_x}} \tag{4.6}$$

To explore the boundary layer effect more clearly in the measurements, it is instructive to consider the variation of the Strouhal number data scaled based on the effective diameter (Figure 4.24a) and the hydraulic diameter (Figure 4.24b), with respect to the ratio of the expected boundary layer thickness to the fin pitch ($\delta_{0.5\pi}/c$). The results reveal a uniform downward trend in the Strouhal number data scaled with the effective diameter, indicated by the dashed line in Figure 4.24a. This illustrates clearly that as the boundary layer thickness grows relative to the fin pitch, the Strouhal number based on the effective diameter does not remain constant. The scaling based on the hydraulic diameter performs poorly for relatively small $\delta_{0.5\pi}/c$ (Figure 4.24b). The observed scatter in the Strouhal number data is hence attributed to changes in the shedding frequency which are related to

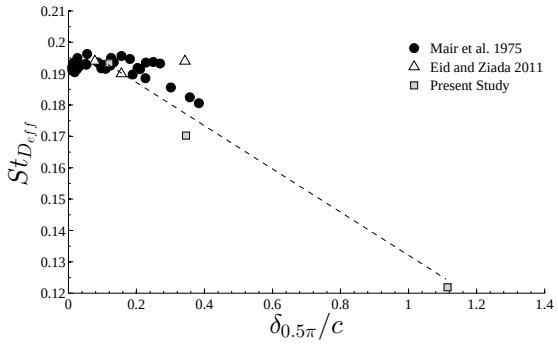

(a)

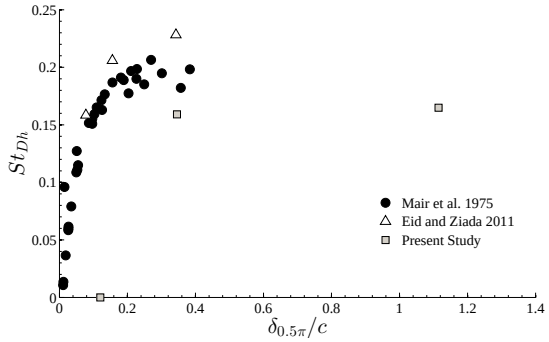

(b)

Figure 4.24: Strouhal number frequency scaling based on (a) the cylinder effective diameter ($St_{Deff} = f_S D_{eff}/U_o$), and (b) the cylinder hydraulic diameter $St_{Dh} = f_S D_h/U_o$, plotted against the ratio of the estimated boundary layer thickness over the fin pitch $\delta_{0.5\pi}/c$.

$\delta_{0.5\pi}/c$, which cannot be accounted for by D_{eff} or D_H since $\delta_{0.5\pi}$ is a function of Reynolds number.

In order to accommodate for the lateral boundary layer growth on the surfaces of the fins in the frequency scaling, the following modification to the effective diameter is proposed to account for the added flow blockage created by the boundary layers. The thickness of the fins (T) is modified, such that the effective thickness of the fins (T^*) is the

physical thickness of the fin plus two predicted displacement thickness' of the fin boundary layer ($T^* = T + 2\delta^*_{0.5\pi}$). With this modification, the effective diameter is now expressed as in Equation 4.7. Substituting in the Blasius solution estimate for the boundary layer displacement thickness ($\delta^*_{0.5\pi}$, Equation 4.6), then results in Equation 4.8. When a critical c/D is reached and the boundary layers coalesce ($c < 2\delta_{0.5\pi}$), the vortex formation has been shown to scale with the fin diameter, with flow being displaced outward and separating at the fin diameter. Thus, the effective diameter definition should be replaced by the fin diameter ($D_{eff} = D_f$, Equation 4.9) when this is the case, following the work of Hamakawa et al. [18].

$$D_{eff*} = D + \left[\frac{2\delta^*_{0.5\pi}}{D} + \frac{T}{D}\right]\frac{(D_f - D)}{c/D} : c > 2\delta_{0.5\pi} \tag{4.7}$$

$$D_{eff*} = D + \left[2.264\left(\frac{D_f}{D}\right)^{1/2}\left(\frac{1}{Re_D}\right)\left(\frac{c}{D}\right) + \frac{T}{D}\right]\frac{(D_f - D)}{c/D} : c > 2\delta_{0.5\pi} \tag{4.8}$$

$$D_{eff*} = D_f : c < 2\delta_{0.5\pi} \tag{4.9}$$

Figure 4.25 presents the frequency data scaled by the modified effective diameter (St_{Deff*}) plotted against the ratio of the expected boundary layer thickness to the fin pitch ($\delta^*_{0.5\pi}/c$). The data now obeys a linear relationship, while demonstrating a better collapse of the results and reduced scatter for all the reported studies. The Strouhal number data now does not show dependence on the differences in the boundary layer thickness

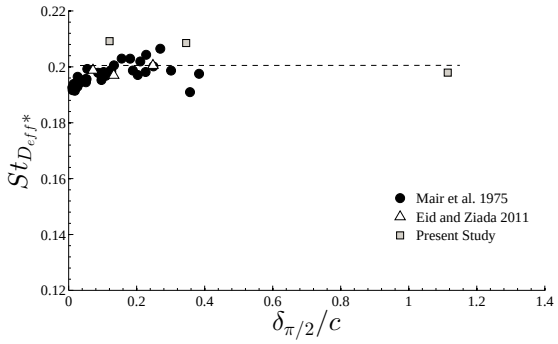

Figure 4.25: Strouhal number frequency scaling based on the cylinder effective diameter ($St_{Deff*} = f_S D_{eff*}/U_o$) versus the ratio of the estimated boundary layer thickness over the fin pitch $\delta_{0.5\pi}/c$.

between the models, hence the new effective diameter definition (D_{eff*}) properly reflects the effect of both Reynolds number and geometric parameters on the flow development. Due to the flat plate approximated used to estimate the boundary layer displacement thickness, the D_{eff*} scaling is supposed to have some limitations. In particular, the flat plate estimates are expected to be more inaccurate for low D_f/D models. For high D_f/D, over the majority of the fin surface, the incoming flow is approximately parallel, in contrast to low D_f/D, where flow curvature around the base cylinder and the associated changing pressure gradient will have effects of the lateral boundary layer growth. Considering this, it is not surprising that the data of Mair et al. [26] exhibits the highest scatter, as they investigate models of lower diameter ratio ($D_f/D = 1.2$ and 1.4) compared to Eid & Ziada ($D_f/D = 1.8$) and the present study ($D_f/D = 2.0$).

4.5 Aerodynamic forces

The force balance measurements were performed for all the uniform and finned cylinder models investigated (Table 3.1). The force balance signals were filtered using a 7th order, low-pass butterworth IIR filter with cutoff frequency $f_c = 2.5Hz$ in order to eliminate the effect of structural vibrations. Further details on the error analysis and calibration procedure developed for the force measurements are included in Appendix C. This section presents the results and trends in the mean and fluctuating forces on the models, and uses pressure extraction techniques, as well as spanwise correlation measurements from the vertical plane PIV data in order to give added insight into the results.

4.5.1 Mean drag

For the presentation of the mean drag coefficient (C_D) results, it is useful to define the fin density (F_ρ) which is expressed in $fins/D$, in place of the pitch ratio c/D, which approaches infinity for the uniform base cylinder (D). The uniform base cylinder corresponds to $F_\rho = 0 fins/D$ and the uniform fin diameter cylinder corresponds to the highest packing density possible for the fin thickness, $F_\rho = 35.7 fins/D$ in this case. Figure 4.26 presents the mean drag coefficient normalized by the projected area of the model ($C_D = F_D/0.5\rho U_o^2 D_{eff} L$). The results show that the drag coefficient for the uniform base cylinder is $C_D = 0.98$, in close agreement with the measurements of Wieselsberger [59]. As fins are added to the base cylinder, the mean drag coefficient increases approximately linearly with increasing fin density (Figure 4.26). The mean drag coefficient continues to increase up to $c/D = 0.083$ ($F_\rho = 12.0$), reaching a maximum of $C_D = 1.87$, but falls below the linear trend. Following

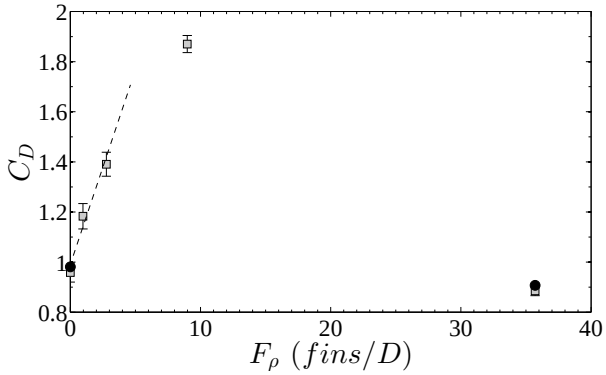

Figure 4.26: Mean drag versus fin density for (□) the present results and (•) Wieselsberger's [59] uniform cylinder results. Error bars calculated based on estimation of the calibration errors.

that, the mean drag coefficient decreases to $C_D = 0.91$ for the uniform cylinder of fin diameter (D_f), in close agreement with the uniform cylinder results of Wieselsberger [59] (Figure 4.26).

The initial linear increase in the mean drag coefficient with the addition of fins to the base cylinder is attributed primarily to the added viscous forces acting on the lateral surfaces of the fins. Hence, with each added fin, the viscous drag increases a constant amount. Since the flow development around the finned cylinder only shows minor changes compared to that of a base uniform cylinder for $c/D = 1.0$ and 0.33, such large changes in the mean drag are unlikely caused by changes in the pressure forcing on the cylinder. Based on this argument, the slope of the linear trend is expected to be Reynolds number dependent, as it relies on the relative contribution of the viscous forces compared to the pressure forces. The levelling off of the linear trend for high F_ρ (Figure 4.26) is attributed to the boundary layer coalescence between the neighbouring fins (e.g., $c/D = 0.083$). The

velocity between the fins is decreased for progressively higher fin densities, reducing the viscous shear on the fin surfaces. Hence, with each added fin, the viscous drag no longer increases independently. The fin density at which the lateral boundary layers coalesce and the linear trend falls off is also expected to be Reynolds numbers dependent since the boundary layer thickness is a function of Reynolds number. Eventually, the fin density is so high that viscous forces on the lateral fin surfaces are small, and the mean drag coefficient will asymptotically approach that of a uniform cylinder of fin diameter ($c/D \rightarrow 0$).

4.5.2 Fluctuating lift

Figure 4.27 presents the RMS of the fluctuating lift coefficient ($C_{L',T}$) measured on the investigated models. The results show that the RMS lift coefficients for a uniform base cylinder ($F_\rho = 0 fins/D$) and a finned cylinder of pitch ratio $c/D = 1.0$ ($F_\rho = 0.97 fins/D$) are approximately $C_{L',T} = 0.012$. For $c/D = 0.33$ ($F_\rho = 2.77 fins/D$), the RMS lift coefficient increases to $C_{L',T} = 0.015$, before decreasing substantially for $c/D = 0.083$ ($F_\rho = 8.98 fins/D$) to $C_{L',T} = 0.006$. The fluctuating lift coefficient for a uniform cylinder of fin diameter ($F_\rho = 35.7 fins/D$) is equal to $C_{L',T} = 0.048$, substantially higher than the rest of the models.

It should be emphasized that the total fluctuating lift coefficient ($C_{L',T}$) acting on a cylinder model depends on how well correlated the shedding is along the span of the model [12]. Since the spanwise correlation of vortex shedding is sensitive to the aspect ratio [38,41] and free-stream conditions in a given facility, the total fluctuating lift coefficient result can vary between experimental facilities and, thus, it is instructive to consider the section lift

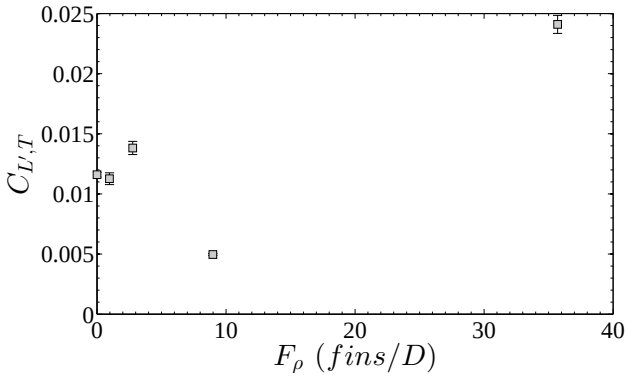

Figure 4.27: RMS fluctuating lift coefficient ($C_{L',T}$) versus fin density (F_ρ). Error bars calculated based on estimation of the calibration errors.

coefficient ($C_{L'}$) instead [12].

Figure 4.28 presents the spanwise correlation coefficient ($R_{uu}(s)$) as it varies along the span of each model. The correlation coefficient is estimated using streamwise velocity signals in the wake obtained from the vertical ($x-z$) plane PIV results at $y/D_{eff} = 0.5$. The streamwise distance into the wake where the velocities were sampled for the correlation measurements was chosen for each model based on the location that yielded the highest correlations, similar to the procedure employed by Ziada et al. [27] in their selection of the transverse location of their roaming hot-wire probes. On the average, the figure shows that the highest correlations are attained for a finned cylinder of pitch ratio $c/D = 0.083$ and a uniform cylinder of fin diameter (D_f). In contrast, notably lower correlations are attained for finned cylinders of pitch ratio $c/D = 0.33$ and 1.0, as well as a uniform cylinder of base diameter (D). The high correlations for the uniform fin diameter cylinder (D_f) and for $c/D = 0.083$ are attributed to aspect ratio effects on the spanwise vortex development. For these models, the aspect ratios ($L/D_{eff*} \approx 10$) are nearing transitional regimes where

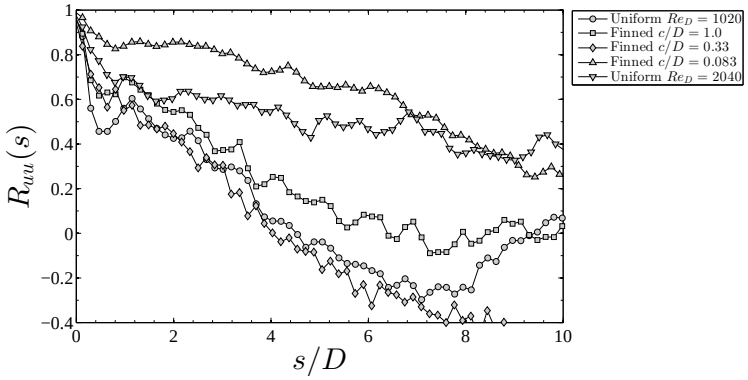

Figure 4.28: Spanwise correlation of vortex shedding $R_{uu}(s)$ along the span of the models. Estimated from PIV measurements of the streamwise velocity signals in the wake.

the end cells of lower frequency merge into a single cell of constant frequency across the span [72, 73]. In contrast, for the higher aspect ratio models, cellular shedding occurs in three distinct cells in the wake, one cell of constant frequency near the midspan of the model and two end cells near the boundaries. This leads to lower reported spanwise correlations compared to the parallel, single cell shedding occurring in the wakes of the uniform cylinder of fin diameter (D_f) and finned cylinder with $c/D = 0.083$.

Sectional RMS lift coefficients can be estimated from measurements of the total RMS lift coefficient ($C_{L,T}$) and spanwise correlation ($R_{uu}(s)$) using Equation 4.10, which integrates the correlation over the finite cylinder length [12, 67]. Since the FOV of the vertical plane PIV measurements only covers approximately $10.5D$ of the cylinder span, in order to integrate the spanwise correlation over the entire cylinder length, exponentials were fit to the correlation data and extrapolated to the full span length. In the cases where the correlations have levelled off to approximately zero within the FOV, the correlation is extrapolated with zero values.

$$C_{L'} = C_{L',T}\frac{1}{L}\left[2\int_0^L (L-s)R_{uu}(s)ds\right]^{1/2} \tag{4.10}$$

Figure 4.29 presents the estimated sectional lift RMS coefficients plotted against the fin density. The sectional RMS lift coefficient is a metric which is independent of spanwise correlation, and hence the observed trends can be related to aspects of the planar flow development in the wake. The results show that with the addition of fins, the sectional RMS lift coefficient is slightly reduced for $c/D = 1.0$ ($F_\rho = 0.97 fins/D$) compared a uniform base cylinder. The sectional RMS lift coefficient then increases substantially for $c/D = 0.33$ ($F_\rho = 2.77 fins/D$) and is substantially reduced for $c/D = 0.083$ ($F_\rho = 8.98 fins/D$). These results may be attributed to the changes in flow development observed with c/D discussed in the previous sections. Specifically, $c/D = 1.0$ shows only small differences in the flow development compared to the uniform cylinder of base diameter, which is reflected by similar magnitudes of the sectional fluctuating lift. The increase in sectional fluctuating lift for $c/D = 0.33$ is attributed to the strengthening of the wake vortices observed in the circulation estimates (Figure 4.19) and the increase in unsteadiness of the shear layers and near wake flow region. The increased unsteadiness in the flow field near the cylinder, for $c/D = 0.33$, can be observed in both the wake Reynolds stresses (Figure 4.4, 4.5, and 4.6) and the first two spatial modes of the POD (Figure 4.15). For $c/D = 0.083$, the stabilization of the wake and displacement of the vortex formation far downstream ($x/D \approx 6.0$, Figure 4.7) leads to the substantial reduction in the observed sectional fluctuating lift, despite having stronger wake vortices for this pitch ratio(Figure 4.19).

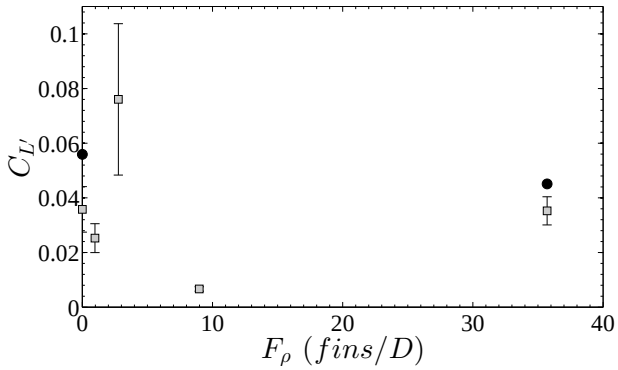

Figure 4.29: Sectional RMS fluctuating lift coefficient ($C_{L'}$) versus fin density (F_ρ) for (□) the present results and (•) Norbergs's [12] uniform cylinder results. Error bars calculated based on estimation of the calibration errors.

4.5.3 Pressure field development

With the mean pressure distribution contributing significantly to the mean drag [59], it is of interest to investigate the mean pressure field development in the wakes of the models. The pressure fields are estimated using horizontal ($x - y$) plane PIV results. Specifically, the Reynolds averaged Navier-Stokes equations (Equation 4.11) are integrated using the omni-directional line integration technique [91].

$$\nabla p(x,y) = \mu \nabla^2 \vec{u} - \rho(\nabla \cdot \tau_{\overline{u'v'}}) - \rho(\vec{u} \cdot \nabla \vec{u}) \tag{4.11}$$

The details of the methodology are discussed in Appendix D. The integration of Equation 4.11 yields the changes in pressure over the domain relative to an integration constant. To obtain absolute pressure fields, the value of the integration constants needs to be defined. For this investigation, the pressures at the transverse and downstream streamwise domain

boundaries ($y/D = \pm 4$, $x/D = 12$) were set such that their average was equal to zero. Given the FOV of the obtained PIV measurements, this approach minimizes the bias error caused by selection of a reference in the wake lower than the free-stream pressure. At these points, the pressure is observed to be closest to the free-stream pressure (p_o) in numerical solutions for flow around cylinders at comparable Reynolds numbers (Appendix D).

Figure 4.30 presents the mean pressure fields for the uniform and finned cylinder models investigated. The pressure fields show the low pressure region in the near wake, associated with the recirculation region upstream of the formation of the wake vortices. Thus, the streamwise and transverse extents of the low pressure contours immediately downstream of the models exhibit the same trends identified in the formation lengths (L_f) and wake widths (L_w) in Figure 4.7. In particular, the low pressure region in the wake for $c/D = 0.083$ is enlarged drastically with the associated flow separation at the fin diameter and elongation of the vortex formation length to $x/D \approx 6$, while the low pressure regions retain similar scales for $c/D = 1.0$, 0.33, and a uniform cylinder of base diameter (D). In the wake of each model, a band of low pressure extends into the wake along $y = 0$, a product of the passage of the low pressure regions in the cores of the wake vortices. This low pressure deficit in the wake is lower for $c/D = 0.083$ and $c/D = 0.33$, compared to for $c/D = 1.0$ and uniform cylinder of base diameter (D), due to the higher circulation wake vortex shedding occurring (Figure 4.19).

Figure 4.31 shows the variation of the base pressure coefficient with fin pitch ratio (c/D) at the mid-pitch location ($z/c = 0.5$) of the models. The base pressure coefficient is estimated from the mean pressure fields at the transverse center ($y = 0$) and at a streamwise distance of $x = D/2$ for the uniform cylinder of base diameter, and $x = D_f/2$ for the

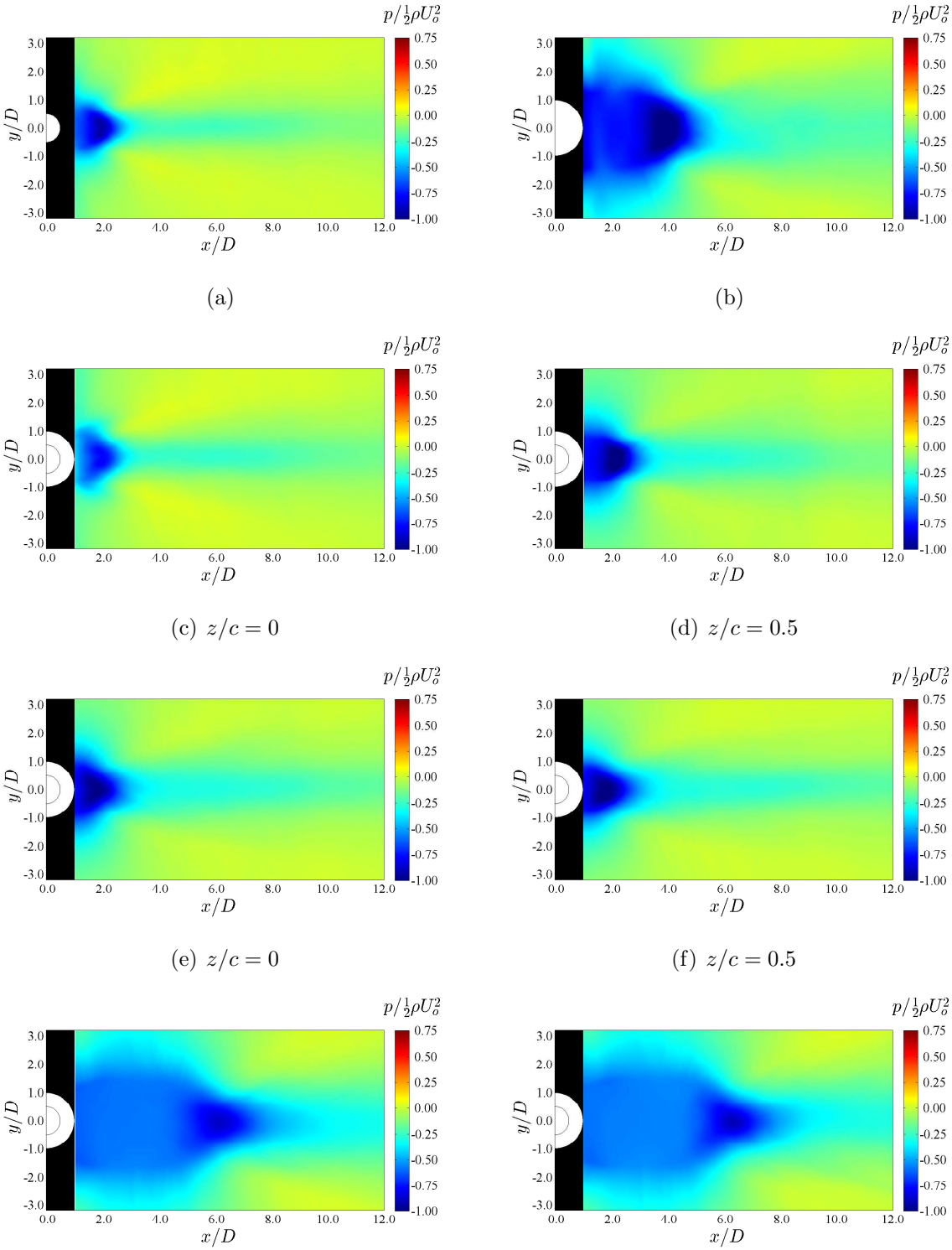

(a) (b)

(c) $z/c = 0$ (d) $z/c = 0.5$

(e) $z/c = 0$ (f) $z/c = 0.5$

(g) $z/c = 0$ (h) $z/c = 0.5$

Figure 4.30: Mean pressure fields for (a) uniform cylinder (D), (b) uniform cylinder (D_f), (c-d) finned cylinder ($c/D = 1.0$), (e-f) finned cylinder ($c/D = 0.33$), and (g-h) finned cylinder ($c/D = 0.083$), calculated using the iterative line integration pressure PIV technique.

remaining models. The results indicate changes between $-0.85 \leq C_{bp} \leq -0.55$ in the base pressure coefficient with pitch ratio. Specifically, the base pressure is approximately constant between the two uniform cylinders ($c/D = \infty$ and 0), and the base pressure decreases slightly with the addition of fins for $c/D = 1.0$ and $c/D = 0.33$, before increasing for $c/D = 0.083$. Previous studies on uniform cylinders have found that increases in base pressure are linked to increases in the formation length [4]. Hence, the observed elongation of the vortex formation length for $c/D = 0.083$ (Figure 4.7) leads to the increase in the base pressure on the model.

The pressure drag acting on a cylindrical bluff body is approximately proportionate to the difference between the stagnation pressure ($C_{pf} \approx 1$) at the front of the cylinder and the base pressure on the aft of the cylinder [4]. Based on the magnitude of the changes in base pressure observed on the models for $c/D = 0.33 - \infty$, compared to the significant increases in total mean drag in the force measurements (Figure 4.26), it must be concluded that the observed trends in the mean drag on the models are entirely attributed to the additive viscous drag from the fin surfaces. The implied changes in the pressure drag, for $c/D = 0.33 - \infty$, are relatively minimal ($< 5\%C_D$) compared to the observed trends in Figure 4.26. Moreover, an increased base pressure would typically lead to a decrease of the net pressure drag on the structure [4], hence $c/D = 0.083$ exhibiting the highest mean drag while simultaneously having the highest base pressure indicates the dominant effect of the viscous drag.

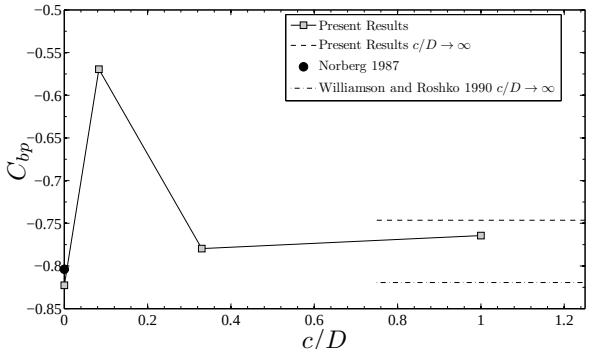

Figure 4.31: Base pressure coefficient (C_{bp}) versus pitch ratio (c/D) from planar measurements at $z/c = 0.5$ and compared to the uniform cylinder results of Norberg [112] and Williamson and Roshko [113].

Chapter 5

Conclusions

The effect of fin pitch ratio ($0.083 \leq c/D \leq 1.0$) on wake development and structural loading characteristics of cylinders with equispaced circular fins has been studied in the shear layer transition regime for $Re_{Deff} = 1020 - 2040$, $D_f/D = 2.0$ and $t/D = 0.028$. For the conditions investigated, vortex shedding occurs in the wake of all models. The near wake development and the characteristics of vortex formation are not affected significantly by the presence of fins at high pitch ratios (e.g., $c/D = 1.0$) compared to a uniform cylinder of base diameter. For $c/D = 0.33$, the effects of the fins on the flow development are more pronounced, with the boundary layer growth on the fin surfaces causing the shear layers to separate further away from the base cylinder. For the lowest pitch ratio investigated ($c/D = 0.083$), the coalescence of the boundary layers between neighbouring fins drastically affects flow development over the model. In particular, the outer flow is directed around the outer surface of the fins away from the base cylinder, leading to a significant enlargement of the vortex formation region. In this case, the wake development is similar to that of

a porous cylinder [30, 78–80], which also features a significant enlargement in the vortex formation length.

The addition of fins leads to the generation of lateral vorticity in the region between the fins due to the boundary layer growth on the fin surfaces. This lateral vorticity leads to a decrease of the spanwise vorticity in the separated shear layers which feed into the wake vortices. Despite the vorticity flux being lower in the shear layers for decreasing c/D, the vorticity advected in the wake vortices is found to be higher for lower c/D. This is attributed to a lower degree of opposite-sign vorticity entrainment between the opposing shear layers during the roll-up process. The injection of low-energy fluid into the vortex formation region from the boundary layers forming on the fins is argued to have a stabilization effect in the wake, as in the case of porous cylinders where shedding may be completely suppressed, which leads to lower entrainment of opposite-signed vorticity from opposing shear layers.

The vortex shedding frequency is shown to decrease with decreasing c/D. When the boundary layers forming on the fins coalesce (e.g., $c/D = 0.083$), separation occurs at the fin diameter, and the shedding frequency becomes comparable to that of a uniform cylinder of fin diameter. A modification of the frequency scaling based on effective diameter is proposed. The proposed scaling accounts for the added flow blockage due to the boundary layer growth using two displacement thickness estimates from Blasius' flat plate boundary layer solution. The resultant Strouhal numbers exhibit significantly less scatter compared to those obtained based on the effective diameter since the proposed formulation accounts for the effect of both the Reynolds number and the geometry of the finned cylinder on the flow development.

Measurements of the structural loading on the models indicate that the mean drag increases with increasing c/D. The initial increase with the addition of fins ($c/D \geq 0.33$) is nearly linear and is attributed to the addition of viscous drag from the boundary layers developing on the fin surfaces. Using planar pressure fields estimated from the $x-y$ plane PIV data, it is shown that the increase of C_D with decreasing c/D is driven primarily by the increase in skin friction, with marginal changes in the pressure field occurring near the cylinder surface. The sectional lift RMS coefficient shows small changes between a uniform base cylinder (D) and a finned cylinder with $c/D = 1.0$. Further decrease in the pitch ratio to $c/D = 0.33$ leads to a substantial increase in the sectional lift RMS coefficient. This increase is attributed to the strengthening of the wake vortices and velocity fluctuations immediately downstream of boundary layer separation. For the lowest pitch ratio $c/D = 0.083$, despite the wake vortices being the strongest, the sectional lift RMS coefficient is reduced substantially in comparison to all other models. This is due to the substantial displacement of vortex formation downstream (up to $x/D \approx 6$), leading to lower fluctuating pressures near the cylinder surface.

Chapter 6

Recommendations

From experience gathered during the course of this study, the author makes the following recommendations pertaining to extension of the current research.

1. The study looks at a rather small geometric parameter range pertaining to finned cylinders. Regarding the pitch ratio effect, it would be beneficial to investigate fin pitch ratios between $c/D = 0.083$ and 1.0 to elucidate the transitional regime between the vastly differing flow developments for $c/D = 1.0$ and $c/D = 0.083$. In addition, with respect to the frequency scaling proposed in the present study, there is lack of data points for the conditions at which the fin boundary layers are nearing coalescence ($\delta_{0.5\pi}/c = 0.25-0.5$). The addition of data points in this regime would further confirm the effectiveness of the proposed frequency scaling.

2. The majority of the observed effect of c/D on the flow development, shedding frequency, and structural loading are linked to the growth of the boundary layers on the

fins. A fundamental study which explores how the boundary layer growth changes with geometrical parameters, in particular D/d and Re_D, will be beneficial for predicting changes in flow development with these parameters.

3. The linear trend in mean drag with increasing fin density is expected to be present for a wide range of Reynolds numbers; however, the slope is hypothesized to change with Re_D as it affects the characteristics of boundary layer development. Thus, performing experiments at multiple Reynolds numbers would provide a correlation for estimating the mean drag on a finned cylinder.

4. Flow visualization in the wakes of the finned cylinders would help elucidate the differences in vorticity entrainment with c/D. It is hypothesized that the lowering of the vorticity entrainment is linked to a decrease in the fine scale three-dimensional vortex structures in the wake. The results would elucidate the stabilization effects of the injection of low energy fluid into the wake.

Bibliography

[1] A. Roshko, "On the wake and drag of bluff bodies," *Journal of Aeronautical Sciences*, vol. 22, p. 124, 1955.

[2] P. W. Bearman, "On vortex street wakes," *Journal of Fluid Mechanics*, vol. 28, p. 625, 1967.

[3] J. Gerrard, "The wakes of cylindrical bluff bodies at low reynolds number," *Phil. Trans. R. Soc. Lond. A*, vol. 288, pp. 351–382, 1978.

[4] A. Roshko, "Perspectives of bluff body aerodynamics," *J. Wind Ind. Aerodyn.*, vol. 49, pp. 79–100, 1993.

[5] C. Williamson, "Vortex dynamics is the cylinder wake," *Annu. Rev. Fluid Mech.*, vol. 28, pp. 477–539, 1996.

[6] M. Zdravkovich, "Review and classification of various aerodynamics and hydrodynamics means for suppressing vortex shedding," *J. Wind Eng. Ind. Aerod.*, vol. 7, pp. 145–189, 1981.

[7] V. Strouhal, "Uber eine besondere Art der Tonerregung," *Ann. Phys. und Chemie*, vol. 10, pp. 216–251, 1878.

[8] T. von Karman, "Uber den mechanismus den widerstands, den ein bewegter korper in einer flussigkeit erfhart," *Gottingen Nachr. Math. Phys. Kl.*, vol. 12, p. 509, 1912.

[9] C. H. K. Williamson, "Oblique and parallel modes of vortex shedding in the wake of a circular cylinder at low Reynolds numbers," *Journal of Fluid Mechanics*, vol. 206, no. December, p. 579, 1989.

[10] J. Gerrard, "The mechanics of the vortex formation region of vortices behind bluff bodies," *J. Fluid Mech.*, vol. 25, p. 401, 1966.

[11] A. Perry, M. Chong, and T. Lim, "The vortex shedding process behind two-dimensional bluff bodies," *J. Fluid Mech.*, vol. 116, p. 77.

[12] C. Norberg, "Fluctuating lift on a circular cylinder: review and new measurements," *J. Fluids Struct.*, vol. 17, pp. 57–96, 2003.

[13] P. Bearman, "Circular cylinder wakes and vortex-induced vibrations," *J. Fluids Struct.*, vol. 27, pp. 648–658, 2011.

[14] R. Blevins, "Flow-induced vibration," *J. Appl. Mech.*, vol. 44, p. 802, 1986.

[15] R. Blevins, "Review of sound induced by vortex shedding from cylinders," *J. Sound Vib.*, vol. 92, pp. 455–470, 1984.

[16] A. Nemoto, A. Takakuwa, and M. Tsutsui, "Flow-induced resonance with various finned tube banks," in *Proceedings of FluidStructure Interaction, Aeroelaciticity, Flow-Induced Vibration and Noise*, vol. 2, (Boston), pp. 311–320, ASME, 1997.

[17] H. Hamakawa, K. Nakashima, T. Kudo, E. Nishida, and T. Fukano, "Vortex shedding from a circular cylinder with spiral fin," *J. Fluid Sci. Tech.*, vol. 3, pp. 787–795, 2008.

[18] H. Hamakawa, T. Fukano, E. Nishida, and M. Aragaki, "Vortex shedding from a circular cylinder with fin," in *AIAA Aeroacoustics Conference*, (Maastricht), pp. 2001–2215, AIAA, 2010.

[19] O. Griffin and S. Ramberg, "Some recent studies of vortex shedding with application to marine tubulars and risers," *J. Energy Resour. Technol.*, vol. 104, pp. 2–13, 1982.

[20] H. Choi, W. P. Jeon, and J. Kim, "Control of Flow Over a Bluff Body," *Annual Review of Fluid Mechanics*, vol. 40, pp. 113–139, Jan. 2008.

[21] I. Yildirim, C. Rindt, and A. A. Steenhoven, "Vortex dynamics in a wire disturbed cylinder wake," *Phys. Fluids*, vol. 22, 2010.

[22] P. W. Bearman, "Investigation of the flow behind a two dimensional model with a blunt trailing edge and fitted with splitter plates," *J. Fluid Mech.*, vol. 21, pp. 241–255, 1965.

[23] M. Matsumoto, "Vortex shedding of bluff bodies: a review," *J. Fluid Stuct.*, vol. 13, pp. 791–811, 1999.

[24] H. Nakamura and T. Igarashi, "Omnidirectional reductions in drag and fluctuating forces for a circular cylinder by attaching rings," *J. Wind Eng. Ind. Aerod.*, vol. 96, pp. 887–899, 2008.

[25] J. McClure, C. Morton, and S. Yarusevych, "Flow development and structural loading on dual step cylinders in laminar shedding regime," *Phys. Fluids*, vol. 92, pp. 455–470, 2015.

[26] W. Mair, P. Jones, and R. Palmer, "Vortex shedding from finned tubes," *J. Sound Vib.*, vol. 39, pp. 293–296, 1975.

[27] S. Ziada, D. Jebodhsingh, D. Weaver, and F. Eisinger, "The effect of fins on vortex shedding from a cylinder in cross-flow," *J. Fluids Struct.*, vol. 21, pp. 689–705, 2005.

[28] M. Eid and S. Ziada, "Vortex shedding and acoustic resonance of single and tandem finned cylinders," *J. Fluids Struct.*, vol. 27, pp. 1035–1048, 2011.

[29] B. Ryu, K. Kim, and J. Boo, "The effect of serrated fins on the flow around a circular cylinder," *J. Mech. Eng. Sci.*, vol. 17, pp. 925–934, 2003.

[30] M. Khashehchi, I. A. Abdi, K. Hooman, and T. Roesgen, "A comparison between the wake behind finned and foamed circular cylinders in cross-flow," *Exp. Therm. Fluid Sci.*, vol. 52, pp. 328–338, 2014.

[31] C. Wang and K. Chi, "Heat transfer and friction characteristics of plain fin-and-tube heat exchangers, part i: new experimental data," *Int. J. Heat Mass Trans.*, vol. 43, pp. 2681–2691, 2000.

[32] C. Wang and K. Chi, "Heat transfer and friction characteristics of plain fin-and-tube heat exchangers, part ii: Correlation," *Int. J. Heat Mass Trans.*, vol. 43, pp. 2693–2700, 2000.

[33] D. Rich, "The effect of fin spacing on the heat transfer and friction performance of multi-row, smooth plate fin-and-tube heat exchangers," *ASHRAE Transactions*, vol. 79, pp. 135–145, 1973.

[34] D. Rich, "The effect of the number of tubes rows on heat transfer performance of smooth plate fin-and-tube heat exchangers," *ASHRAE Transactions*, vol. 81, pp. 307–317, 1975.

[35] Y. Seshimo and M. Fujii, "An experimental study of the performance of plate fin and tube heat exchangers at low reynolds number," in *Proceeding of the 3rd ASME/JSME Thermal Engineering Joint Conference*, pp. 449–454.

[36] M. Provansal, C. Mathis, and L. Boyer, "Benard-von Karman instability: transient and forced regimes," *J. Fluid Mech.*, vol. 182, pp. 1–22, 1987.

[37] J. Hunt, A. Wray, and P. Moin, "Eddies, streams, and convergence zones in tubulent flows," in *Proceedings fof the Summer Program*, no. N89-24555, Center for Turbulence Research, 1988.

[38] D. Gerich and H. Eckelmann, "Influence of end plates and free ends on the shedding frequency of circular cylinders," *Journal of Fluid Mechanics*, vol. 122, p. 109, 1982.

[39] H. Eisenlohr and H. Eckelmann, "Vortex splitting and its consequence in the vortex street wake of cylinders at low Reynolds number," *Physics of Fluids A*, vol. 1, pp. 189–192, 1989.

[40] G. Miller and C. Williamson, "Control of three-dimensional phase dynamics in a cylinder wake," *Exp. Fluids*, vol. 18, pp. 26–35, 1994.

[41] C. Norberg, "An experimental investigation of the flow around a circular cylinder: influence of aspect ratio," *J. Fluid Mech.*, vol. 258, pp. 287–316, 1994.

[42] C. H. K. Williamson, "Three-dimensional wake transition," *Journal of Fluid Mechanics*, vol. 328, p. 345, 1996.

[43] M. Bloor, "The transition to turbulence in the wake of a circular cylinder," *J. Fluid Mech.*, vol. 19, pp. 290–304, 1964.

[44] M. Braza, P. Chassaing, and H. H. Minh, "Numerical study and analysis of the pressure and velocity fields in the near wake of a cylinder," *J. Fluid Mech.*, vol. 165, pp. 79–130, 1986.

[45] O. Inoue and A. Sakuragi, "Vortex shedding from a circular cylinder of finite length at low Reynolds numbers," *Physics of Fluids*, vol. 20, 2008.

[46] C. Williamson and G. Miller, "Three-dimensional phase dynamics in a cylinder wake," *Meccanica*, vol. 29, pp. 411–429, 1994.

[47] C. Williamson, "The natural and forced formation of spotlike vortex dislocations in the transition of a wake," *J. Fluid Mech.*, vol. 243, pp. 393–441, 1992.

[48] C. Morton and S. Yarusevych, "Vortex Shedding in the Wake of a Dual Step Cylinder," pp. 1–6, 2012.

[49] C. Morton, "Turbulent Vortex Shedding From a Dual-Step Cylinder : Influence of Diameter Ratio and Aspect Ratio," pp. 1–6, 2013.

[50] E. Berger and R. Wille, "Periodic flow phenomena," *Annu. Rev. Fluid Mech.*, vol. 4, pp. 313–340, 1972.

[51] F. Abernathy and R. Kronauer, "The formation of vortex streets," *J. Fluid Mech.*, vol. 13, pp. 1–20, 1962.

[52] M. Zdravkovich, "Smoke observations of the formation of a Karman vortex street," *J. Fluid Mech.*, vol. 37, pp. 491–499, 1969.

[53] V. Timme, "Uber die Geschwindigkeitsverteilung in Wirbeln," *Band*, vol. XXV, pp. 205–225, 1957.

[54] M. Davies, "A comparison of the wake structure of a stationary and oscillating bluff body using a conditional averaging technique," *J. Fluid Mech.*, vol. 75, pp. 209–231, 1976.

[55] P. Kundu and I. Cohen, *Fluid Mechanics*. Academic Press, 2002.

[56] W. Dunn and S. Tavoularis, "Experimental studies of vortices shed from cylinders with a step-change in diameter," *Journal of Fluid Mechanics*, vol. 555, p. 409, May 2006.

[57] C. Morton and S. Yarusevych, "Vortex shedding in the wake of a step cylinder," *Physics of Fluids*, vol. 22, no. 2010, p. 083602, 2010.

[58] J. A. Bourgeois, P. Sattari, and R. J. Martinuzzi, "Alternating half-loop shedding in the turbulent wake of a finite surface-mounted square cylinder with a thin boundary layer," *Physics of Fluids*, vol. 23, no. 2011, 2011.

[59] C. Wieselsberger, "New data on the law of hydro and aerodynamic resistance," *Phys. Zeitschrift*, vol. 22, pp. 321–328, 1921.

[60] H. Drescher, "Messung der auf querangestromte Zylinder ausgeubten zeitlich veranderten Drucke," *Zeitschrift fur Flugwissenschaften und Weltraumforschung*, vol. 4, pp. 17–21, 1956.

[61] D. J. Tritton, "Experiments on the flow past a circular cylinder at low Reynolds numbers," *Journal of Fluid Mechanics*, vol. 6, no. 1936, p. 547, 1959.

[62] E. Relf, "Discussion of the Results of Measurements of the Resistance of Wires, with Some Additional Tests on the Resistance of Wires of Small Diameter," Tech. Rep. Reports and Memoranda No. 102, British A.C.A.

[63] A. Thom, "A.r.c.," Tech. Rep. Reports and Memoranda No. 1194, British A.C.A., 1929.

[64] K. Lam, F. Wang, and R. So, "Three-dimensional nature of vortices in the near wake of a wavy cylinder," *J. Fluids Struct.*, vol. 19, pp. 815–833, 2004.

[65] M. Moeller and P. Leehay, "Unsteady forces on a cylinder in cross flow at subcritical reynolds numbers," in *ASME Symposium on Flow-Induced Vibrations*, vol. 1, (New Orleans), pp. 57–71, ASME, 1984.

[66] P. Leehay and C. Hanson, "Aeolian tones associated with resonated vibration," *Journal of Sound and Vibration*, vol. 13, pp. 465–483, 1971.

[67] J. Ribeiro, "Fluctuating lift and its spanwise correlation on a circular cylinder in a smooth and in a turbulent flow: a critical review," *Journal of Wind Engineering and Industrial Aerodynamics*, vol. 40, pp. 179–198, 1992.

[68] W. Blake, *Mechanics of Flow-Induced Sound and Vibration*, vol. 1. New York: Academic Press, 1986.

[69] M. Arie and H. Rouse, "Experiments on two-dimensional flow over a normal wall," *J. Fluid Mech.*, vol. 1, pp. 129–141, 1956.

[70] C. Farell, "Flow around fixed circular cylinders: fluctuating loads," *ASCE. Journal of the Engineering Mechanics Division*, vol. 107, pp. 565–587, 1981.

[71] M. Zdravkovich, *Flow Around Circular Cylinders, Vol 1: Fundamentals*. New York: Oxford University Press, 1997.

[72] G. West and T. Fox, "On the use of endplates with circular cylinders," *Experiments in Fluids*, vol. 9, pp. 237–239, 1990.

[73] P. Stansby, "The effect of end plates on the base pressure coefficient of a circular cylinder," *Aeronaut. J.*, vol. 78, pp. 36–37, 1974.

[74] D. Sumner, "Flow above the free end of a surface-mounted finite-height circular cylinder: A review," *Journal of Fluids and Structures*, vol. 43, pp. 41–63, 2013.

[75] M. M. Zdravkovich, V. P. Brand, G. Mathew, and A. Weston, "Flow past short circular cylinders with two free ends," *Journal of Fluid Mechanics*, vol. 203, p. 557, 1989.

[76] S. Szepressy and P. Bearman, "Aspect ratio and end plate effects on vortex shedding from a circular cylinder," *Journal of Fluid Mechanics*, vol. 234, pp. 191–217, 1992.

[77] R. Keefe, "Investigation of the fluctuating forces on a stationary circular cylinder in a subsonic stream and of the associated sound field," *The Journal of the Acoustical Society of America*, vol. 34, pp. 1711–1714, 1962.

[78] T. Sueki, T. Takaishi, M. Ikeda, and N. Arai, "Application of porous material to reduce aerodynamic sound from bluff bodies," *Fluid Dyn. Res.*, vol. 42, 2010.

[79] H. Naito and K. Fukagata, "Numerical simulation of flow around a circular cylinder having porous surface," *Phys. Fluids*, vol. 24, 2012.

[80] J. Fransson, P. Konieczny, and P. Alfredsson, "Flow around a porous cylinder subject to continuous suction or blowing," *Journal of Fluids and Structures*, vol. 19, pp. 1031–1048, 2004.

[81] D. Hammond and L. Redekopp, "Global dynamics of symmetric and asymmetric wakes," *J. Fluid Mech.*, vol. 331, pp. 231–260, 1997.

[82] C. Morton and S. Yarusevych, "On vortex shedding from low aspect ratio dual step cylinders," *Journal of Fluids and Structures*, vol. 44, pp. 251–269, 2014.

[83] Shan and Sekulic, *Fundamentals of Heat Exchanger Design*. John Wiley and Sons, 2003.

[84] M. Zdravkovich, *Flow Around Circular Cylinders, Vol 2: Applications*. New York: Oxford University Press, 2003.

[85] H. Hamakawa, H. Matsuoka, K. Hosokai, E. Nishida, and E. Kurihara, "Characteristics of aerodynamics sound radiated from two finned cylinders," in *Proceedings of the ASME 2014 Pressure Vessels and Piping Conference*, (Anaheim, California, USA), ASME, 2014.

[86] H. Hamakawa, T. Fukano, E. Nishida, and K. Muraoka, "Vortex shedding in normal triangular tube arrays with closely mounted twist serrated fin," in *Proceedings of International Conference on Jets, Wakes and Separated Flows*, (Japan), pp. 543–548, JSME, 2005.

[87] H. Hamakawa, K. Komatsu, E. Nishida, and T. Fukano, "Effect of Fin on Vortex Shedding from Fin-Tube Banks," *Nihon Kikai Gakkai Nenji Taikai Koen Ronbunshu*, vol. 7, 2006.

[88] B. W. van Oudheusden, "PIV-based pressure measurement," *Measurement Science and Technology*, vol. 24, p. 032001, 2013.

[89] T. Baur and J. Kongeter, "Piv with high temporal resolution for the determination of local pressure reductions from coherent turbulent phenomena," in *3rd Int. Workshop on Particle Image Velocimetry*, (Santa Barbara), pp. 101–106, 1999.

[90] J. O. Dabiri, S. Bose, B. J. Gemmell, S. P. Colin, and J. H. Costello, "An algorithm to estimate unsteady and quasi-steady pressure fields from velocity field measurements.," *The Journal of experimental biology*, vol. 217, pp. 331–6, 2014.

[91] X. Liu and J. Katz, "Instantaneous pressure and material acceleration measurements using a four-exposure PIV system," *Experiments in Fluids*, vol. 41, pp. 227–240, 2006.

[92] R. Gurka, A. Liberzon, D. Hefetz, D. Rubinstein, and U. Shavit, "Computation of pressure distribution using piv velocity data," in *3rd Int. Workshop on Particle Image Velocimetry*, (Santa Barbara), pp. 671–676, 1999.

[93] J. J. Charonko, C. V. King, B. L. Smith, and P. P. Vlachos, "Assessment of pressure field calculations from particle image velocimetry measurements," *Measurement Science and Technology*, vol. 21, p. 105401, 2010.

[94] D. Violato, P. Moore, and F. Scarano, "Lagrangian and Eulerian pressure field evaluation of rod-airfoil flow from time-resolved tomographic PIV," *Experiments in Fluids*, vol. 50, pp. 1057–1070, 2011.

[95] R. De Kat and B. Van Oudheusden, "Instantaneous planar pressure determination from PIV in turbulent flow," *Experiments in Fluids*, vol. 52, pp. 1089–1106, 2012.

[96] M. Bansal, "Experimental and numerical investigation of three equispaced cylinders in cross-flow," Master's thesis, University of Waterloo, 2014.

[97] C. Morton, "Experimental and numerical investigations of the flow development over cylinders with stepwise discontinuities in diameter," Master's thesis, University of Waterloo, 2010.

[98] C. Morton, *Three-Dimensional Wake Development and Structural Loading on Dual Step Cylinders in Cross-Flow*. PhD thesis, University of Waterloo, 2014.

[99] S. Kheirkhah, "Vortex-induced vibrations of a pivoted circular cylinder and their control using a tuned-mass damper," Master's thesis, University of Waterloo, 2011.

[100] C. Willert and M. Gharib, "Digital particle image velocimetry," *Exp. Fluids*, vol. 10, pp. 181–193, 1991.

[101] J. Westerweel, "Fundamentals of digital particle image velocimetry," *Measurement Science and Technology*, vol. 8, pp. 1379–1392, 1997.

[102] M. Raffel, C. E. Willert, S. T. Wereley, and J. Kompenhans, *Particle Image Velocimetry*. Spriner-Verlag, 2007.

[103] A. Sciacchitano, F. Scarano, and B. Wieneke, "Multi-frame pyramid correlation for time-resolved PIV," *Experiments in Fluids*, vol. 53, pp. 1087–1105, 2012.

[104] S. Tavoularis, *Measurement in Fluid Mechanics*. Cambridge University Press, 2005.

[105] R. J. Adrian and C. S. Yao, "Power spectra of fluid velocities measured by laser Doppler velocimetry," *Experiments in Fluids*, vol. 5, pp. 17–28, 1987.

[106] A. Perry and M. Chong, "A description of eddying motions and flow patterns using critical-point concepts," *Annu. Rev. Fluid Mech.*, vol. 19, pp. 125–155.

[107] H. Blasius, "Grenzschichten in Flussigkeiten mit kleiner Reibung," *Z. Math. Phys.*, vol. 56, pp. 1–37, 1908.

[108] T. Fox and G. West, "On the use of endplates with circular cylinders," *Experiments in Fluids*, vol. 9, pp. 237–239, 1990.

[109] J. Lumley, *Stochastic tools in turbulence*. New York: Academic Press, 1972.

[110] B. Oudheusden, F. Scarano, N. Hinsberg, and D. Watt, "Phase resolved characterization of vortex shedding inthe near wake of a square-section cylinder at incidence," *Exp. Fluids*, vol. 39, pp. 86–98, 2005.

[111] R. Perrin, M. Braza, E. Cid, S. Cazin, A. Barthet, A. Sevrain, C. Mockett, and F. Thiele, "Obtaining phase averaged turbulence properties in the near wake of a circular cylinder at high Reynolds number using POD," *Exp. Fluids*, vol. 43, pp. 341–355, 2007.

[112] C. Norberg, "Effects of Reynolds numbers and a low-intensity freestream turbulence on the flow around a circular cylinder," *Chalmers Univ. Technol. Publ. No. 87/2*, vol. S, pp. 412–496, 1987.

[113] C. Williamson and A. Roshko, "Measurements of base pressure in the wake of a cylinder at low Reynolds numbers," *Z. Flugwiss Weltraumforsch*, vol. 14, pp. 38–46, 1990.

[114] F. White, *Fluid Mechanics*. McGraw-Hill, 2009.

[115] J. Westerweel, "Theoretical analysis of the measurement precision in particle image velocimetry," *Experiments in Fluids*, vol. 29, no. 1, pp. S003–S012, 2000.

[116] R. Keane and R. Adrian, "Theory of cross-correlation analysis of PIV images," *Appl. Sci. Res.*, vol. 49, pp. 191–215, 1992.

[117] R. de Kat, B. W. van Oudheusden, and F. Scarano, "Instantaneous planar pressure field determination around a square-section cylinder based on time-resolved stereo-PIV," *14th Int Symp on Applications of Laser Techniques to Fluid Mechanics*, pp. 7–10, 2008.

[118] R. de Kat, *Instantaneous planar pressure determination from particle image velocimetry.* PhD thesis, Delft University of Technology, 2012.

[119] R. de Kat and B. Ganapathisubramani, "Pressure from particle image velocimetry for convective flows: a Taylors hypothesis approach," *Measurement Science and Technology*, vol. 24, p. 024002, 2013.

Appendices

Appendix A

Free-stream characterization

The current flow conditioning design in the flume is shown in Figure A.1. Water enters the settling chamber from the head tank through primary and secondary pipe outlets. Honeycomb place horizontally in the settling chamber prevents a large recirculating flow from developing in the settling chamber. The flow exits the settling chamber through a plastic/wood grid ($G1$) and through two turbulence screens ($SC0$ and $SC1$). The water then flows through a 2.42 deg diffuser section over $2.46m$ before entering an aluminium honeycomb of cell size $M = 9.5mm$ and aspect ratio $L/M = 10.1$ followed by an aluminium grid with porosity $\beta = 0.66$, cell size $M = 5.08cm$ and $w = 0.953cm$. Before entering the test section, the flow passes through five turbulence reducing screens, the first three of higher porosity and wire Reynolds number ($SC2$, $SC3$, and $SC4$), and the last two fine screens ($SC5$, $SC6$).

The water flume facility free-stream characteristics were extracted from a long sample, single-point LDV measurement of the streamwise velocity and planar PIV measurements

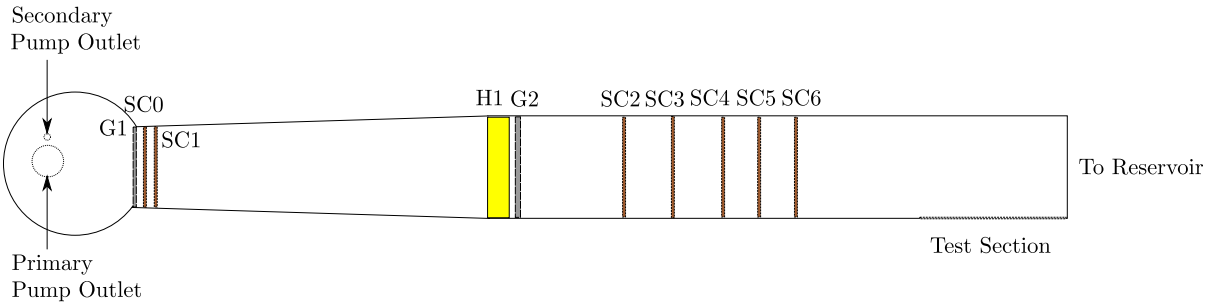

Figure A.1: Water flume flow conditioning elements, SC denotes aluminium screens, G large scale grids, and H aluminium honeycomb.

in horizontal $(x - y)$ and vertical $(x - z)$ planes with the models removed from the test section. The measurements were centred in-line with the model mounting axis $(x, y, z = 0)$. Careful control of the water height in the flume and cleanliness of the flow conditioning elements throughout the experimental campaign minimized deviation from the characteristics reported in this section.

The LDV signal was collected for a one hour duration and re-sampled at a constant $f_{acq} = 10Hz$. The resulting single-point, streamwise velocity signal had a mean of $87.4mm/s$ and turbulence intensity of 1.2%. The spectrum of the velocity signal is shown in Figure A.2. The spectrum exhibits a small peak at $f \approx 0.1Hz$, which has been attributed to low frequency global oscillations of the mean streamwise velocity associated with surface waves in the water flume [97].

Mean velocity profiles obtained with PIV measurements along the transverse direction (Figure A.3a) for $-100mm \leq y \leq 100mm$ and vertical direction (Figure A.3b) for $-100mm \leq z \leq 100mm$ show the uniformity of the free-stream (α_u) across the test section. The min-max flow uniformity is $\alpha_u = 4.3\%$ in the transverse direction and 1.4% in

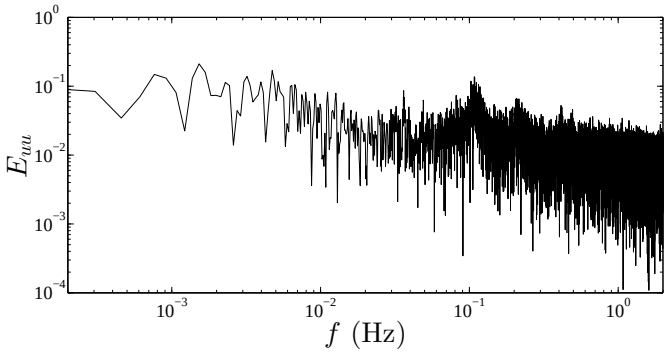

Figure A.2: Spectrum of the streamwise free-stream velocity acquired from LDV measurement.

the vertical direction. This is a slightly higher uniformity estimate than that characterized upon the installation of the flow conditioning elements ($< 3\%$ in 2010) [97]. However, the condition of the turbulence screens is assumed to have deteriorated over this time period, and their redesign and/or replacement is the subject of ongoing work. The free-stream velocity value used as reference in this study ($U_o = 86.5mm/s$) is the inclusive mean of both the vertical and horizontal plane velocity measurements.

The free-stream references used in the thesis are the velocity ($U_o = 0.0865m/s$) as measured with the LDV system with the models removed, and the water density ($\rho_w = 998.7kg/m^3$) and viscosity ($\mu_w = 1.611 \times 10^{-3} Pa \cdot s$) for a measured water temperature of 17° [114].

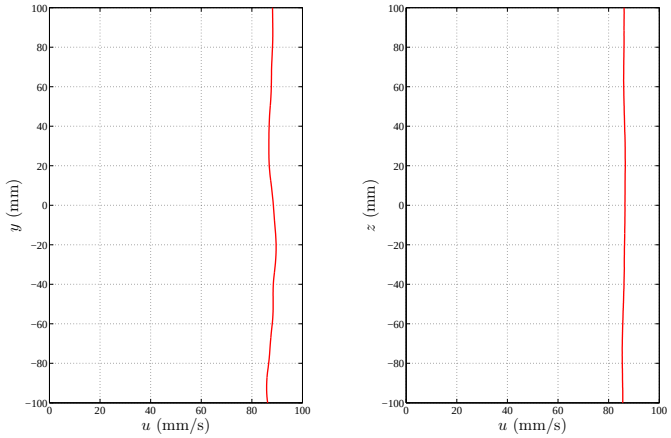

(a) (b)

Figure A.3: Profiles of the streamwise free-stream velocity in the (a) transverse direction for $-100mm \leq y \leq 100mm$ and (b) spanwise direction for $-100mm \leq z \leq 100mm$, acquired from PIV measurement.

Appendix B

Experimental uncertainty

B.1 LDV Uncertainty

The most significant error source in LDV measurements is typically attributed to a velocity bias error which originates from higher velocity particles crossing the measurement volume more often than low velocity particles [104]. Equation B.1 gives an order of magnitude estimate of the velocity bias, which depends on the mean (U) and RMS ($\bar{u'}$) of the measured velocity signal in order to calculate the true velocity (U_T).

$$U/U_T \approx 1 + \frac{\bar{u'}^2}{U_T^2} \tag{B.1}$$

Based on the wake velocity obtained at x/D_{eff} and $y/D_{eff} = 0.5$ for each model, the velocity bias error is estimated based on Equation B.1 to be between $3.44 - 10.74 mm/s$. This is a conservative estimate, and it is known that re-sampling of the velocity data at

a constant frequency reduces this velocity bias error [105]. After re-sampling the velocity signal, the mean value decreases such that the bias error is estimated to be between $0 - 7.23mm/s$. The highest bias error estimate ($7.23mm/s$) corresponds to the velocity signal in the wake of the $c/D = 0.083$ finned cylinder model, where the measurement volume lies in a low velocity region in the wake. Despite these relatively high error values, the spectral content of the velocity signals should not be affected, which is the utility of the LDV measurements in this study.

The MSE miniLDV probe sensor has a repeatability error of 0.1% and a total accuracy of 0.3% according to the manufacturers specifications. The mean particle diameter is $10\mu m$ and is estimated to vary from $0 - 20\mu m$, which will contribute to a slight over prediction of RMS velocity values due to the randomness associated with the particle size [104]. The optics within the LDV laser insure that the dual-beam is parallel, and a digital level is used to insure that it is mounted within $\pm 0.1^{\circ}$ of horizontal. The alignment of the laser volume in the wake is done using the Photron high speed cameras and the alignment is estimated to be accurate within $\pm 0.01D$. Therefore, errors associated with the mounting and alignment of the probe are assumed negligible.

Error in the extraction of the shedding frequency (f_S) from the LDV measurements is due to the finite resolution of the calculated spectra. The velocity signal was sampled at a constant $f_{acq} = 20Hz$ and partitioned into segments of 2048 samples resulting in a spectral resolution of $\pm 0.0049Hz$ or $\pm 0.001fD/U_o$, which is $\pm 0.5\%$ the measured shedding frequency from the base cylinder.

B.2 PIV Uncertainty

Error estimation for PIV experimentation is known to be difficult to quantify analytically [101, 102]. In general, sources of error may be subdivided into: (i) errors due to geometric configuration and calibration (i.e., how accurately is the magnification factor (K) known in $mm/pixel$) and (ii) errors in determining the particle displacement (δ_x) from the cross-correlation and peak detection of the images.

Errors in the determination of the magnification factor (ϵ_K) are well-defined from the calibration procedure. The image calibration is performed with the aid of a calibration plate with a square grid of milled holes at known spacings $1.5 \pm 0.005in$. The laser sheet is aligned parallel with the edge of the calibration plate, such that the error in the difference in height of the calibration plate and the laser sheet is approximately half the laser sheet thickness ($1mm$). This amounts to a total uncertainty in the calibration distance between the grid points of $\epsilon_{lc} = \pm 0.136mm$. The magnification factor (K) is then determined by reading the amount of pixels between the milled holes on the calibration plate (N_{pix}) over the known distance between the calibration points (l_c). There is an uncertainty associated with the determination of the number of pixels between the grid points. The calibration procedure uses a number of grid points such that this error is minimized, however a conservative estimate is $\epsilon_N = \pm 0.5 pixels$. These errors combine to determine the total magnification error according to Equation B.2.

$$\epsilon_K = K\sqrt{(\epsilon_{lc}/l_c)^2 + (\epsilon_N/N_{pix})^2} \tag{B.2}$$

The magnification factor varies slightly between PIV planes, but is approximately $K \approx$

$0.2mm/pixel$, and typically the calibration involves approximately $N_{pix} \approx 550$ over $l_c = 4.5in$. This leads to a calculated error in the determination of the magnification factor of approximately $\epsilon_K = 0.00102mm/pixel(0.51\%)$.

The errors involved in the cross correlation of the images to recover the particle displacements is more difficult to quantify, but typically is the main contributing factor to the random error in PIV measurements. For a good experimental set-up, the use of sub-pixel interpolation has resulted in estimates of the correlation error between $\epsilon_{cc} = 0.04 - 0.1pixels$ [115, 116]. Based on $U_o = 86.5mm/s$ and the 16×16 interrogation windows used, typical particle displacements are $\delta_x = 4pixels$. This leads to an error estimate of $0.8 - 2mm/s(0.92 - 2.31\%)$. The total error can then be calculated as a combination of the calibration and cross-correlation error according to Equation B.3. Leading to a total uncertainty in the velocity field measurements of $0.9 - 2.04mm/s(1.03 - 2.36\%)$.

$$\epsilon_{\delta x} = \sqrt{(K\epsilon_{cc})^2 + (\delta x \frac{\epsilon_K}{K})^2} \tag{B.3}$$

B.2.1 Uncertainty of the mean and RMS velocity

The maximum PIV sample length is limited to 5454 images at 1024×1024 pixel resolution by the memory buffer in the SA2 Photron high-speed cameras used in the PIV setup. Increased sample size would come at the expense of a truncated field of view. In order to quantify the statistical errors in the mean velocity and RMS velocity measurements due to the finite sample, the convergence of the mean and RMS statistics can be estimated analytically using the variance of the mean (Equation B.4),and the variance of the standard

deviation (Equation B.5). These estimates give estimates of the standard error of the mean 0.58% and standard error of the RMS of 0.96% based on data collected in the wake at $x = 125mm$, $y = 0mm$.

$$\sigma_\mu = \sigma/\sqrt{N} \tag{B.4}$$

$$\sigma_\sigma = \sigma/\sqrt{2(N-1)} \tag{B.5}$$

However due to the data being collected in a time series in a periodic flow, the samples are not independent and hence these estimates may under predict the observed convergence, i.e. low frequency phenomena in the flume relative to the sample size will hinder convergence in the finite samples taken. Figure B.1a shows the convergence of the mean velocity and Figure B.1b the convergence of the RMS velocity versus sample length (N) both in the free-stream ($x = 125mm$, $y = 75mm$) where it is expected convergence will be quick due to the steadiness of the flow in this region, and along the wake centreline ($x = 125mm$, $y = 0mm$) where RMS fluctuations are much higher.

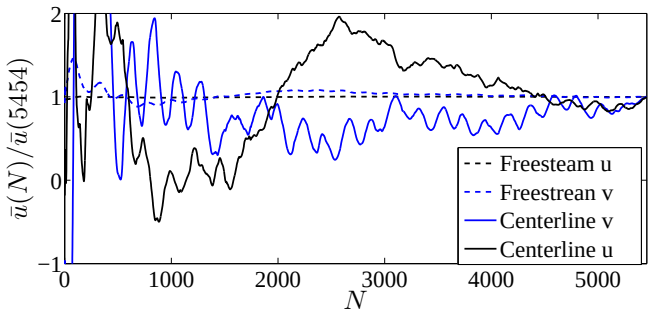

(a)

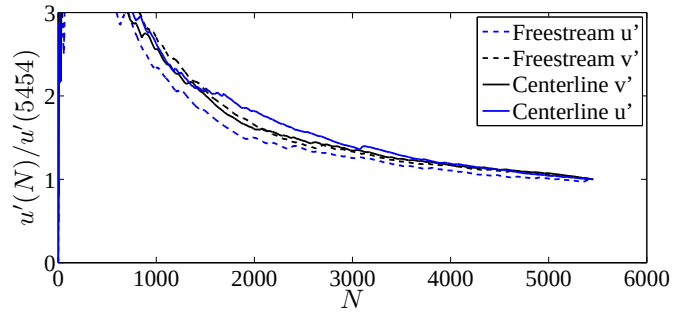

(b)

Figure B.1: Convergence of the (a) mean and (b) RMS velocities from PIV data obtained along the wake centreline ($x = 125mm$, $y = 0$) and in the free-stream ($x = 125mm$, $y = 75mm$).

Appendix C

Force balance calibration

The design and set-up of the strain gauge force balance used for the measurement of the mean and fluctuating forces on the models is presented in Section 3.4. Added details on the characterization of structural vibrations, calibration procedure and signal filtering are included herein.

In order to calibrate the force balance, the following procedure is employed. A set of calibrations weights ($1g$, $2g$, $5g$, $10g$) are used in combination to apply a known weight to the midspan of each model in a known direction using the string and pulley system shown in Figure C.1. The string is lightweight sewing thread and the pulley is a small ($0.5in\ OD$) ball bearing mounted on a moveable stand. The calibration is performed independently for each model such that differences in the weights of the models and re-assembly of the system are accounted for. The string is aligned within $z = \pm 1/16in$ of the midspan of each model and within $\pm 1^{\circ}$ of either the lift or drag direction during calibration. This leads to an equivalent total of $\pm 0.72\%$ uncertainty in the force applied to the cylinder due to

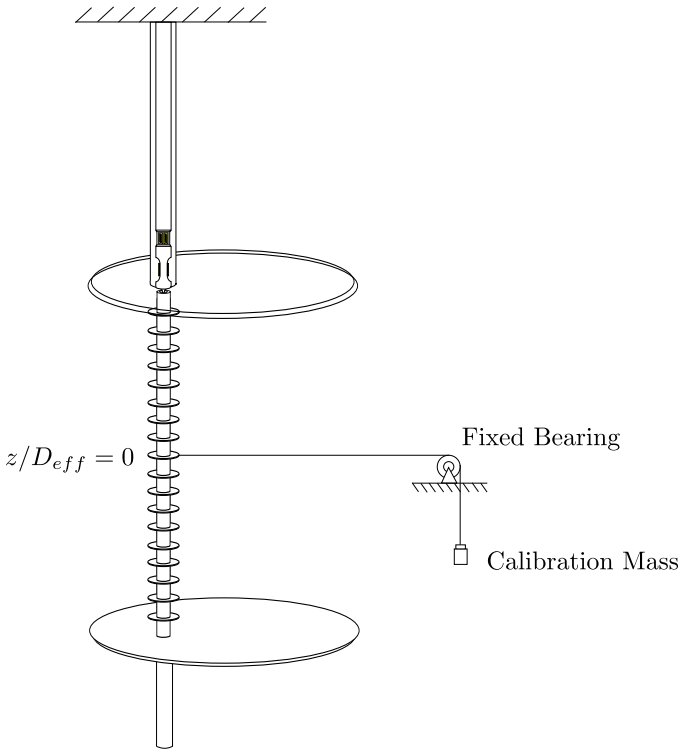

Figure C.1: Force balance calibration configuration.

geometrical alignment. The uncertainty in the mass of the calibration weight is negligible in comparison. In order to ensure that thread elasticity or frictional effects in the pulley did not effect the consistency of the calibration, five measurements were repeated with the smallest calibration weight ($1g$), leading to a repeatability estimate of $\pm 0.0084V$ or $\pm 0.069g$. While the repeatability error is significant for the smallest calibration weight (6.9%), it is less so for the higher calibration weights. In order to ensure reduce the effect of the repeatability error on the calibration, a minimum of two measurements are repeated for each calibration weight applied and used in the determination of the linear calibration curve. Sample calibration curves for the uniform cylinder model of diameter D are shown

in Figure C.2. The calibration exhibits good linearity such that knowledge of the force balance sensitivity $S(g/V)$, the no load voltage V_{nl} and the in-flow signal $V(t)$ gives a measurement of the forcing on the model (Equations C.1 and C.2).

$$\overline{F_D} = S(\overline{V(t)} - V_{nl}) \tag{C.1}$$

$$F_{L'} = SV'(t) \tag{C.2}$$

Since the calibration is performed in air, buoyant forces on the models must be accounted for when determining the no load voltage for the mean drag measurements. For each model, a solid back plate is installed in the flume and the flume is filled with quiescent water. Once the voltage signal settles due to the temperature change ($\approx 20min$), the mean signal is sampled (V_{nl}) and the value is used as a zero for the in-flow measurements. There is a small leakage flow in the flume, however the mean flow velocity is estimated to be $< 0.04167m/s$ from observations of the free surface flow and the change in water height with time. This small flow rate produces negligible forces on the model ($< 0.2\%C_D$). Repeatability of the buoyancy correction was $0.005V$, and the largest observed difference between the mean buoyant signal and the mean lift signal in-flow (which is assumed to be zero-mean) is $0.02V$, giving a maximum error estimate of $6.1\%C_D$ associated with the buoyant force correction. In order to ensure the hydrodynamics forces on the isolating shroud did not affect the force measurements, a known weight which approximates the mean drag acting on the shroud in the free-stream ($5g$) was applied to the shroud with the calibration system. The effect on the mean signal output was minimal ($< 0.0005V$) and

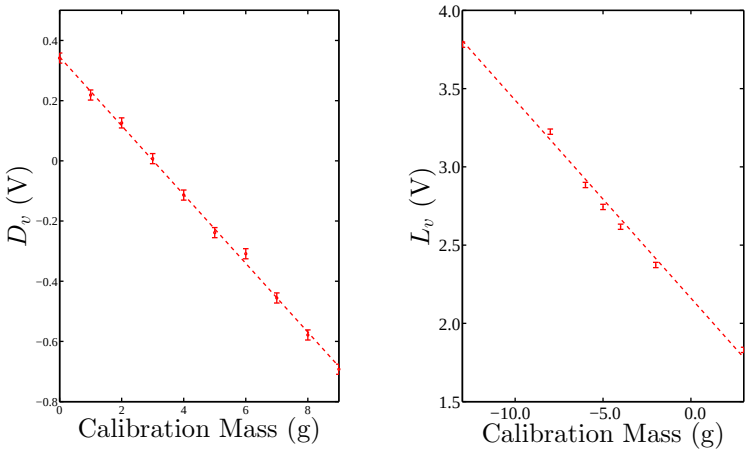

(a) (b)

Figure C.2: (a) Drag direction and (b) lift direction calibration curves for uniform cylinder ($Re_D = 1020$) model

hence is assumed negligible.

It is apparent from analysis of both the in-flow signals and the no-load signals in air, that structural vibrations of the flume and the force balance assembly have some effect on the measurements. The force balance was designed so the natural frequency of the force balance assembly was sufficiently higher than the characteristic vortex shedding frequencies [98], such that VIV are minimal. However, due to the small magnitude of the forces being measured, the vibrations of the structure leave a race on the signals and it is of interest to characterize the vibrations and filter them out. Spectra of the in-flow lift signal, and the no load in-air signal are shown in Figure C.3. Spectral peaks appear for frequencies $5 - 6\times$ the vortex shedding frequency in both signals which are associated the vibrations caused by noise sources in the laboratory.

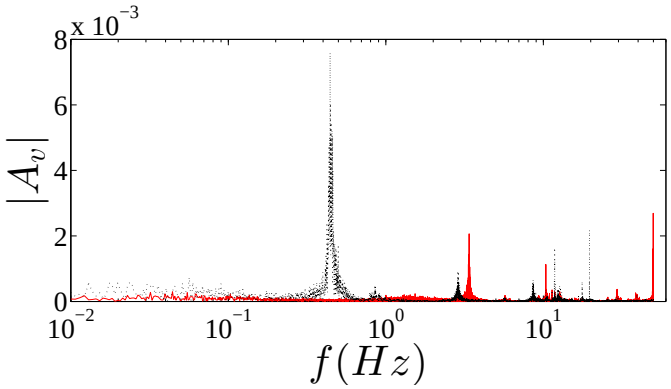

Figure C.3: The lift signal spectra for the $Re_{Df} = 2040$ model is shown in black, while the no load spectra of the model in quiescent air is shown in red.

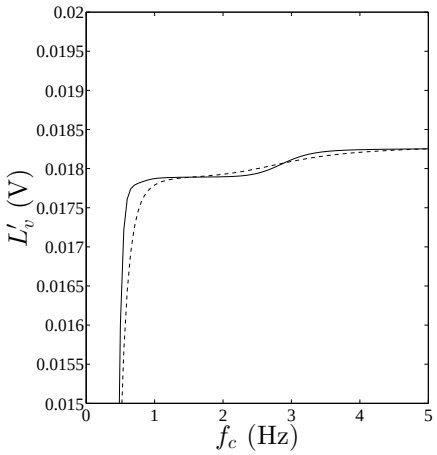

Figure C.4: Lift RMS vs. low-pass butterworth filter cut-off frequency (f_c) for $Re_{Df} = 2040$, (–) 3rd order filter (-) 7th order filter.

In order to filter the force balance signals, a low-pass butterworth filter is chosen with a cut-off frequency between the vortex shedding frequency and the structural vibration frequencies. Figure C.4 shows that a 7th order filter with cut-off frequency between $1 < f_c < 2.5Hz$ attenuates the vibrational frequencies without affecting the energy content of

the fluctuations at the vortex shedding frequency. The filtered lift and drag signals may be compared to the raw signals in Figure C.5.

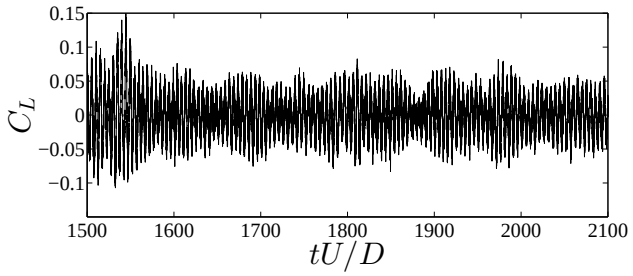

(a)

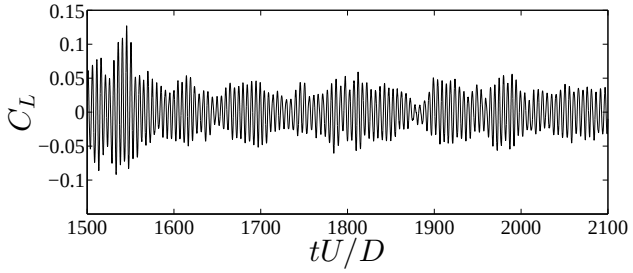

(b)

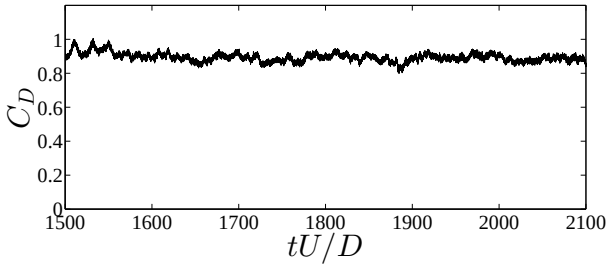

(c)

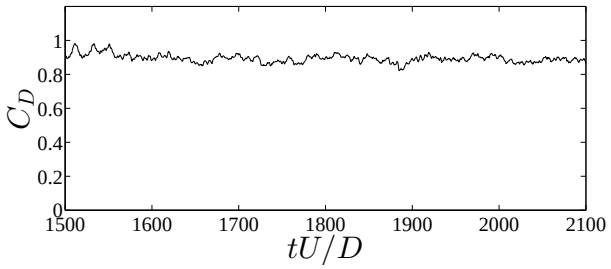

(d)

Figure C.5: (a) Raw lift signal, (b) filtered lift signal, (c) raw drag signal, and (d) filtered drag signal, for uniform cylinder ($Re_{Df} = 2040$) model.

Appendix D

Pressure PIV optimization

The use of numerical techniques to extract planar pressure fields ($p(x, y)$) from PIV data has become popular in recent years, with proven utility in the analysis of a wide range of flows [88,90,91,117–119]. A discussion of previous work on multiple methods for integrating the pressure field and characterizing the errors is provided in Section 2. The focus of this study is to optimize and compare the application of multiple pressure PIV techniques to the flow around a uniform cylinder. The effects of velocity error (ϵ_u) sensitivity and flow three-dimensionality are studied using numerical solutions for flow around a uniform cylinder at $Re_D = 100$, 300, and 1575. A mathematical model is proposed for determining the optimum spatial and temporal resolutions which minimize velocity error propagation in computed pressure fields (ϵ_p).

D.1 Numerical Study

The incompressible Navier-Stokes equations were solved numerically using the finite volume solver in ANSYS CFX 14.0 for flow around a uniform circular cylinder at $Re_D = 100$, 300, and 1575. The equations were discretized and solved on a two-dimensional mesh for $Re_D = 100$, and three-dimensional meshes for the higher Reynolds numbers ($s/D = 6$ for $Re_D = 300$ and $s/D = \pi$ for 1575) where flow is three-dimensional. Mesh sizing parameters were scaled based on the Reynolds number in order to ensure acceptable mesh density for resolving the decreasing temporal and spatial scales of the flow (Table D.1). Solutions were stepped forward in time such that a Courant number ($u\Delta t_{solv}/\Delta x_{solv}$) of less than one was maintained. No sub-grid-scale modelling was applied for the higher Reynolds numbers; the numerical dissipation of the mesh mimics the dissipative behaviour of the small scale eddies instead. Details of the numerical set up are included in Table D.1 and the accuracy of the numerical results is validated by a comparison to experimental results for the fluctuating lift force (C_L) [12], shedding frequency (St_D) [12], and mean drag (C_D) [59] . Vortex visualizations using the Q-criterion of the results are included in Section 2, which clearly show the increase in flow three-dimensionality and fine scale vortex structures with increasing Re_D.

In order to mimic PIV data, planar velocity fields ($\vec{u}(x, y)$) are extracted from the numerical solutions at varying temporal resolutions Δt and sampled on a square grid of spatial resolution Δx (Table D.2). The velocity fields coincide with the midspan of the cylinder across a domain in the wake from $0.5D < x < 4D$ and $-3D < y < 3D$. The sampled velocity fields are then subjected to artificially generated white-noise $\widetilde{u}(x, y) = (1+$

Table D.1: Experimental and numerical results for flow around a circular cylinder.

	Nodes	St_D	$C_{L'}$	C_D
Present Results ($Re_D = 100$)	3.5×10^4	0.167	0.231	1.351
Experiments ($Re_D = 100$)	-	0.164 [12]	0.227 [12]	1.43 [59]
Present Results ($Re_D = 300$)	1.7×10^6	0.199	0.423	1.278
Experiments ($Re_D = 300$)	-	0.202 [12]	0.457 [12]	1.24 [59]
Present Results ($Re_D = 1575$)	1.7×10^7	0.217	0.046-0.086	0.997
Experiments ($Re_D = 1575$)	-	0.211 [12]	0.045 [12]	0.95 [59]

$\epsilon_u)u(x, y)$ ranging from $\epsilon_u = 0-2.5\%$. The Eulerian spatial and temporal derivatives of the velocity fields are calculated using second-order central difference schemes on the discretized domain and used as input into the pressure solvers. Four pressure integration techniques are compared: (i) omni-directional line integration [91], (ii) iterative line integration [89], (iii) multiple-path integration [90], and (iv) Poisson equation [92]. A range of temporal and spacial resolutions are tested for each Reynolds number and are listed in Table D.2. For every respective temporal and grid resolution, and velocity error level, five pressure fields are calculated using each pressure solver. The resulting error in the pressure fields is quantified by the RMS difference (ϵ_p) compared to the pressure field from the CFD solution, according to Equation D.1.

Table D.2: Parameter space investigated for pressure PIV calculations.

Re_D	U_o (m/s)	D (m)	Δt (s)	$\Delta x/D$ (m)	ϵ_u (%)
100	0.009108	0.01	0.0065, 0.026, 0.104, 0.208, 0.416	0.03, 0.05, 0.07, 0.1	0-2.5
300	0.02733	0.01	0.005, 0.01, 0.02, 0.03, 0.04, 0.05, 0.1	0.03, 0.05, 0.07, 0.1	0-2.5
1575	0.1406	0.01	0.0003, 0.0009, 0.003, 0.009, 0.015	0.03, 0.05, 0.07, 0.1	0-2.5

$$\epsilon_p = \frac{\sqrt{\sum((p_{derived} - \bar{p}_{derived}) - (p_{numerical} - \bar{p}_{numerical}))^2}}{\sqrt{N}\rho U_o^2} \tag{D.1}$$

The results of the parametric study yield a large data set, with over 275 parameter space realizations for each pressure extraction method and Reynolds number. Optimization surfaces with respect to Δt and Δx may be constructed for each method and velocity error level. Figures D.1, D.2, and D.3 show the optimization surfaces for $\epsilon_u = 1.5\%$ along with a sample resulting pressure field from each method for $Re_D = 100$, 300, and 1575, respectively. The optimization surfaces indicate that once the temporal resolution becomes sufficiently small, the pressure error levels rise exponentially. This is due to random error in the velocity field being amplified for smaller Δt in the temporal derivative term in the N-S equation. The temporal resolutions investigated do not exceed the convective time-scales of the flow, hence excessively large errors are not observed for the higher Δt investigated. Nevertheless, a local minimum is always observed within the parameter space. For the range of spatial resolutions investigated, it appears that lower Δx may be possible without the propagation of the random error in the spatial derivative estimators disturbing the results substantially, as minimum pressure error levels occur for $\Delta x/D = 0.03$ in some cases. Generally high error values are observed for the higher spatial resolutions $\Delta x/D > 0.07$, where truncation errors begin to dominate.

Both the iterative-line integration and omni-directional integration methods exhibit the lowest sensitivity to random errors in the velocity field (Figures D.1, D.2, and D.3). The iterative-line integration method produces the lowest error values typically for a given configuration, however the computational time is extensive compared to the omni-directional

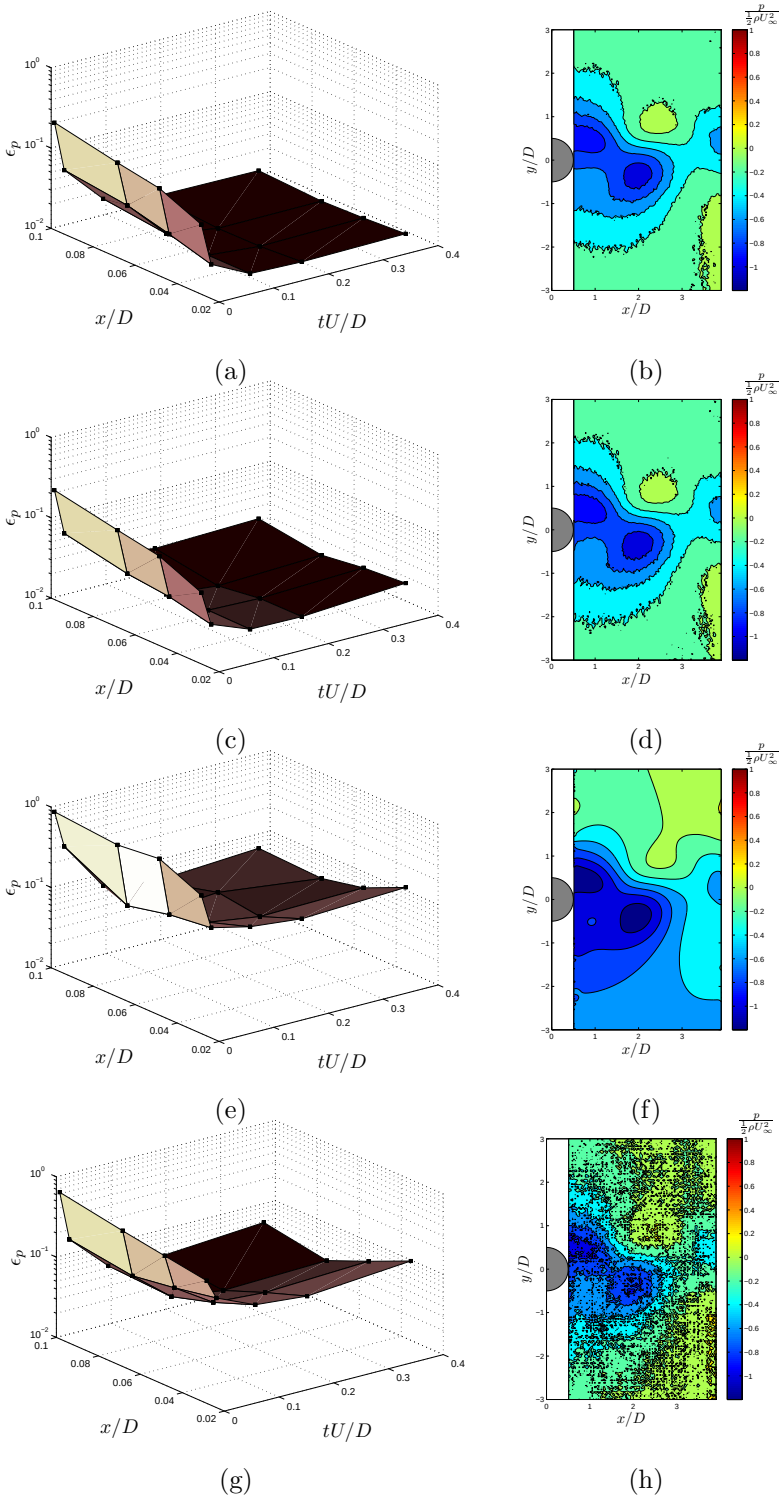

Figure D.1: $Re_D = 100$ optimization surfaces for $\epsilon_u = 1.5\%$ and sample pressure fields for (a-b) iterative line integrations, (c-d) omni-directional integrations, (e-f) Poisson equation, and (g-h) multiple path integration.

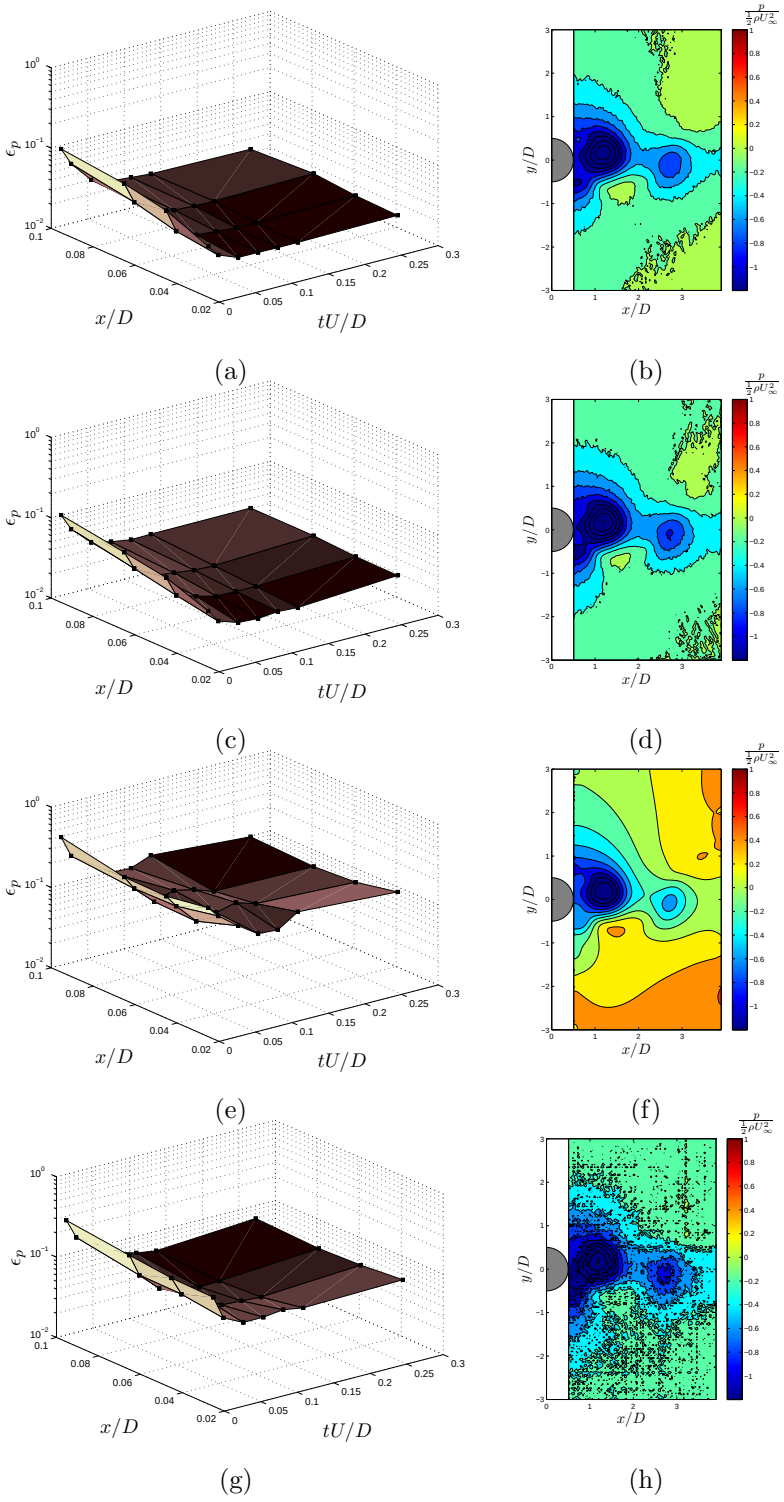

Figure D.2: $Re_D = 300$ optimization surfaces for $\epsilon_u = 1.5\%$ and sample pressure fields for (a-b) iterative line integrations, (c-d) omni-directional integrations, (e-f) Poisson equation, and (g-h) multiple path integration.

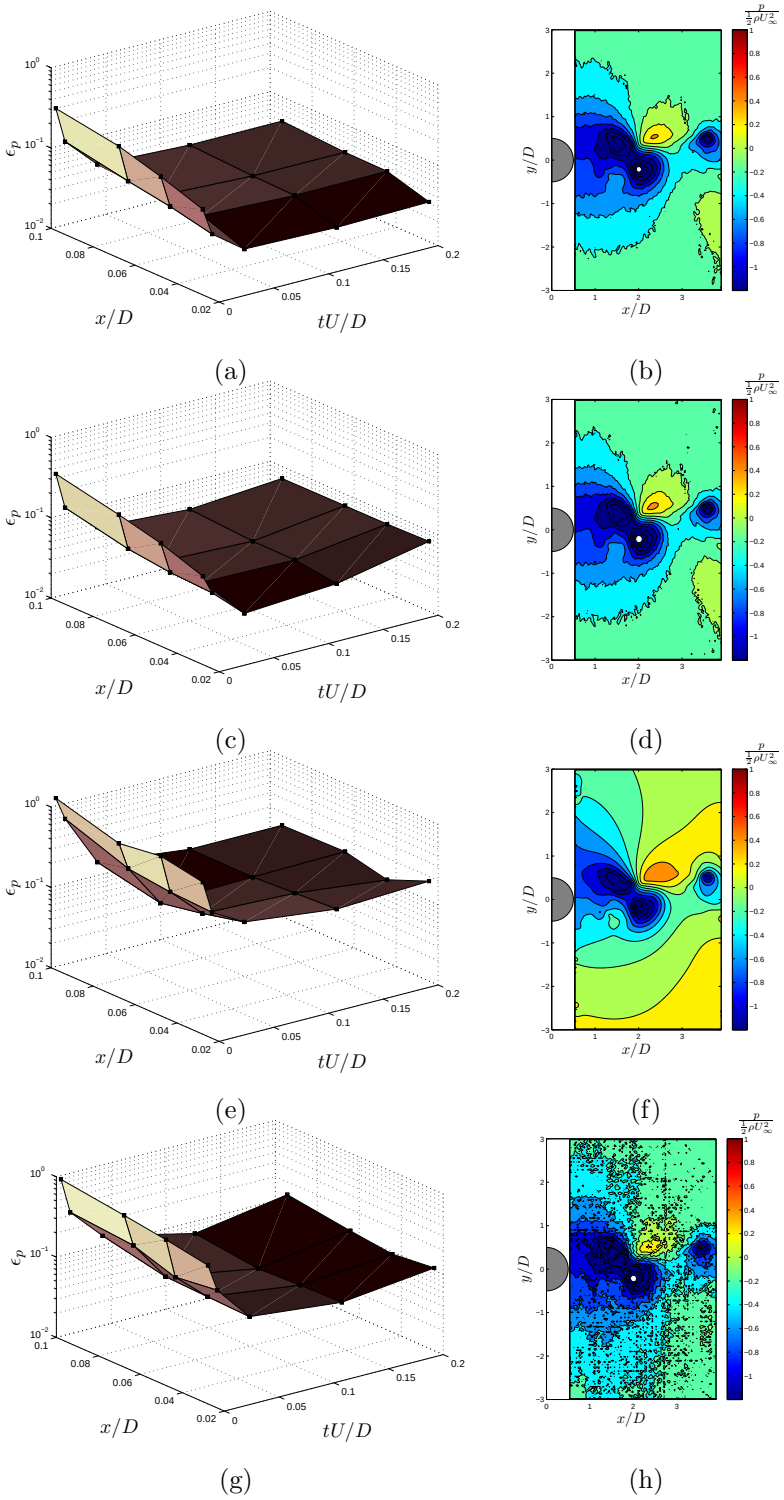

Figure D.3: $Re_D = 1575$ optimization surfaces for $\epsilon_u = 1.5\%$ and sample pressure fields for (a-b) iterative line integrations, (c-d) omni-directional integrations, (e-f) Poisson equation, and (g-h) multiple path integration.

scheme, so the latter may be a good computationally cheap alternative. The Poisson equation approach is shown to be very sensitive to random error, with large asymmetries arising in the pressure fields (Figures D.1, D.2, and D.3), compared to the primarily isotropic noise observed in the line integration techniques. Charanko et al. [93] also observed the Poisson equation approach being highly sensitive to random error in the velocity fields. The multiple-path line integration technique also performs poorly, the low number of line integrals involved in the pressure calculation results in substantial noise in the resulting fields. The sensitivity of the methods to ϵ_u are compared in Figure D.4, at a single temporal and spatial resolution for $Re_D = 100$. The figure clearly illustrates the high error sensitivities of the Poisson equation and multiple path integration methods. In addition, the Poisson equation method shows high deviation ($\sigma_{\epsilon p}$) between successive calculations with random white noise applied, while the line integration methods show lower deviation due to the averaging inherent in their application.

The error introduced in the determination of the pressure gradient ($\epsilon_{\nabla p}$) can be expressed in terms of the contributions of the propagation of the random velocity error (ϵ_u) [91] through the derivative estimators, and the truncation error terms introduced from the resolution of the derivative estimators. Therefore, for the second-order central difference schemes used herein, the pressure gradient error can be expressed as:

$$\epsilon_{\nabla p}^2 \approx \epsilon_{Du/Dt}^2 \approx \epsilon_u^2\left(\frac{1}{2\Delta t^2} + \frac{|u|^2}{2\Delta x^2} + |\nabla u|^2\right) + \frac{\Delta x^4}{36}(\nabla^3 u)^2 + \frac{\Delta t^4}{36}\left(\frac{\partial^3 u}{\partial t^3}\right)^2 \tag{D.2}$$

Equation D.2 implies that to minimize the pressure error, a balance must be struck

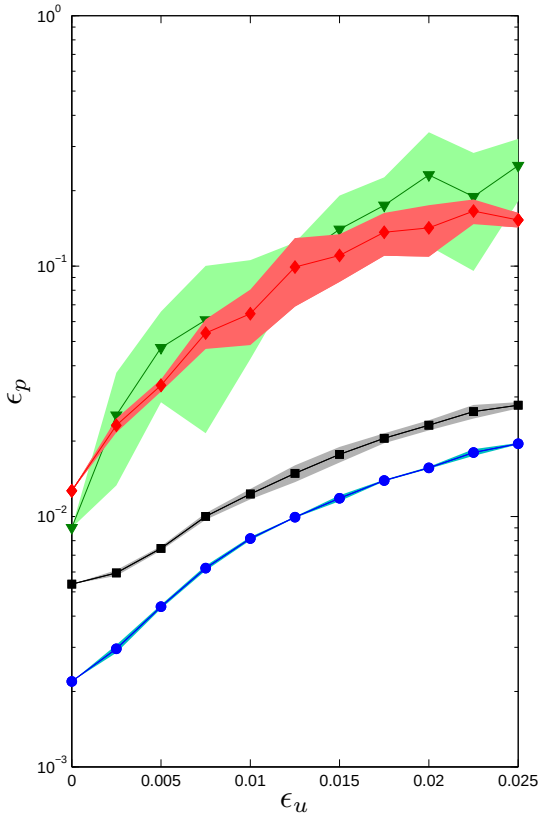

Figure D.4: Sensitivity of the pressure evaluation methods to random velocity error for $\Delta t U_o/D = 0.095$, $\Delta x/D = 0.03$, and $Re_D = 100$, ($\diamond$) multiple-path method, ($\square$) omni-directional method, ($\bullet$) iterative-integration method, and (∇) Poisson equation. The shaded regions indicate $\pm\sigma_{\epsilon p}$.

between the propagation of random error through the derivative estimators (represented by the first term in Equation D.2), which increases with decreasing Δt and Δx, and the truncation error introduced from the derivative estimators, which increases for increasing Δt and Δx. In order to develop a mathematical model for the optimum parameters which minimize the pressure field error (ϵ_p), an optimization problem may be solved for Equation D.2 with respect to Δt and Δx. The solution to the optimization problem for a given ϵ_u is then:

$$\Delta t_{opt} = (\frac{9\epsilon_u^2|u|^2}{(\partial^3 u/dt^3)^2})^{1/6} \approx \frac{(3\epsilon_u)^{1/3}}{f_{flow}} \tag{D.3}$$

$$\Delta x_{opt} = (\frac{9\epsilon_u^2|u|^2}{(\nabla^3 u)^2})^{1/6} \approx (3\epsilon_u)^{1/3}\lambda_x \tag{D.4}$$

The temporal and spatial derivatives in the expressions may be approximated by the timescales (f_{flow}) and spatial scales (λ_x) of the given flow, hence the values of the velocity and it's gradients will hence be flow dependent. For a circular cylinder, the following approximations can be made. The characteristic velocity scale is U_o, the time scale is the period of vortex shedding $f_{flow} = St_D D/U_o$. The length scale is the shear layer thickness, where the highest pressure gradients appear. The shear layer thickness may be approximated as $\lambda_x = \delta_{sl} = 7.5D/Re_D^{1/2}$ [4, 5]. Using these approximations results in a model for estimating the optimum sample spatial and temporal resolutions for the flow. Figure D.5 presents the optimum spatial and temporal resolutions as determined from the parametric study for each method and Reynolds number versus velocity error. The model developed in Equations D.3 and D.4 is validated against this data and is shown to predict the trends in Reynolds number and velocity error level well. Notably, since only five pressure fields

were calculated for each parameter point, the mean error response is not converged. In particular, for the Poisson equation approach, the results exhibited substantial deviation between evaluations, leading to some scatter in the sensitive determination of the optimum parameters. For higher Reynolds numbers, Δt and Δx are optimally lower in order to account for the thinning of the shear layers, general onset of smaller scale structures, and increase in shedding frequency.

In order to determine the Reynolds number effect on the accuracy of the planar pressure determination techniques, it is useful to compare the base errors present in the pressure field when zero noise ($\epsilon_u = 0\%$) is applied to the velocity fields. The base error is simply representative of: (i) the truncation error due to the derivative estimators, (ii) errors inherent to the integration method, and (iii) errors introduced by the two-dimensional assumption on the planar fields. The base error for each method is plotted in Figure D.6 against Reynolds number. The results show that the base error grows with Reynolds number, reaching $\approx 2\%$ for $Re_D = 1575$, perhaps indicating that three-dimensionality errors may be affecting the accuracy. However, the use of alternative formulations of the N-S equations was found to not affect the base error (Table D.3). A comparison of the 2D formulation, a 2D formulation which preserves dw/dz as calculated from the continuity equation [89,93], and the full 3D formulation show negligible differences between each other for each Reynolds number. This is attributed to the relatively weak spanwise velocities and spanwise gradients in the flow, such that the convective terms wdu/dz and wdv/dz in the N-S equations are small in comparison to the dominant streamwise and transverse convective terms. The increase in base error with Reynolds number is therefore solely attributed to the truncation error growth, which is associated with the smaller spatial and

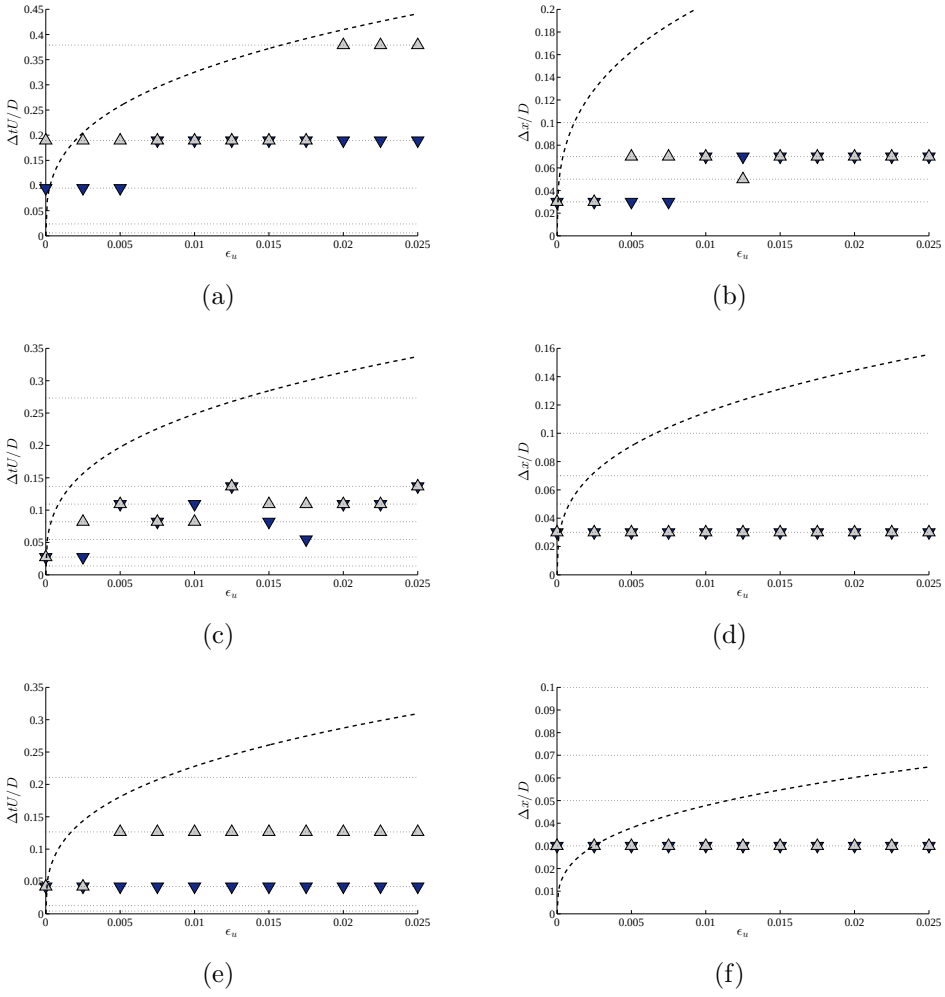

Figure D.5: Optimum Δt and Δx vs. velocity random error ϵ_u for ($\bullet$) iterative line integration, ($\triangleleft$) omni-directional integrations, ($\Diamond$) Poisson equation, and ($\triangle$) multiple path integration and (a-b) $Re_D = 100$, (c-d) $Re_D = 300$, and (e-f) $Re_D = 1575$. The proposed models (Equations D.3,D.4) are shown by the dotted lines.

temporal scales encountered with increasing Reynolds number.

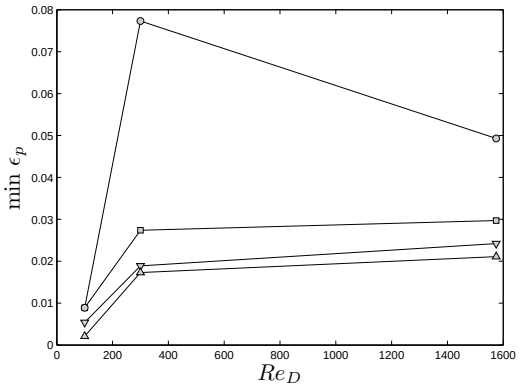

Figure D.6: Minimum RMS pressure field error ϵ_p vs. Re_D.

Table D.3: Base error of the pressure evaluation governing formulation vs. Re_D

Re_D	min(ϵ_p) 2-D	min(ϵ_p) 2-D conservative	min(ϵ_p) 3-D
100	0.21%	0.21%	0.21%
300	1.73%	1.73%	1.74%
1575	2.11%	2.10%	2.09%

D.2 Experimental Study

Due to the substantial computational time involved in calculating the pressure fields ($\approx$ 10 minutes for a single 256×256 vector field), time-resolved pressure PIV estimates were not performed in the thesis. However, the techniques may be used on the mean and RMS statistics derived from the PIV experiments in order to determine the mean pressure field. When averaged in time, the Navier-Stokes equation becomes the Reynolds-Averaged

Navier-Stokes (RANS) equation (Equation D.5), which can be integrated using the previously discussed methods.

$$\nabla p(x,y) = \mu \nabla^2 \vec{u} - \rho(\nabla \cdot \tau_{\overline{u'v'}}) - \rho(\vec{u} \cdot \nabla \vec{u}) \tag{D.5}$$

The mean pressure fields calculated for the experimental results for uniform cylinders of $Re_D = 1020$ and 2040 are compared to the numerical results for $Re_D = 1575$ in Figure D.7. The mean pressure field is not fully converged for the numerical results, due to the high computational time needed, however in the near wake, the pressure fields are fairly steady in time and hence can be used for comparison. The pressure fields are estimated using the omni-directional line integration technique [91]. The Figure shows the pressure fields estimated from the PIV experiments show good agreement with those extracted from the numerical solution, validating the approach.

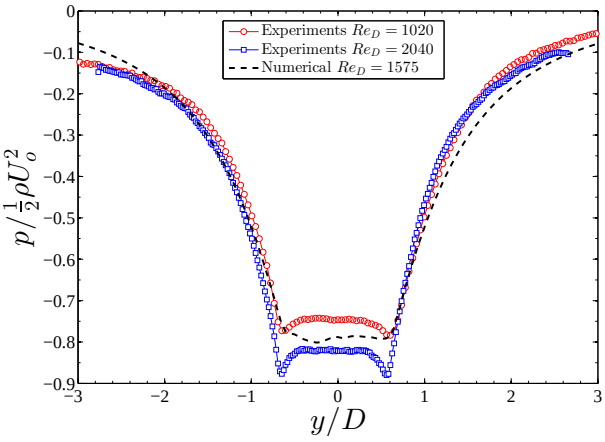

(a)

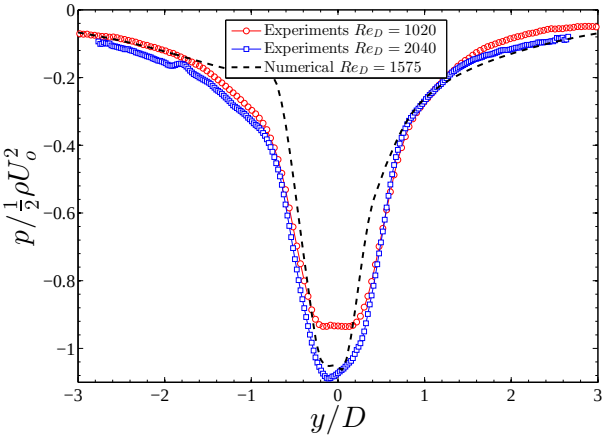

(b)

Figure D.7: Experimental pressure PIV results for $Re_D = 1020$ and 2040 using the omni-directional line integration technique compared to the numerical solution for $Re_D = 1575$ with transverse pressure profiles obtained at streamwise locations (a) $x/D = 0.5$, and (b) $x/D = 2.0$.